CARBON FIBER MICROELECTRODE ARRAYS FOR NEUROPROSTHETIC AND NEUROSCIENCE APPLICATIONS

by

Paras Rajni Patel

A dissertation submitted in partial fulfillment
of the requirements for the degree of
Doctor of Philosophy
(Biomedical Engineering)
in The University of Michigan
2015

Doctoral Committee:

Assistant Professor Cynthia A. Chestek, Chair
Assistant Professor Timothy M. Bruns
Daryl R. Kipke, Executive Director, NeuroNexus Technologies
Professor Nicholas A. Kotov
Assistant Professor William C. Stacey

DEDICATION

To my Mom, Dad, and Sister. You have always been there for me and believed in me, even when I did not. I cannot thank you enough for the love and support you have shown me throughout this endeavor.

ACKNOWLEDGEMENTS

Working towards my Ph.D. has been the hardest thing I have done thus far in my life. While it would be easy to claim this work as entirely my own that would be far from the truth. All graduate students rely on the vast network that makes up a lab and department and I have truly benefitted from this in more ways than I can recount. That said, I will attempt to acknowledge all of those individuals who have helped me reach this goal.

I would like to first thank my advisors, Daryl Kipke and Cynthia Chestek. No graduate student is complete without their advisor and I have learned so much from them both. They have both taught me how to be a better scientist, engineer, and researcher. Throughout my many years at Michigan they have both always supported my research, even if the goal was unclear and fraught with difficulties. Their confidence in my abilities, over my sometimes lackluster results, is one of the biggest reasons that I have been able to reach this point. For this I am eternally grateful.

Though my advisors served a large role in my day to day academic career, I have also gained valuable insights from my committee members. William Stacey taught me how to look at a problem from both a medical and engineering viewpoint, and strike a balance between the two. Tim Bruns has challenged me to know and understand even the smallest of details about my work. Watching him run marathon experiments that lasted

well over 48 hours has impressed upon me the importance of experimental design and never settling when more questions can be asked and data collected. Nicholas Kotov has been an amazing collaborator in my research. He was always there to suggest new modifications to improve the durability of my probes and never hesitated when I asked for assistance from his group.

Most individuals have the honor of being part of one lab in their graduate career, I have had the distinct pleasure of being part of three. I would first like to thank my lab by proxy, the Shikanov lab. You treated me like one of your own without hesitation. The friendships I have formed with you all are treasured. I will miss bothering you all, even when you were trying to get work done while my 'data was processing'. You are an exemplary group of people and it has been a pleasure being part of your group. To my current lab, the Chestek lab, I know we have physically worked apart for a few years now, but even in that time I feel like I have been working with you in lab every single day. You are an amazing group of people that have enjoyed each other's company in the best of times and come together in the worst of times. Autumn Bullard, Dave Thompson, Derek Tat, Kaile Bennett, Karen Schroeder, Nicole Bentley, Philip Vu, and Zachary Irwin, you reminded me of what it is to have labmates and I look forward to actually working side-by-side with you in the coming months.

The members of the Neural Engineering Lab have had the biggest impact on me both personally and in my research. Without their collective knowledge I would not be here today. Matt Gibson was an excellent mentor in some of my toughest times and more importantly has become a close friend. His outlook on life and work, regardless of the situation, has been an inspiration and definitively shaped who I am today. Takashi Kozai

has been an immeasurable force in helping me develop my research and analytical skills. His gift in asking the right questions and more importantly to see them through with answers has been an inspiration. Even after leaving Michigan, he responded to my many emails, texts, calls, and chats about research, without any delay. Nick Langhals was fundamental to my early days in lab. His training and guidance would serve as the bedrock to much of my research. Without him I would not have had the confidence nor ability to do the work that I have done here at Michigan. Karen Schroeder has been an instrumental part of my life and sanity in lab. She came in two years after I did, but it feels like I have known her for much longer. Her maturity, adeptness in research, and most importantly her friendship made life in lab far more enjoyable. Without her, lab would not have been the same and I am fortunate that I can forever call her my colleague and friend. Colin Stoetzner and Andre Snellings both provided me with the wisdom that only post doctorates can give. Their collective experiences helped me to put mine in context and their guidance both academically, but more professionally, will always stay with me. Though I did not overlap much with Kip Ludwig, he treated me like we had been labmates for years. Even after leaving, he continually offered his help in revising manuscripts or to just talk about research. John Seymour was another individual with whom I did not overlap with at the beginning. However, his continued stay in Ann Arbor has led to our close friendship in both the academic and non-academic settings and I am fortunate to call him a friend. Labmates like this remind me what it truly means to be part of a lab, regardless of when you joined or left. No graduate student would be complete without the help of talented undergraduate students. To Justin Nofar, Geoffrey Burns, Matthew Robbins, Michael Kobylarek, and Shaun Marshall, your dedication to all

tasks small and large, has helped me immensely. To all the other members of the lab, Amanda Perez, Amisha Agarwal, Azadeh Yazdan, Erin Purcell, Eugene Daneshvar, Firas Midani, Greg Gage, Hirak Parikh, John Bentley, Karen Coulter, Komal Kampasi, Kyle Ronquist, Michael Joseph, Pratik Rohatgi, Rachel Miriani, Rikki Hullinger, Taegyun Moon, Taneev Escamilla, Timothy Marzullo, Vera Williams, and Ziya Bhagmanli, many thanks for your comradery and friendship, you truly made my lab experience memorable and I will always cherish that time we spent together.

Finally, my biggest and most heartfelt thanks goes to my family. This is not an easy task as I have quite a large family. First, I would like to thank my extended Michigan family. Before I moved here, I did not know many of them, let alone how we were related. None of that actually mattered as they treated me like a family member they had known their entire lives. I have grown very close to all of them and am lucky to have them. Second, I cannot express how grateful I am to my aunt and uncle who live in Ann Arbor. From the moment I landed in Michigan, they treated me like their own son, and made Michigan feel like home. Their door was always open to me without hesitation and a home cooked meal not far away. To this day I cannot imagine life in Ann Arbor without them and am blessed to have them here. Finally, and most importantly, I want to thank my Mom, Dad, and Sister for being with me every step of the way. You have taught me the value in working hard in life, but also of the importance in being able to laugh even in the toughest times. Your support never wavered, your confidence never flagged, and your love never ceased. Without you, none of this would have been remotely possible and I owe you everything. I love you three very much.

TABLE OF CONTENTS

LIST OF FIGURES

LIST OF TABLES

LIST OF APPENDICES

ABSTRACT

The aim of this work is to develop, validate, and characterize the insertion mechanism, tissue response, and recording longevity of a new high-density carbon fiber microelectrode array. This technology was designed to significantly improve the field of penetrating microelectrodes while simultaneously accommodating the variable needs of both neuroscientists and neural engineers.

The first study presents the fabrication and insertion dynamics of a high-density carbon fiber electrode array using a dual sided printed circuit board platform. The use of this platform has pushed electrode density to limits not seen in other works. This necessitated the use of an encapsulation method that served to temporarily stiffen the fibers during insertion, but did not enter the brain as many other shuttles do for other probe designs. The initial findings in this work informed the development of an even higher density array using a silicon support structure as a backbone.

The second study reports on the tissue reaction of chronically implanted carbon fiber electrode arrays as compared to silicon electrodes. Due to their smaller footprint, the reactive response to carbon fibers should be greatly attenuated, if not non-existent. Results show a scarring response to the implanted silicon electrode with elevated astrocyte and microglia activity coupled to a local decrease in neuronal density. The area implanted with the carbon fiber electrodes showed a varied response, from no detectable

increase in astrocytic or microglial activity to an elevated activation of both cell types, but with no detectable scars. Neuronal density in the carbon fiber implant region was unaffected. The data demonstrates that the small carbon fiber profile, even in an array configuration, shows an attenuated reactive response with no visible scaring.

The final study reports on the viability of chronically implanted high-density carbon fiber arrays as compared to more traditional silicon planar arrays with comparable site sizes. While most new probe technologies or designs are able to demonstrate proof of concept functionality in acute preparations, very few show the ability to record chronic unit activity. This study aims to provide a comprehensive analysis of electrophysiology data collected over implant durations ranging from 3 – 5 months.

CHAPTER I

Introduction

Recording long-term activity from every neuron in any area of the brain would have profound implications for fundamental research aimed at better understanding and treating the brain and for neuroprosthetics aimed at rehabilitating those with traumatic nervous system injuries. In animal models, such as those for Parkinson's disease and epilepsy, the observations of neuronal circuit dynamics can lead to better informed diagnoses and treatment strategies in human patients. Furthermore, chronic recordings of motor cortex activity in human patients that suffer from paraplegia or quadriplegia have been used to control prosthetic limbs through the use of a brain machine interface. These brain machine interfaces (BMIs) are a collection of systems that take neural recordings from within the patient's intact motor cortex, feed this data through a set of algorithms that interpret the patients desired movements based on neural firing patterns, and then use this information to actuate a prosthetic limb in the desired manner (Simeral et al. 2011; Carmena et al. 2003; Velliste et al. 2008; Hochberg et al. 2012; Hochberg et al. 2006; Taylor et al. 2003; Schwartz et al. 2006). For all of these applications, impressive strides have been made in recording technology, in particular for long-term studies, but more

work is needed to improve the reliability and density of recording electrodes that will in turn provide a more faithful representation of the underlying neural activity.

Recording all the neural activity in a small 0.5 mm^3 volume of motor cortex, given an estimated density of 9.9 x 10^6 neurons/cm^3 (Cragg 1967; Lempka et al. 2011), would require sampling from nearly 5000 individual neurons. Currently no device exists that can accomplish this task. A recording technology that can meet this goal and maintain signal fidelity over the lifetime of the device would need to incorporate numerous recording channels in a dense configuration, be minimally obtrusive to the subject, and be biocompatible if implanted in the body.

The primary focus of this dissertation is to demonstrate the viability of a neural recording technology based on penetrating carbon fiber microelectrode arrays. These carbon fiber microelectrodes meet the necessary requirements of a small, scalable, and biocompatible technology that has the capability to sample from every neuron in a given brain region and can improve the understanding and treatment of neurological diseases and the effectiveness of BMIs.

1.1 Motivation for Single Unit Recordings

Many different technologies exist that can be used to study and query the brain. In addition, these different technologies have all demonstrated the ability to be used in BMI applications (Lebedev & Nicolelis 2006; Donoghue 2002; Schwartz et al. 2006). Though they exist in many different variations, each electrical recording modality generally falls under one of three broad categories: electroencephalography (EEG), electrocorticography (ECoG), or penetrating microelectrodes. Each type of technology differs in its level of invasiveness and information content. In general, to sample specific

communications between individual neurons or small groups of neurons the more invasive the technology will be. Conversely, less invasive technologies provide less resolution of specific neuronal activity and will instead relay information about the overall state of brain activity in the area of inquiry.

Recording from all areas of the brain simultaneously is accomplished using EEG. This technology typically employs the use of dozens of electrodes placed on the scalp, often with the aid of a recording cap that secures the electrodes in place (Teplan 2002). While unable to detect the firing of individual neurons, EEG recordings can be used to sense changes in neuronal states in different regions of the brain. These changes can be of particular use in areas such as epilepsy (Noachtar & Rémi 2009; Musumeci et al. 1999; Smith 2005), sleep studies (Feinberg & Campbell 2010; Acharya et al. 2005), and depression (Steiger & Kimura 2010; Riemann et al. 2001). In addition, EEG recordings have been used to control BMI systems (Wolpaw et al. 1991; Wolpaw & McFarland 2004; Bell et al. 2008; Lauer et al. 1999; Hoffmann et al. 2008). Implementation of EEG can be straightforward but there are also drawbacks, particularly for many neuroscience studies or BMIs. EEG cannot be used to study circuit level connections or precise neural firing patterns in animals due to the lack of resolution. The large number of wires and time needed to prepare an EEG head cap also makes it impractical for human BMI use.

More invasive than EEG is ECoG, which requires a craniotomy to place a small grid of electrodes on the surface of the dura mater, a layer of tissue that encapsulates the brain, or directly on the brain itself. Placing electrodes in close proximity to the source of neural activity eliminates signal losses experienced by EEG, where the signal must first travel through the skull and skin which leads to attenuation. ECoG grids also provide

higher spatial resolution compared to an EEG grid; however, due to its invasive nature, covering the entire surface of the brain with ECoG electrodes would be impossible. Because of this higher spatial sensitivity ECoG has been used in a variety of studies concerning BMIs (Leuthardt et al. 2004; Leuthardt et al. 2011; Chestek et al. 2013). While ECoG provides a higher resolution of neural activity, even demonstrating the ability to record neuronal spikes (Khodagholy et al. 2015), they still lack the ability to access and record unit activity from deeper cortical layers.

The most invasive recording technology uses penetrating microelectrodes. These electrodes are made from a range of materials (Najafi et al. 1985; Seymour & Kipke 2007; Harris, Capadona, et al. 2011; Kim et al. 2013; Nordhausen et al. 1996; Cheung et al. 2007; Mercanzini et al. 2008; Moxon et al. 2004; Ware et al. 2012; Rennaker, Ruyle, et al. 2005) and can be designed to access any area of the brain. With a smaller form factor than both EEG and ECoG, penetrating microelectrodes are designed to interface with a smaller region of the brain, but also provide higher spatial resolution. As with EEG and ECoG, penetrating microelectrodes have their own tradeoffs. Regardless of location or depth, these electrodes require penetration of the brain, which in turn can cause damage (Kozai et al. 2010; Potter et al. 2012). This damage can persist over time and contribute to the failure of an implanted probe (Ward et al. 2009; Winslow & Tresco 2010; Winslow et al. 2010; Barrese et al. 2013; Polikov et al. 2005). Though these limitations are well known, penetrating microelectrodes are routinely used in both acute and long-term neuroscience studies (Davidson et al. 2009; Cohen et al. 2012; Berke et al. 2009; Self et al. 2014; Royer et al. 2010) and are the predominantly used electrode for BMIs (Carmena et al. 2003; Simeral et al. 2011; Hochberg et al. 2006; Chestek et al.

2011; Collinger et al. 2013; Velliste et al. 2008; Hochberg et al. 2012; Taylor et al. 2003; Schwartz et al. 2006).

While all three technologies have their benefits and drawbacks, it is penetrating microelectrodes that offer the best insight into the intricacies of neuron to neuron communications. Information content at this level provides the best opportunities for controlling BMIs and understanding the dynamics within and between specific brain regions.

1.2 Penetrating Microelectrodes

The viability of chronic neural recordings using penetrating microelectrodes was demonstrated as far back as the late 1950's, using 80 μm diameter, insulated stainless-steel wires (Strumwasser 1958). Since that time remarkable progress has been made in the development of microelectrodes, with advances that have led from the smallest of wires to probes manufactured using the same processes and materials found in today's microprocessors.

Microwires (figures 1.1(a) & 1.1(b)), much like those used by Strumwasser, still remain popular today for their ease of use, simplicity, and ability to reach deep structures (Cheung 2007; Tseng et al. 2011). They can be arranged in multiple configurations, with the tetrode (Cheung 2007; Gray et al. 1995) and the linear, or grid, arrangement (Nicolelis et al. 2003; Williams et al. 1999; Rennaker, Street, et al. 2005; Prasad et al. 2014) being two of the most prevalent. Popular materials used to make microwire arrays or bundles include tungsten (Nicolelis et al. 2003; Rennaker, Ruyle, et al. 2005; Williams et al. 1999), stainless-steel (Nicolelis et al. 2003; Strumwasser 1958), and

platinum/iridium (Prasad et al. 2014; Chakravarty & Faingold 1998), with insulating coatings of polyimide (Prasad & Sanchez 2012) or teflon (Nicolelis et al. 2003).

In the last few decades a new style of microelectrode technology has emerged using clean room manufacturing processes. The two most dominant designs are the Michigan probe, developed at the University of Michigan, and the Utah Array, developed at the University of Utah. The Michigan probe (figure 1.1(c)) is based on a planar silicon platform with multiple electrode sites along the shank of the device (Wise & Angell 1975; Najafi et al. 1985; Wise et al. 2004; Vetter et al. 2005). This electrode style has been shown to chronically record neural activity (Kipke et al. 2003; Ludwig et al. 2006; Vetter et al. 2004; Karumbaiah et al. 2013; Berényi et al. 2014; Otto et al. 2006; Gage et al. 2006; Parikh et al. 2009), detect local neurotransmitter levels (Johnson et al. 2005; Johnson et al. 2008), detect local changes in pH (Johnson et al. 2007), integrate with fluidic tubing for drug delivery applications (figure 1.1(d)) (Rohatgi et al. 2009), and deliver light to targeted areas for optogenetic stimulation (figure 1.1(e)) (Wu et al. 2013; Im et al. 2011). Other groups have emulated the planar style electrode and created devices that are made of ceramics (figure 1.1(f)) (Moxon et al. 2004; Burmeister et al. 2002), can sense biochemicals (Moxon et al. 2004; Burmeister et al. 2002; Frey et al. 2010), or integrate fluidic channels directly within the device (Frey et al. 2011).

The Utah Array consists of a grid design with 100 individual recording shanks, conical in shape, with the recording site at the tip (figure 1.1(g)) (Campbell et al. 1991; Nordhausen et al. 1996). Originally developed for use in the visual cortex of cats (Campbell et al. 1991; Nordhausen et al. 1996) and to aid in vision prostheses (Campbell et al. 1991; Normann et al. 1999), they quickly transitioned to use in BMIs for those with

motor impairments (Maynard et al. 1997; Simeral et al. 2011; Hochberg et al. 2012; Hochberg et al. 2006). Recent advances in fabrication technology have led to longer term reliability of the parylene-c insulating coating (Xie, Rieth, Williams, et al. 2014; Xie, Rieth, Negi, et al. 2014), more uniform exposure of the electrode recording sites (Bhandari et al. 2009), better site coatings for lower impedance (Negi et al. 2010), arrays with variable shank lengths (Branner et al. 2001; Sharma et al. 2011), and arrays with a higher shank density (figure 1.1(h)) (Wark et al. 2014; Wark et al. 2013).

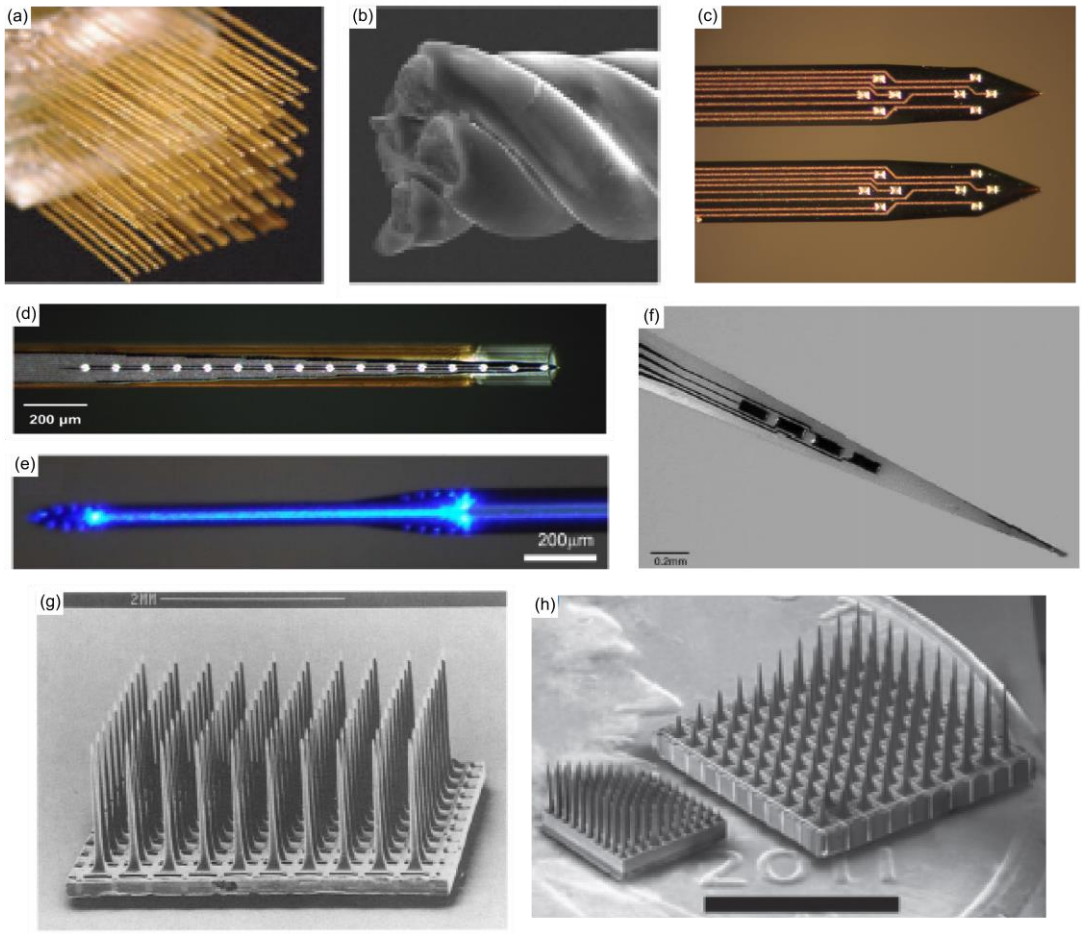

Figure 1.1. Examples of penetrating microelectrodes. (a) Tungsten microwires in a grid configuration (Nicolelis et al. 2003). (b) Tungsten microwires in a tetrode configuration (Liao et al. 2011). (c) Michigan style planar electrode. (d) Michigan electrode with integrated fluidic tubing (Rohatgi et al. 2009). (e) Michigan electrode with integrated waveguide (Im et al. 2011). (f) Ceramic based microelectrode (Burmeister et al. 2002). (g) Utah array (Nordhausen et al. 1996). (h) Utah arrays with variable lengths and high density shanks (Wark et al. 2013).

1.3 Probe Failure Mechanisms

1.3.1 Local Tissue Response

One of the largest drawbacks to using penetrating microelectrodes is their propensity to fail over time. This long-term failure can often be directly tied to the lack of healthy functioning neurons near a probe's recording site(s). This cell death is thought to be related to the formation of a glial scar around the probe. The initial wound from a probe insertion causes the rupture of microvasculature, as well as localized cell damage. The contents released from both the damaged cells and microvasculature will attract and activate astrocytes and microglia, two native glial cells (Edell et al. 1992; Carter & Houk 1993; Schmidt et al. 1993; Turner et al. 1999; Liu et al. 1999; Szarowski et al. 2003; Biran et al. 2005; Polikov et al. 2005; McConnell et al. 2009; Grand et al. 2010; Winslow & Tresco 2010). Both types of cells exist within the brain in an inactive form; however, chemical factors released during injury such as monocyte chemotactic protein-1 (Biran et al. 2005; Sawyer et al. 2014), interleukin 1 (Kozai et al. 2014), & tumor necrosis factor-alpha (Biran et al. 2005; Smith et al. 2012) will induce both morphological and functional changes. Activated astrocytes and microglia further recruit other glial cells, resulting in a localized cascade of cell activation (Biran et al. 2005; Polikov et al. 2005). The ensuing sheath formed by these cells leaves little room for neuronal growth (Edell et al. 1992; Liu et al. 1999; Winslow & Tresco 2010). This sheath changes in size and composition as time progresses with the implant in place. After the initial probe insertion, there is localized bleeding as well as cellular rupturing. Within the first 2 – 4 weeks, a sheath of activated astrocytes and microglia form. Studies have shown the initial radius of the microglia sheath to be up to 200 μm in the early weeks of implantation followed by a

"tightening", wherein the sheath radius decreases to roughly 100 μm at 16 weeks or longer (Szarowski et al. 2003; McConnell et al. 2009; Winslow & Tresco 2010; Ersen et al. 2015). Similarly, early astrocytic activity has been shown to be as far reaching as several hundred microns away, eventually coming down to a radius of 50 – 100 μm (Szarowski et al. 2003; Ersen et al. 2015) although some researchers have seen final radii as large as 300 μm (McConnell et al. 2009).

Past the initial three month implant period the glial sheath changes very little and resides in a state of equilibrium. In a typical injury response, the inflicted wound would heal with minimal scarring and show a down regulation of activated response cells (Biran et al. 2005; McConnell et al. 2009). However, the persistent glial scar that surrounds neural probes has led to multiple hypotheses as to why gliosis persists. One popular thought is that the presence of the probe prevents the brain's vasculature from fully healing. These continuously leaking vessels release inflammatory factors into the wound site causing the reaction to persist (Szarowski et al. 2003; Biran et al. 2005; McConnell et al. 2009; Winslow & Tresco 2010; Saxena et al. 2013; Potter et al. 2012). Another idea put forth is the concept of frustrated phagocytosis wherein the microglia are unable to digest the foreign body, in this case the probe, and continually release chemokines to further recruit more microglia (Polikov et al. 2005). Yet others have proposed neither of these issues being the direct problem, but instead point to the local chemical environment as being toxic for neural growth and/or regeneration due to the release of neurotoxic factors from activated microglia (Guilian et al. 1993).

1.3.2 Mechanical Mismatch and Micromotion

While the persistence of the glial scar can easily be linked to the presence of a foreign body in the brain, many have hypothesized that this persistence can be more precisely tied to the physical properties of the implant and its mechanical interaction with the local environment. When a probe is implanted within the brain it is subject to many different forces. Of these forces, the most regular and persistent are the small movements, or micromotion, that the brain continually undergoes. This micromotion is on the order of 1 – 25 μm and is due to both respiration and the pulsatile nature of vascular activity (Gilletti & Muthuswamy 2006; Muthuswamy et al. 2003). One group has hypothesized that the persistent inflammatory response is in part due to the inability of traditional microelectrodes to move with the brain (Gilletti & Muthuswamy 2006; Muthuswamy et al. 2003). Instead, these stiff materials tend to stay in place, particularly when tethered to the skull (Biran et al. 2007; Karumbaiah et al. 2013), leading to a stiffening of the local tissue environment (Sridharan et al. 2013) and to potential ruptures in nearby cells or vasculature (Saxena et al. 2013). This continual rupturing of vasculature may be partially alleviated by implanting probes further away from major surface vessels (Kozai et al. 2010) or by implanting the electrode in an untethered manner (Biran et al. 2007; Karumbaiah et al. 2013). The use of more mechanically compliant materials has also been proposed to alleviate the mechanical mismatch between the brain and the implanted probes which can help to mitigate the micromotion effects of stiff electrodes (Subbaroyan et al. 2005; Subbaroyan & Kipke 2006; Sankar et al. 2013).

1.4 Reducing Tissue Inflammation

To improve recording quality from chronically implanted probes, many groups have focused primarily on reducing tissue inflammation as well as improving the interface between the actual electrode recording sites and the brain. By reducing the long-term inflammatory response, it is believed that local neuronal survivability will greatly increase (Biran et al. 2005). Improving the electrical characteristics of the recording sites can serve to reduce recording noise, provide a more stable long-term signal, and improve tissue integration. Several approaches have shown promising results, including local and peripheral drug delivery, surface modifications to the implanted probes, recording site specific coatings, the use of novel probe materials, and modified probe architectures.

1.4.1 Drug Release

One of the most well explored ways of reducing tissue inflammation has been through the use of drugs. A commonly delivered drug has been dexamethasone, an anti-inflammatory glucocorticoid (Kim & Martin 2006; Willerth & Sakiyama-Elbert 2007). Initially, dexamethasone was delivered globally through an injection in the periphery (Shain et al. 2003); however, this is an ineffective method of delivering a drug particularly one targeted to such a small area in the brain. Newer, more novel techniques for delivering dexamethasone have been demonstrated both *in vivo* and *in vitro*. Actuating conductive hollow tubes of poly(3,4-ethylenedioxythiophene) (PEDOT) loaded with poly(lactic-co-glycolic acid) (PLGA) and dexamethasone have shown the ability to release the drug at the implant site (Abidian et al. 2006). Others have taken a more passive approach by utilizing PLGA nanoparticles, loaded with dexamethasone, that have been imbedded in a hydrogel that is then dehydrated. Upon insertion into the brain, the

hydrogel rehydrates allowing for the outward diffusion of dexamethasone into the surrounding tissue (Kim & Martin 2006). Porous silicon has also been used to load and release dexamethasone using a passive approach (Sun et al. 2014). Most importantly, the release of dexamethasone *in vivo* has been shown to reduce long-term astrocytic activity (Shain et al. 2003; Zhong & Bellamkonda 2007). More experimental approaches that have not been proven in a long-term setting include the release of α-melanocyte stimulating hormone (α-MSH) from a nitrocellulose polymer matrix (Zhong & Bellamkonda 2005) and the secretion of nerve growth factor from a hydrogel of poly(ethylene glycol)-poly(lactic acid) (Winter et al. 2007). These treatments, though effective in the short term, have not demonstrated long-term viability as the eluted drug is finite in quantity and thus has a limited efficacy.

1.4.2 Surface Modifications

Altering the surface properties of an implanted device can be one of the most potent options to encourage neuronal growth and reduce inflammation. In permanently modifying the surface of a probe no actual molecule is consumed. Instead, the bound motif stays on the surface and continually interacts with neighboring cells. Different groups have shown promising results in immobilizing agents such as transforming growth factor β1 (TGF-β1) (Klaver & Caplan 2007), α-MSH (He et al. 2007), laminin (Klaver & Caplan 2007), and neural adhesion molecule L1 coupled with polyethylene glycol (Azemi et al. 2008) on the probe surface. Molecules such as TGF-β1 and α-MSH interact with receptors on the cell's surface and are positioned in a particular orientation to have an effect. Therefore, one of the major drawbacks to this approach is a requirement that the immobilized molecule be positioned in the correct manner to interact

with cellular receptors. Not all drugs or proteins are amenable to this technique which leads to a restricted set of candidate therapies. Few studies have demonstrated long term improvement in recording quality and instead rely on histology to prove the underlying principles of reduced encapsulation.

An alternative approach to the immobilization of drugs or growth factors is the use of anti-fouling molecules (Katira et al. 2007; Gutowski et al. 2014). This technique aims to reduce the amount of adsorbed protein on the probe surface, which can act as a signaling mechanism for the inflammatory cascade. Many explanted probes have shown, through staining, an adherence of proteins or protein markers associated with glial scarring (Biran et al. 2005; Grand et al. 2010). One such anti-fouling coating is poly(ethylene glycol) methacrylate (PEGMA) which is a hydrophobic surface and has been shown to be protein resistant (Katira et al. 2007). To create such a barrier, first a surface is coated with poly[(p-xylylene-4-methyl-2-bromoisobutyrate)-co-(p-xylylene)], followed by atom transfer radical polymerization which leads to the deposition of PEGMA (Lahann 2006; Jiang et al. 2008). While this is a promising avenue, there have been limited studies that actually apply this technique to functioning neural probes. In addition, if a coating were successfully applied it would only mitigate signaling caused by proteins on the probes surface and would not address signaling induced by a leaking vasculature.

1.4.3 Electrode Site Coatings

Directly modifying electrode recording sites can serve as an alternative to local drug or surface immobilization intervention strategies. Typically, site coatings lower the impedance of the recording electrode which will also reduce the baseline thermal noise

and allow for previously undetectable units to be detected (Ludwig et al. 2006; Arcot Desai et al. 2010; Lempka et al. 2011). Coatings such as PEDOT doped with either sodium p-toluenesulfonate (Green et al. 2012) or carbon nanotubes (Zhou et al. 2013; Luo et al. 2011; Kolarcik et al. 2015), or polypyrrole doped with a CDPGYIGSR nonapeptide (Cui et al. 2001), can lower site impedance and improve cell viability and neuronal adhesion. Alternatively, site coatings used to lower impedance can also incorporate additional molecules, such as nerve growth factor, that improve integration with surrounding neuronal cells (Green et al. 2010). Unfortunately, these methods have only shown neuronal adhesion and viability with cell culture studies (Green et al. 2012; Green et al. 2010; Zhou et al. 2013; Luo et al. 2011; Cui et al. 2001) or implants that lasted for 17 days (Kolarcik et al. 2015), neither of which is definitive proof that these coatings will be effective for multi-month implants.

1.4.4 Novel Probe Materials

It has been shown both experimentally and through simulations that more flexible probes will lead to less strain on the surrounding tissue and potentially less inflammation (Subbaroyan & Kipke 2006; Subbaroyan et al. 2005). Most designs attempt to capitalize on this phenomenon by using materials with a low Young's modulus that more closely matches the brain's own Young's modulus. A smaller difference in mechanical mismatch will in theory lead to less inflammation of the surrounding tissue.

A commonly used material for developing soft electrodes is polyimide, a biocompatible material with a Young's modulus of 2.8 GPa (Rousche et al. 2001). Polyimide based electrodes can be patterend and fabricated using standard cleanroom techniques (Rousche et al. 2001). Over the past decade and a half, many groups have

developed their own neural probe technologies centered around polyimide (Rousche et al. 2001; Mercanzini et al. 2008; Lai et al. 2012; Sankar et al. 2013; Xiang et al. 2014; Jeon et al. 2014; Cheung et al. 2007). Other groups have focused on the use of parylene-c as an electrode material (Kuo et al. 2013; Takeuchi et al. 2005).

Creating an electrode from softer materials often leads to insertion difficuties as the large devices are unlikely to overcome the critical force needed to penetrate the brain (Najafi & Hetke 1990; Wester et al. 2009; Harris, Hess, et al. 2011). This can be alleviated by covering the electrode in a dissolvable coating that temporarily stiffens the device (Xiang et al. 2014; Takeuchi et al. 2005; Jeon et al. 2014). More novel materials made from polymer nanocomposites (NCs) have the ability to change from a stiff material (~5 GPa) prior to brain insertion to a more flexible material (~12 MPa) upon insertion into the brain (Harris, Capadona, et al. 2011; Harris, Hess, et al. 2011). A similar dual Young's modulus approach has been utilized with thiol-ene/acrylate polymer electrodes which decrease from 1 GPa to 12 MPa, post-implantation (Ware et al. 2012; Ware et al. 2014).

Acute testing of these novel electrode materials shows the feasibility of such designs; however, many of the electrodes have yet to show multi-month chronic viability with electrophysiology data. The few that have undergone more extensive testing show little evidence of their superiority over traditional silicon electrodes in a chronic setting (Rousche et al. 2001; Takeuchi et al. 2004; Cheung et al. 2007). Other devices, such as the non-functional NCs, show improved neuronal density surrounding the probe after four weeks when compared to a nanowire; however, this difference became negligible after eight weeks (Harris, Capadona, et al. 2011; Harris, Hess, et al. 2011).

1.4.5 Modified Neural Probe Architecture

While changes in material properties have shown modest success in improving the longevity of penetrating microelectrodes, the most profound effects in improving longevity have come from dramatically reducing the size of the electrodes. Initial work studying the effect of an electrode's cross-sectional area on tissue response showed no difference between large devices (16,000 μm^2) and small devices (1450 – 2500 μm^2) (Szarowski et al. 2003). These devices were likely not small enough as later studies investigated much smaller values and found that devices with cross-sectional areas on the order of 100s of μm^2 showed significant increases in neuronal survivability (Karumbaiah et al. 2013; Seymour & Kipke 2007; Skousen et al. 2011) and reductions in tissue inflammation (Karumbaiah et al. 2013; Stice et al. 2007; Seymour & Kipke 2007; Skousen et al. 2011). The works by Skousen et al. and Seymour et al. used silicon and parylene-c respectively to fabricate their devices. These materials differ in Young's moduli by approximately 1.7 orders of magnitude (Wester et al. 2009; Dolbow & Gosz 1996) which points to size and not material as being a more crucial factor in improving microelectrode longevity.

An ideal microelectrode would be made from a material that is extremely strong, such that it can penetrate the brain during insertion (Najafi & Hetke 1990; Wester et al. 2009; Harris, Hess, et al. 2011), as well as be extremely small, to avoid causing both short and long-term tissue damage. The use of carbon fibers as an electrode substrate can meet both needs. Carbon fibers have long been used in neuroscience studies to record extracellular potentials in acute preparations (Armstrong-James & Millar 1979), as well as detect neurotransmitter levels in both animals (Ponchon et al. 1979; Rebec et al. 1997; Park et al. 2011) and slice work (Heien et al. 2004; Ferris et al. 2013). The traditional use

of a pulled glass capillary as an insulating layer for carbon fiber electrodes (Armstrong-James & Millar 1979) would be impractical for chronic implantation. This has led groups to seek out new coatings, such as parylene-c (Kozai et al. 2012; Guitchounts et al. 2013), to serve as an insulation layer. Fully functionalized single carbon fiber microelectrodes, insulated with parylene-c and tip coated with PEDOT:polystyrene sulfonate have been implanted and shown to work *in vivo* (Kozai et al. 2012). Other groups have developed and chronically implanted carbon fiber electrodes that form a 4 x 4 tetrode-like bundle, with an overall cross-sectional width of 26 µm (Guitchounts et al. 2013).

The reduced size of carbon fiber electrodes also make it one of the most flexible designs to date. The flexibility of a probe factors in both the material's Young's modulus and the physical dimensions of a probe. This metric, flexibility, can be represented by the spring constant of a cantilever beam. Neural probes are best modeled as a beam fixed only at one end which has a spring constant of $k = \frac{3EI}{l^3}$, where E = Young's modulus, I = moment of inertia, and l = length of the beam. For a cylindrical beam, such as a carbon fiber, the moment of inertia is calculated as $\frac{\pi r^4}{4}$, where r = radius of the cylinder. For a rectangular prism which best approximates traditional probe geometries the moment of inertia is calculated as $\frac{wt^3}{12}$ where w = width of the beam and t is the thickness of the beam. Table 1.1 uses the previous equations to calculate the spring constants for various probe designs proposed and used throughout the literature.

Probe Design/Material	E (MPa)	Length (mm)	Width (μm)	Thickness (μm)	k (mN/m)
Carbon Fiber (MatWeb 2012; Kozai et al. 2012)	241,000	5	6.8 (diameter)	N/A	0.61
Nanocomposites (before implant) (Harris, Capadona, et al. 2011; Harris, Hess, et al. 2011)	5,000	3	203	100	9398.15
Nanocomposites (after implant) (Harris, Capadona, et al. 2011; Harris, Hess, et al. 2011)	12	3	203	100	22.56
Silicon (Olsen et al. 2012; Dolbow & Gosz 1996)	165,000	3	123	15	136.99
Polyimide (Rousche et al. 2001)	2,800	1.5	160	20	265.48
Parylene-c (Wester et al. 2009)	3,778	2.5	100	25	94.5
Open Architecture (non-functional) - Parylene-c (Seymour & Kipke 2007)	3,778	1.1	4	5	0.26
Tungsten (Lassner & Schubert 1999; Ward et al. 2009)	390,000	2	50 (diameter)	N/A	44,868

Table 1.1. Physical properties of various probe designs.

Although the carbon fibers have one of the highest Young's moduli, compounding the potential issue of mechanical mismatch with the brain, when the actual size of the electrode is taken into account, they have superior flexibility. All other probe technologies, except for the open architecture style, are hindered by either their large non-length dimensions, Young's modulus, or a combination of both. While the open-architecture style has a lower theoretical flexibility, it is important to note that a permanently attached shuttle was required to insert this non-functional device, and therefore its actual flexibility would be greatly diminished. The low spring constant of carbon fibers increases the ability of this electrode to move with the brain during micromotion (Gilletti & Muthuswamy 2006; Muthuswamy et al. 2003) and potential traumatic movements induced by a concussive force.

1.5 Dissertation Organization

The aim of this work is to develop, validate, and characterize the insertion mechanism, tissue response, and recording longevity of a new high-density carbon fiber microelectrode array. This technology was designed to significantly improve the field of

penetrating microelectrodes while simultaneously accommodating the variable needs of both neuroscientists and neural engineers. To provide a comprehensive and accurate depiction of device viability all studies utilized the most relevant and widely used *in vitro* and *in vivo* experimental models.

Chapter II presents the fabrication and insertion dynamics of a high-density carbon fiber electrode array using a dual sided printed circuit board platform. The use of this platform has pushed electrode density to limits not seen in other works. This necessitated the use of an encapsulation method that served to temporarily stiffen the fibers during insertion, but did not enter the brain as many other shuttles do for other probe designs (Kozai & Kipke 2009; Seymour & Kipke 2007). The initial findings in this work informed the development of an even higher density array using a silicon support structure as a backbone. This work has been tentatively accepted, with minor revisions, to the *Journal of Neural Engineering* (Patel et al. 2015).

Chapter III reports on the tissue reaction of chronically implanted carbon fiber electrodes arrays as compared to silicon electrodes. Due to their smaller footprint, the reactive response to carbon fibers should be greatly attenuated, if not non-existent. Tissue sections from multiple chronic implants of both probe types were stained for astrocytes, microglia, and neurons. Results show a scarring response to the implanted silicon electrode with elevated astrocyte and microglia activity coupled to a local decrease in neuronal density. The area implanted with the carbon fiber electrodes showed a varied response, from no detectable increase in astrocytic or microglial activity to an elevated activation of both cell types, but with no detectable scars. Neuronal density in the carbon fiber implant region was unaffected. The data demonstrates that the

small carbon fiber profile, even in an array configuration, shows an attenuated reactive response with no visible scaring.

Chapter IV reports the viability of chronically implanted high-density carbon fiber arrays as compared to more traditional silicon planar arrays with comparable site sizes. While most new probe technologies or designs are able to demonstrate proof of concept functionality in acute preparations, very few show the ability to record chronic unit activity. This study aims to provide a comprehensive analysis of electrophysiology data collected over implant durations ranging from 3 – 5 months. This work is currently in preparation for journal submission.

Chapter V provides a summary of the findings in this dissertation and offers insights into the future directions of this work and that of the field as a whole.

1.6 References

Abidian, M.R., Kim, D.H. & Martin, D.C., 2006. Conducting-polymer nanotubes for controlled drug release. *Advanced Materials*, 18(4), pp.405–409.

Acharya, R.U. et al., 2005. Non-linear analysis of EEG signals at various sleep stages. *Computer Methods and Programs in Biomedicine*, 80(1), pp.37–45.

Arcot Desai, S. et al., 2010. Improving impedance of implantable microwire multi-electrode arrays by ultrasonic electroplating of durable platinum black. *Frontiers in Neuroengineering*, 3, pp.1–5.

Armstrong-James, M. & Millar, J., 1979. Carbon fibre microelectrodes. *Journal of Neuroscience Methods*, 1(3), pp.279–287.

Azemi, E. et al., 2008. Surface immobilization of neural adhesion molecule L1 for improving the biocompatibility of chronic neural probes: In vitro characterization. *Acta Biomaterialia*, 4(5), pp.1208–1217.

Barrese, J.C. et al., 2013. Failure mode analysis of silicon-based intracortical microelectrode arrays in non-human primates. *Journal of Neural Engineering*, 10(6), p.66014.

Bell, C.J. et al., 2008. Control of a humanoid robot by a noninvasive brain-computer interface in humans. *Journal of Neural Engineering*, 5(2), p.214.

Berényi, A. et al., 2014. Large-scale, high-density (up to 512 channels) recording of local circuits in behaving animals. *Journal of Neurophysiology*, 111(5), pp.1132–1149.

Berke, J.D., Breck, J.T. & Eichenbaum, H., 2009. Striatal Versus Hippocampal Representations During Win-Stay Maze Performance. *Journal of Neurophysiology*, 101(3), pp.1575–1587.

Bhandari, R. et al., 2009. A novel masking method for high aspect ratio penetrating microelectrode arrays. *Journal of Micromechanics and Microengineering*, 19(3), p.35004.

Biran, R., Martin, D.C. & Tresco, P.A., 2005. Neuronal cell loss accompanies the brain tissue response to chronically implanted silicon microelectrode arrays. *Experimental Neurology*, 195(1), pp.115–126.

Biran, R., Martin, D.C. & Tresco, P.A., 2007. The brain tissue response to implanted silicon microelectrode arrays is increased when the device is tethered to the skull. *Journal of Biomedical Materials Research Part A*, 82(1), pp.169–178.

Branner, A., Stein, R.B. & Normann, R.A., 2001. Selective Stimulation of Cat Sciatic Nerve Using an Array of Varying-Length Microelectrodes. *Journal of Neurophysiology*, 85(4), pp.1585–1594.

Burmeister, J.J. et al., 2002. Improved ceramic-based multisite microelectrode for rapid measurements of L-glutamate in the CNS. *Journal of Neuroscience Methods*, 119(2), pp.163–171.

Campbell, P.K. et al., 1991. A Silicon-Based, Three-Dimensional Neural Interface - Manufacturing Processes For An Intracortical Electrode Array. *IEEE Transactions On Biomedical Engineering*, 38(8), pp.758–768.

Carmena, J.M. et al., 2003. Learning to control a brain-machine interface for reaching and grasping by primates. *PLoS Biology*, 1(2), pp.193–208.

Carter, R.R. & Houk, J.C., 1993. Multiple single-unit recordings from the CNS using thin-film electrode arrays. *IEEE Transactions on Rehabilitation Engineering*, 1(3), pp.175–184.

Chakravarty, D.N. & Faingold, C.L., 1998. Comparison of neuronal response patterns in the external and central nuclei of inferior colliculus during ethanol administration and ethanol withdrawal. *Brain Research*, 783(1), pp.102–108.

Chestek, C.A. et al., 2013. Hand posture classification using electrocorticography signals in the gamma band over human sensorimotor brain areas. *Journal of Neural Engineering*, 10(2), p.26002.

Chestek, C.A. et al., 2011. Long-term stability of neural prosthetic control signals from silicon cortical arrays in rhesus macaque motor cortex. *Journal of Neural Engineering*, 8(4), p.45005.

Cheung, K.C. et al., 2007. Flexible polyimide microelectrode array for in vivo recordings and current source density analysis. *Biosensors and Bioelectronics*, 22(8), pp.1783–1790.

Cheung, K.C., 2007. Implantable microscale neural interfaces. *Biomedical Microdevices*, 9(6), pp.923–938.

Cohen, J.Y. et al., 2012. Neuron-type-specific signals for reward and punishment in the ventral tegmental area. *Nature*, 482, pp.85–88.

Collinger, J.L. et al., 2013. High-performance neuroprosthetic control by an individual with tetraplegia. *The Lancet*, 381(9866), pp.557–564.

Cragg, B.G., 1967. The density of synapses and neurones in the motor and visual areas of the cerebral cortex. *Journal of Anatomy*, 101(Pt 4), pp.639–654.

Cui, X. et al., 2001. Surface modification of neural recording electrodes with conducting polymer/biomolecule blends. *Journal of Biomedical Materials Research*, 56(2), pp.261–272.

Davidson, T.J., Kloosterman, F. & Wilson, M.A., 2009. Hippocampal Replay of Extended Experience. *Neuron*, 63(4), pp.497–507.

Dolbow, J. & Gosz, M., 1996. Effect of out-of-plane properties of a polyimide film on the stress fields in microelectronic structures. *Mechanics of Materials*, 23(4), pp.311–321.

Donoghue, J.P., 2002. Connecting cortex to machines: recent advances in brain interfaces. *Nature Neuroscience*, 5, pp.1085–1088.

Edell, D.J. et al., 1992. Factors influencing the biocompatibility of insertable silicon microshafts in cerebral cortex. *IEEE Transactions on Biomedical Engineering*, 39(6), pp.635–643.

Ersen, A. et al., 2015. Chronic tissue response to untethered microelectrode implants in the rat brain and spinal cord. *Journal of Neural Engineering*, 12(1), p.16019.

Feinberg, I. & Campbell, I.G., 2010. Sleep EEG changes during adolescence: An index of a fundamental brain reorganization. *Brain and Cognition*, 72(1), pp.56–65.

Ferris, M.J. et al., 2013. Examining the Complex Regulation and Drug-Induced Plasticity of Dopamine Release and Uptake Using Voltammetry in Brain Slices. *ACS Chemical Neuroscience*, 4(5), pp.693–703.

Frey, O. et al., 2011. Biosensor microprobes with integrated microfluidic channels for bi-directional neurochemical interaction. *Journal of Neural Engineering*, 8(6), p.66001.

Frey, O. et al., 2010. Enzyme-based choline and L-glutamate biosensor electrodes on silicon microprobe arrays. *Biosensors and Bioelectronics*, 26(2), pp.477–484.

Gage, G.J. et al., 2006. Laminar Analysis of Movement Direction Information in Local Field Potentials of the Rat Motor Cortex. *2006 Annual International Conference of the IEEE Engineering In Medicine and Biology Society*, pp.2589–2592.

Gilletti, A. & Muthuswamy, J., 2006. Brain micromotion around implants in the rodent somatosensory cortex. *Journal of Neural Engineering*, 3(3), p.189.

Grand, L. et al., 2010. Short and long term biocompatibility of NeuroProbes silicon probes. *Journal of Neuroscience Methods*, 189(2), pp.216–229.

Gray, C.M. et al., 1995. Tetrodes markedly improve the reliability and yield of multiple single-unit isolation from multi-unit recordings in cat striate cortex. *Journal of Neuroscience Methods*, 63(1-2), pp.43–54.

Green, R.A. et al., 2012. Substrate dependent stability of conducting polymer coatings on medical electrodes. *Biomaterials*, 33(25), pp.5875–5886.

Green, R.A., Lovell, N.H. & Poole-Warren, L.A., 2010. Impact of co-incorporating laminin peptide dopants and neurotrophic growth factors on conducting polymer properties. *Acta Biomaterialia*, 6(1), pp.63–71.

Guilian, D. et al., 1993. Reactive Mononuclear Phagocytes Release Neurotoxins After Ischemic and Traumatic Injury To the Central-nervous-system. *Journal of Neuroscience Research*, 36(6), pp.681–693.

Guitchounts, G. et al., 2013. A carbon-fiber electrode array for long-term neural recording. *Journal of Neural Engineering*, 10(4), p.46016.

Gutowski, S.M. et al., 2014. Host response to microgel coatings on neural electrodes implanted in the brain. *Journal of Biomedical Materials Research Part A*, 102(5), pp.1486–1499.

Harris, J.P., Hess, A.E., et al., 2011. In vivo deployment of mechanically adaptive nanocomposites for intracortical microelectrodes. *Journal of Neural Engineering*, 8(4), p.46010.

Harris, J.P., Capadona, J.R., et al., 2011. Mechanically adaptive intracortical implants improve the proximity of neuronal cell bodies. *Journal of Neural Engineering*, 8(6), p.66011.

He, W. et al., 2007. A Novel Anti-inflammatory Surface for Neural Electrodes. *Advanced Materials*, 19(21), pp.3529–3533.

Heien, M.L.A. V, Johnson, M.A. & Wightman, R.M., 2004. Resolving neurotransmitters detected by fast-scan cyclic voltammetry. *Analytical Chemistry*, 76(19), pp.5697–5704.

Hochberg, L.R. et al., 2006. Neuronal ensemble control of prosthetic devices by a human with tetraplegia. *Nature*, 442(7099), pp.164–171.

Hochberg, L.R. et al., 2012. Reach and grasp by people with tetraplegia using a neurally controlled robotic arm. *Nature*, 485(7398), pp.372–375.

Hoffmann, U. et al., 2008. An efficient P300-based brain-computer interface for disabled subjects. *Journal of Neuroscience Methods*, 167(1), pp.115–125.

Im, M. et al., 2011. Neural Probes with optical mixer/splitter waveguides and multiple stimulation sites. *2011 IEEE 24th International Conference on Micro Electro Mechanical Systems*, pp.1051–1054.

Jeon, M. et al., 2014. Partially flexible MEMS neural probe composed of polyimide and sucrose gel for reducing brain damage during and after implantation. *Journal of Micromechanics and Microengineering*, 24(2), p.25010.

Jiang, X. et al., 2008. Vapor-based initiator coatings for atom transfer radical polymerization. *Advanced Functional Materials*, 18(1), pp.27–35.

Johnson, M.D. et al., 2008. Implantable microelectrode arrays for simultaneous electrophysiological and neurochemical recordings. *Journal of Neuroscience Methods*, 174(1), pp.62–70.

Johnson, M.D. et al., 2005. Neural Probes for Concurrent Detection of Neurochemical and Electrophysiological Signals in vivo. *2005 Annual International Conference of the IEEE Engineering In Medicine and Biology Society*, pp.7325–7328.

Johnson, M.D., Kao, O.E. & Kipke, D.R., 2007. Spatiotemporal pH dynamics following insertion of neural microelectrode arrays. *Journal of Neuroscience Methods*, 160(2), pp.276–287.

Karumbaiah, L. et al., 2013. Relationship between intracortical electrode design and chronic recording function. *Biomaterials*, 34(33), pp.8061–8074.

Katira, P. et al., 2007. Quantifying the performance of protein-resisting surfaces at ultra-low protein coverages using kinesin motor proteins as probes. *Advanced Materials*, 19(20), pp.3171–3176.

Khodagholy, D. et al., 2015. NeuroGrid: recording action potentials from the surface of the brain. *Nature Neuroscience*, 18(2), pp.310–315.

Kim, B.J. et al., 2013. 3D Parylene sheath neural probe for chronic recordings. *Journal of Neural Engineering*, 10(4), p.45002.

Kim, D.-H. & Martin, D.C., 2006. Sustained release of dexamethasone from hydrophilic matrices using PLGA nanoparticles for neural drug delivery. *Biomaterials*, 27(15), pp.3031–3037.

Kipke, D.R. et al., 2003. Silicon-substrate intracortical microelectrode arrays for long-term recording of neuronal spike activity in cerebral cortex. *IEEE Transactions on Neural Systems and Rehabilitation Engineering*, 11(2), pp.151–155.

Klaver, C.L. & Caplan, M.R., 2007. Bioactive surface for neural electrodes: Decreasing astrocyte proliferation via transforming growth factor-β1. *Journal of Biomedical Materials Research Part A*, 81A(4), pp.1011–1016.

Kolarcik, C.L. et al., 2015. Evaluation of poly(3,4-ethylenedioxythiophene)/carbon nanotube neural electrode coatings for stimulation in the dorsal root ganglion. *Journal of Neural Engineering*, 12(1), p.16008.

Kozai, T.D.Y. et al., 2014. Effects of caspase-1 knockout on chronic neural recording quality and longevity: Insight into cellular and molecular mechanisms of the reactive tissue response. *Biomaterials*, 35(34), pp.9255–9268.

Kozai, T.D.Y. et al., 2010. Reduction of neurovascular damage resulting from microelectrode insertion into the cerebral cortex using in vivo two-photon mapping. *Journal of Neural Engineering*, 7(4), p.46011.

Kozai, T.D.Y. et al., 2012. Ultrasmall implantable composite microelectrodes with bioactive surfaces for chronic neural interfaces. *Nature Materials*, 11(12), pp.1065–1073.

Kozai, T.D.Y. & Kipke, D.R., 2009. Insertion shuttle with carboxyl terminated self-assembled monolayer coatings for implanting flexible polymer neural probes in the brain. *Journal of Neuroscience Methods*, 184(2), pp.199–205.

Kuo, J.T.W. et al., 2013. Novel flexible Parylene neural probe with 3D sheath structure for enhancing tissue integration. *Lab On A Chip*, 13, pp.554–561.

Lahann, J., 2006. Vapor-based polymer coatings for potential biomedical applications. *Polymer International*, 55(12), pp.1361–1370.

Lai, H.-Y. et al., 2012. Design, simulation and experimental validation of a novel flexible neural probe for deep brain stimulation and multichannel recording. *Journal of Neural Engineering*, 9(3), p.36001.

Lassner, E. & Schubert, W.-D., 1999. *Tungsten: properties, chemistry, technology of the element, alloys, and chemical compounds*, Springer.

Lauer, R.T., Peckham, P.H. & Kilgore, K.L., 1999. EEG-based control of a hand grasp neuroprosthesis. *Neuroreport*, 10(8), pp.1767–1771.

Lebedev, M.A. & Nicolelis, M.A.L., 2006. Brain-machine interfaces: past, present and future. *Trends in Neurosciences*, 29(9), pp.536–546.

Lempka, S.F. et al., 2011. Theoretical analysis of intracortical microelectrode recordings. *Journal of Neural Engineering*, 8(4), p.45006.

Leuthardt, E.C. et al., 2004. A brain-computer interface using electrocorticographic signals in humans. *Journal of Neural Engineering*, 1(2), p.63.

Leuthardt, E.C. et al., 2011. Using the electrocorticographic speech network to control a brain-computer interface in humans. *Journal of Neural Engineering*, 8(3), p.36004.

Liao, Y.-F. et al., 2011. A simple method for fabricating microwire tetrode with sufficient rigidity and integrity without a heat-fusing process. *Journal of Neuroscience Methods*, 195(2), pp.211–215.

Liu, X. et al., 1999. Stability of the interface between neural tissue and chronically implanted intracortical microelectrodes. *IEEE Transactions on Rehabilitation Engineering*, 7(3), pp.315–326.

Ludwig, K.A. et al., 2006. Chronic neural recordings using silicon microelectrode arrays electrochemically deposited with a poly(3,4-ethylenedioxythiophene) (PEDOT) film. *Journal of Neural Engineering*, 3(1), pp.59–70.

Luo, X. et al., 2011. Highly stable carbon nanotube doped poly(3,4-ethylenedioxythiophene) for chronic neural stimulation. *Biomaterials*, 32(24), pp.5551–5557.

MatWeb, 2012. Cytec Thornel® T-650/35 3K Carbon Fiber, Polyacrylonitrile (PAN) Precursor. Available at:

http://www.matweb.com/search/DataSheet.aspx?MatGUID=7e9aca60a2e84538a4e8038784f2b629&ckck=1.

Maynard, E.M., Nordhausen, C.T. & Normann, R.A., 1997. The Utah Intracortical Electrode Array: A recording structure for potential brain-computer interfaces. *Electroencephalography and Clinical Neurophysiology*, 102(3), pp.228–239.

McConnell, G.C. et al., 2009. Implanted neural electrodes cause chronic, local inflammation that is correlated with local neurodegeneration. *Journal of Neural Engineering*, 6(5), p.56003.

Mercanzini, A. et al., 2008. Demonstration of cortical recording using novel flexible polymer neural probes. *Sensors and Actuators A: Physical*, 143(1), pp.90–96.

Moxon, K.A. et al., 2004. Nanostructured surface modification of ceramic-based microelectrodes to enhance biocompatibility for a direct brain-machine interface. *IEEE Transactions on Biomedical Engineering*, 51(6), pp.881–889.

Musumeci, S.A. et al., 1999. Epilepsy and EEG Findings in Males with Fragile X Syndrome. *Epilepsia*, 40(8), pp.1092–1099.

Muthuswamy, J. et al., 2003. Microactuated neural probes to compensate for brain micromotion. *2003 Annual International Conference of the IEEE Engineering In Medicine and Biology Society*, 2, pp.1941–1943.

Najafi, K. & Hetke, J.F., 1990. Strength characterization of silicon microprobes in neurophysiological tissues. *IEEE Transactions on Biomedical Engineering*, 37(5), pp.474–481.

Najafi, K., Wise, K.D. & Mochizuki, T., 1985. A high-yield IC-compatible multichannel recording array. *IEEE Transactions on Electron Devices*, 32(7), pp.1206–1211.

Negi, S. et al., 2010. In vitro comparison of sputtered iridium oxide and platinum-coated neural implantable microelectrode arrays. *Biomedical Materials*, 5(1), p.15007.

Nicolelis, M.A.L. et al., 2003. Chronic, multisite, multielectrode recordings in macaque monkeys. *Proceedings of the National Academy of Sciences*, 100(19), pp.11041–11046.

Noachtar, S. & Rémi, J., 2009. The role of EEG in epilepsy: A critical review. *Epilepsy & Behavior*, 15(1), pp.22–33.

Nordhausen, C.T., Maynard, E.M. & Normann, R.A., 1996. Single unit recording capabilities of a 100 microelectrode array. *Brain Research*, 726(1-2), pp.129–140.

Normann, R.A. et al., 1999. A neural interface for a cortical vision prosthesis. *Vision Research*, 39(15), pp.2577–2587.

Olsen, S.R. et al., 2012. Gain control by layer six in cortical circuits of vision. *Nature*, 483(7387), pp.47–52.

Otto, K.J., Johnson, M.D. & Kipke, D.R., 2006. Voltage pulses change neural interface properties and improve unit recordings with chronically implanted microelectrodes. *IEEE Transactions on Biomedical Engineering*, 53(2), pp.333–340.

Parikh, H., Marzullo, T.C. & Kipke, D.R., 2009. Lower layers in the motor cortex are more effective targets for penetrating microelectrodes in cortical prostheses. *Journal of Neural Engineering*, 6(2), p.26004.

Park, J., Takmakov, P. & Wightman, R.M., 2011. In vivo comparison of norepinephrine and dopamine release in rat brain by simultaneous measurements with fast-scan cyclic voltammetry. *Journal of Neurochemistry*, 119(5), pp.932–944.

Patel, P.R. et al., 2015. Insertion of linear 8.4 μm diameter 16 channel carbon fiber electrode arrays for single unit recordings. *Journal of Neural Engineering*, (accepted with minor revisions).

Polikov, V.S., Tresco, P.A. & Reichert, W.M., 2005. Response of brain tissue to chronically implanted neural electrodes. *Journal of Neuroscience Methods*, 148(1), pp.1–18.

Ponchon, J.L. et al., 1979. Normal Pulse Polarography With Carbon-fiber Electrodes For Invitro and Invivo Determination of Catecholamines. *Analytical Chemistry*, 51(9), pp.1483–1486.

Potter, K.A. et al., 2012. Stab injury and device implantation within the brain results in inversely multiphasic neuroinflammatory and neurodegenerative responses. *Journal of Neural Engineering*, 9(4), p.46020.

Prasad, A. et al., 2014. Abiotic-biotic characterization of Pt/Ir microelectrode arrays in chronic implants. *Frontiers in neuroengineering*, 7, pp.1–15.

Prasad, A. & Sanchez, J.C., 2012. Quantifying long-term microelectrode array functionality using chronic in vivo impedance testing. *Journal of Neural Engineering*, 9(2), p.26028.

Rebec, G. V et al., 1997. Regional and temporal differences in real-time dopamine efflux in the nucleus accumbens during free-choice novelty. *Brain Research*, 776(1-2), pp.61–67.

Rennaker, R.L., Street, S., et al., 2005. A comparison of chronic multi-channel cortical implantation techniques: manual versus mechanical insertion. *Journal of Neuroscience Methods*, 142(2), pp.169–176.

Rennaker, R.L., Ruyle, A.M., et al., 2005. An economical multi-channel cortical electrode array for extended periods of recording during behavior. *Journal of Neuroscience Methods*, 142(1), pp.97–105.

Riemann, D., Berger, M. & Voderholzer, U., 2001. Sleep and depression - results from psychobiological studies: an overview. *Biological Psychology*, 57(1-3), pp.67–103.

Rohatgi, P. et al., 2009. In vivo performance of a microelectrode neural probe with integrated drug delivery. *Neurosurgical Focus*, 27(1), pp.E8–E8.

Rousche, P.J. et al., 2001. Flexible polyimide-based intracortical electrode arrays with bioactive capability. *IEEE Transactions on Biomedical Engineering*, 48(3), pp.361–371.

Royer, S. et al., 2010. Distinct Representations and Theta Dynamics in Dorsal and Ventral Hippocampus. *Journal of Neuroscience*, 30(5), pp.1777–1787.

Sankar, V. et al., 2013. A highly compliant serpentine shaped polyimide interconnect for front-end strain relief in chronic neural implants. *Frontiers in Neurology*, 4(124), pp.1–11.

Sawyer, A.J. et al., 2014. The effect of inflammatory cell-derived MCP-1 loss on neuronal survival during chronic neuroinflammation. *Biomaterials*, 35(25), pp.6698–6706.

Saxena, T. et al., 2013. The impact of chronic blood-brain barrier breach on intracortical electrode function. *Biomaterials*, 34(20), pp.4703–4713.

Schmidt, S., Horch, K. & Normann, R., 1993. Biocompatibility of Silicon-based Electrode Arrays Implanted In Feline Cortical Tissue. *Journal of Biomedical Materials Research*, 27(11), pp.1393–1399.

Schwartz, A.B. et al., 2006. Brain-Controlled Interfaces: Movement Restoration with Neural Prosthetics. *Neuron*, 52(1), pp.205–220.

Self, M.W. et al., 2014. Orientation-Tuned Surround Suppression in Mouse Visual Cortex. *Journal of Neuroscience*, 34(28), pp.9290–9304.

Seymour, J.P. & Kipke, D.R., 2007. Neural probe design for reduced tissue encapsulation in CNS. *Biomaterials*, 28(25), pp.3594–3607.

Shain, W. et al., 2003. Controlling cellular reactive responses around neural prosthetic devices using peripheral and local intervention strategies. *IEEE Transactions on Neural Systems and Rehabilitation Engineering*, 11(2), pp.186–188.

Sharma, A. et al., 2011. Long term in vitro functional stability and recording longevity of fully integrated wireless neural interfaces based on the Utah Slant Electrode Array. *Journal of Neural Engineering*, 8(4), p.45004.

Simeral, J.D. et al., 2011. Neural control of cursor trajectory and click by a human with tetraplegia 1000 days after implant of an intracortical microelectrode array. *Journal of Neural Engineering*, 8(2), p.25027.

Skousen, J.L. et al., 2011. Reducing surface area while maintaining implant penetrating profile lowers the brain foreign body response to chronically implanted planar silicon microelectrode arrays. *Progress in Brain Research*, 194, pp.167–180.

Smith, J.A. et al., 2012. Role of pro-inflammatory cytokines released from microglia in neurodegenerative diseases. *Brain Research Bulletin*, 87(1), pp.10–20.

Smith, S.J.M., 2005. EEG in the diagnosis, classification, and management of patients with epilepsy. *Journal of Neurology, Neurosurgery & Psychiatry*, 76(suppl 2), pp.ii2–ii7.

Sridharan, A., Rajan, S.D. & Muthuswamy, J., 2013. Long-term changes in the material properties of brain tissue at the implant-tissue interface. *Journal of Neural Engineering*, 10(6), p.66001.

Steiger, A. & Kimura, M., 2010. Wake and sleep EEG provide biomarkers in depression. *Journal of Psychiatric Research*, 44(4), pp.242–252.

Stice, P. et al., 2007. Thin microelectrodes reduce GFAP expression in the implant site in rodent somatosensory cortex. *Journal of Neural Engineering*, 4(2), p.42.

Strumwasser, F., 1958. Long-term Recording From Single Neurons In Brain of Unrestrained Mammals. *Science*, 127(3296), pp.469–470.

Subbaroyan, J. & Kipke, D.R., 2006. The role of flexible polymer interconnects in chronic tissue response induced by intracortical microelectrodes - a modeling and an in vivo study. *2006 Annual International Conference of the IEEE Engineering In Medicine and Biology Society*, pp.3588–3591.

Subbaroyan, J., Martin, D.C. & Kipke, D.R., 2005. A finite-element model of the mechanical effects of implantable microelectrodes in the cerebral cortex. *Journal of Neural Engineering*, 2(4), pp.103–113.

Sun, T., Tsang, W.M. & Park, W.-T., 2014. Drug release from porous silicon for stable neural interface. *Applied Surface Science*, 292, pp.843–851.

Szarowski, D.H. et al., 2003. Brain responses to micro-machined silicon devices. *Brain Research*, 983(1-2), pp.23–35.

Takeuchi, S. et al., 2004. 3D flexible multichannel neural probe array. *Journal of Micromechanics and Microengineering*, 14(1), pp.104–107.

Takeuchi, S. et al., 2005. Parylene flexible neural probes integrated with microfluidic channels. *Lab*, 5, pp.519–523.

Taylor, D.M., Tillery, S.I.H. & Schwartz, A.B., 2003. Information conveyed through brain-control: cursor versus robot. *IEEE Transactions on Neural Systems and Rehabilitation Engineering*, 11(2), pp.195–199.

Teplan, M., 2002. Fundamentals of EEG Measurement. *Measurement Science Review*, 2(2), pp.1–11.

Tseng, W.-T., Yen, C.-T. & Tsai, M.-L., 2011. A bundled microwire array for long-term chronic single-unit recording in deep brain regions of behaving rats. *Journal of Neuroscience Methods*, 201(2), pp.368–376.

Turner, J.N. et al., 1999. Cerebral Astrocyte Response to Micromachined Silicon Implants. *Experimental Neurology*, 156(1), pp.33–49.

Velliste, M. et al., 2008. Cortical control of a prosthetic arm for self-feeding. *Nature*, 453(7198), pp.1098–1101.

Vetter, R.J. et al., 2004. Chronic neural recording using silicon-substrate microelectrode arrays implanted in cerebral cortex. *IEEE Transactions on Biomedical Engineering*, 51(6), pp.896–904.

Vetter, R.J. et al., 2005. Development of a Microscale Implantable Neural Interface (MINI) Probe System. *2005 Annual International Conference of the IEEE Engineering In Medicine and Biology Society*, 7, pp.7341–7344.

Ward, M.P. et al., 2009. Toward a comparison of microelectrodes for acute and chronic recordings. *Brain Research*, 1282, pp.183–200.

Ware, T. et al., 2014. Thiol-ene/acrylate substrates for softening intracortical electrodes. *Journal of Biomedical Materials Research Part B: Applied Biomaterials*, 102(1), pp.1–11.

Ware, T. et al., 2012. Three-Dimensional Flexible Electronics Enabled by Shape Memory Polymer Substrates for Responsive Neural Interfaces. *Macromolecular Materials and Engineering*, 297(12), pp.1193–1202.

Wark, H.A.C. et al., 2013. A new high-density (25 electrodes/mm2) penetrating microelectrode array for recording and stimulating sub-millimeter neuroanatomical structures. *Journal of Neural Engineering*, 10(4), p.45003.

Wark, H.A.C. et al., 2014. Behavioral and cellular consequences of high-electrode count Utah Arrays chronically implanted in rat sciatic nerve. *Journal of Neural Engineering*, 11(4), p.46027.

Wester, B.A., Lee, R.H. & LaPlaca, M.C., 2009. Development and characterization of in vivo flexible electrodes compatible with large tissue displacements. *Journal of Neural Engineering*, 6(2), p.24002.

Willerth, S.M. & Sakiyama-Elbert, S.E., 2007. Approaches to neural tissue engineering using scaffolds for drug delivery. *Advanced Drug Delivery Reviews*, 59(4-5), pp.325–338.

Williams, J.C., Rennaker, R.L. & Kipke, D.R., 1999. Long-term neural recording characteristics of wire microelectrode arrays implanted in cerebral cortex. *Brain Research Protocols*, 4(3), pp.303–313.

Winslow, B.D. et al., 2010. A comparison of the tissue response to chronically implanted Parylene-C-coated and uncoated planar silicon microelectrode arrays in rat cortex. *Biomaterials*, 31, pp.9163–9172.

Winslow, B.D. & Tresco, P.A., 2010. Quantitative analysis of the tissue response to chronically implanted microwire electrodes in rat cortex. *Biomaterials*, 31(7), pp.1558–1567.

Winter, J.O., Cogan, S.F. & Rizzo, J.F., 2007. Neurotrophin-eluting hydrogel coatings for neural stimulating electrodes. *Journal of Biomedical Materials Research Part B: Applied Biomaterials*, 81B(2), pp.551–563.

Wise, K.D. et al., 2004. Wireless implantable microsystems: High-density electronic interfaces to the nervous system. *Proceedings of the IEEE*, 92(1), pp.76–97.

Wise, K.D. & Angell, J.B., 1975. A Low-Capacitance Multielectrode Probe for Use in Extracellular Neurophysiology. *IEEE Transactions on Biomedical Engineering*, BME-22(3), pp.212–219.

Wolpaw, J.R. et al., 1991. An EEG-based brain-computer interface for cursor control. *Electroencephalography and Clinical Neurophysiology*, 78(3), pp.252–259.

Wolpaw, J.R. & McFarland, D.J., 2004. Control of a two-dimensional movement signal by a noninvasive brain-computer interface in humans. *Proceedings of the National Academy of Sciences of the United States of America*, 101(51), pp.17849–17854.

Wu, F. et al., 2013. An implantable neural probe with monolithically integrated dielectric waveguide and recording electrodes for optogenetics applications. *Journal of Neural Engineering*, 10(5), p.56012.

Xiang, Z. et al., 2014. Ultra-thin flexible polyimide neural probe embedded in a dissolvable maltose-coated microneedle. *Journal of Micromechanics and Microengineering*, 24(6), p.65015.

Xie, X., Rieth, L., Williams, L., et al., 2014. Long-term reliability of Al2O3 and Parylene C bilayer encapsulated Utah electrode array based neural interfaces for chronic implantation. *Journal of Neural Engineering*, 11(2), p.26016.

Xie, X., Rieth, L., Negi, S., et al., 2014. Self-aligned tip deinsulation of atomic layer deposited Al2O3 and parylene C coated Utah electrode array based neural interfaces. *Journal of Micromechanics and Microengineering*, 24(3), p.35003.

Zhong, Y. & Bellamkonda, R. V, 2005. Controlled release of anti-inflammatory agent Î±-MSH from neural implants. *Journal of Controlled Release*, 106(3), pp.309–318.

Zhong, Y. & Bellamkonda, R. V, 2007. Dexamethasone-coated neural probes elicit attenuated inflammatory response and neuronal loss compared to uncoated neural probes. *Brain Research*, 1148(0), pp.15–27.

Zhou, H. et al., 2013. Poly(3,4-ethylenedioxythiophene)/multiwall carbon nanotube composite coatings for improving the stability of microelectrodes in neural prostheses applications. *Acta Biomaterialia*, 9(5), pp.6439–6449.

CHAPTER II

Insertion of Linear 8.4 µm Diameter 16 Channel Carbon Fiber Microelectrode Arrays for Single Unit Recordings

2.1 Abstract

Objective. Single carbon fiber electrodes (d=8.4 µm) insulated with parylene-c and functionalized with PEDOT:PSS have been shown to record single unit activity but manual implantation of these devices with forceps can be difficult. Without an improvement in the insertion method any increase in the channel count by fabricating carbon fiber arrays would be impractical. In this study, a water soluble coating and structural backbones are utilized to create, implant, and record from fully functionalized arrays of carbon fibers with ~150 µm pitch. *Approach.* Two approaches were tested for the insertion of carbon fiber arrays. The first method used a PEG coating that temporarily stiffened the fibers while leaving a small portion at the tip exposed. The small exposed portion (500 µm – 1 mm) readily penetrated the brain allowing for an insertion that did not require the handling of each fiber by forceps. The second method involved the fabrication of silicon support structures with individual shanks spaced 150 µm apart. Each shank consisted of a small groove that held an individual carbon fiber. *Main results.* Results showed that the PEG coating allowed for the chronic implantation

of carbon fiber arrays in 5 rats with unit activity detected at 31 days post-implant. The silicon support structures recorded single unit activity in 3 acute rat surgeries. In one of those surgeries a stacked device with 3 layers of silicon support structures and carbon fibers was built and shown to readily insert into the brain with unit activity on select sites. *Significance.* From these studies it was found that carbon fibers spaced at ~150 μm readily insert into the brain. This greatly increases the recording density of chronic neural probes and paves the way for even higher density devices that have a minimal scarring response.

2.2 Introduction

The ability to record simultaneous neural activity from large neuronal populations has had a far reaching impact in the fields of neuroscience (Nicolelis et al. 2003; Berényi et al. 2014) and neural prosthetics, including brain machine interfaces (BMIs) (Carmena et al. 2003; Simeral et al. 2011; Hochberg et al. 2006). These fields often employ the use of microelectrode arrays (MEAs) which can routinely record from dozens to several hundreds of electrodes simultaneously. MEAs are typically composed of silicon shanks, ideally at regular and closely spaced intervals, with one or more electrode recording sites on the individual shanks. Some of the earliest MEAs, and still widely used, are microwire arrays consisting of individually placed wires, typically arranged in a linear configuration (Schwartz 2004; Williams et al. 1999; Nicolelis et al. 2003; Rennaker et al. 2005). Other commonly used high channel MEAs include the Michigan probe (Vetter et al. 2004; Kipke et al. 2003; Kozai, Du, et al. 2015) and Utah array (Nordhausen et al. 1996; Wark et al. 2013; Barrese et al. 2013). While extremely popular in their use, all of these MEAs, and their respective applications, would benefit from greater spatial

sensitivity with more closely spaced shanks that can record from more neurons, damage less tissue, and last for decades.

A limiting factor in creating extremely high density arrays, particularly those that can be implanted long-term, is gliosis. The initial trauma endured by the brain tissue and local vasculature upon probe insertion (Johnson et al. 2007; Bjornsson et al. 2008; Kozai et al. 2010) can recover rapidly if the foreign object is either removed (Biran et al. 2005; Potter et al. 2012) or dissolves away (Kozai, Gugel, et al. 2014). However, when a probe is chronically implanted a persistent reactive response will take place. This reactive response is best characterized by a glial sheath or scar, surrounding the probe, composed of activated astrocytes and microglia (Edell et al. 1992; Carter & Houk 1993; Schmidt et al. 1993; Turner et al. 1999; Liu et al. 1999; Szarowski et al. 2003; Biran et al. 2005; Polikov et al. 2005; McConnell et al. 2009; Grand et al. 2010; Winslow & Tresco 2010; Kozai, Vazquez, et al. 2012). This scar can extend out to 250 µm for a typical 15 µm thick silicon shank electrode (Biran et al. 2005). In addition, the chronic glial sheath contributes to a local zone of neuronal cell death and neurofilament loss (~100 – 200 µm radius) making it difficult to acquire signal (Biran et al. 2005). Coupled with the reactive response is the persistence of leaky vasculature. An implanted neural probe continually disrupts local vasculature due to micromotion and mechanical strain (Kozai, Vazquez, et al. 2012; Muthuswamy et al. 2003) leading to the constant release of inflammatory agents (Karumbaiah et al. 2013; Saxena et al. 2013; Szarowski et al. 2003; Biran et al. 2005; McConnell et al. 2009; Winslow & Tresco 2010; Kozai, Li, et al. 2014; Kozai, Gugel, et al. 2014) that perpetuates the local reactive response (Kozai, Jaquins-Gerstl, et al. 2015). Thus, an MEA with a pitch of less than 400 µm would begin to suffer from overlapping

regions of glial scarring, neuronal death, and leaky vasculature, ultimately leading to degraded probe performance in a continuous scarred region.

The overall shortcomings of traditional MEAs have led to many groups exploring various design modifications. Some have tried to develop electrodes with a low Young's modulus by building the electrodes from soft nanocomposites (Harris, Capadona, et al. 2011; Harris, Hess, et al. 2011), shape memory polymers (Ware et al. 2012), parylene-c (Kim et al. 2013; Takeuchi et al. 2005), polyimide (Rousche et al. 2001), or polydimethyl siloxane (McClain et al. 2011; Kozai & Kipke 2009). These materials have a Young's modulus that is closer to that of the brain; however, these new probes introduce new challenges due to bending, buckling, and deflecting of the probe during insertion. In addition, these polymer probes use thin-film metal traces which are brittle and geometries that are more susceptible to cracking during fabrication, assembly, and insertion (Ware et al. 2014; Kozai, Catt, et al. 2015). To compensate for the softness of the probe and fragility of the traces, these softer probes often reinforce their structures by using larger dimensions, which can lead to greater tissue damage and also greatly diminishes their ability to be used in a high density electrode array.

Another approach has been the development of ultrasmall probes. Skousen and colleagues showed that a lattice style electrode, with its greatly reduced surface area, had significantly improved normalized neuronal density (~90%) within a 50 μm radius, compared to a solid device (~40%) with the same footprint (Skousen et al. 2011). This type of electrode design demonstrates the ability to minimize the scarring response of the brain which in turn would allow MEAs to have pitches much smaller than 400 μm. Many current designs require the use of a shuttle (Kozai & Kipke 2009; Gilgunn et al.

2012) or lattice style backbone (Seymour & Kipke 2007; Skousen et al. 2011) that can make implantation difficult and possibly lead to a larger damage radius. In addition, many of these smaller devices cannot reach deeper structures in the brain, can be extremely brittle, and are difficult to achieve in high channel counts across large cortical areas compared to state-of-the-art MEAs, such as the Utah Array.

Ideally an MEA would be made from a soft material that can be manufactured with ultrasmall dimensions with sufficient strength and durability, and have high channel counts. Unfortunately, such a device does not currently exist due to the physical limitations and tradeoffs between size and strength. This work takes a different approach by utilizing stiff carbon fiber electrodes, which typically have radii on the order of 6 – 7 μm and a Young's modulus of 241 GPa (MatWeb 2012), as compared to silicon's 165 GPa (Dolbow & Gosz 1996). Some of the earliest carbon fibers electrodes were insulated in a pulled glass capillary tube, which was then back filled with an electrolyte (Armstrong-James & Millar 1979). Once insulated, this electrode can be used as is for acute electrophysiology recordings (Armstrong-James & Millar 1979). Coupled with voltammetry methods the same carbon fiber electrodes can be used to detect dopamine, or other oxidisable neurotransmitters (Budai 2010), in both animals (Ponchon et al. 1979; Rebec et al. 1997; Park et al. 2011) and slice work (Heien et al. 2004; Ferris et al. 2013). These applications are feasible due to the low electrical resistivity of carbon fibers. This leads to less thermal noise and enables the fibers to detect small signals without noise contamination (Budai 2010). These characteristics have led other groups to develop and chronically implant bundled carbon fibers electrodes that form a 4 x 4 tetrode-like bundle, with an overall cross-sectional width of 26 μm (Guitchounts et al. 2013).

Unfortunately, none of the previously described implementations of carbon fiber electrodes take advantage of all of the unique properties inherent to an individual fiber. The naturally small cross-sectional footprint of individual carbon fibers leads to less scarring and the high Young's modulus makes insertion easier (Kozai, Langhals, et al. 2012). The high Young's modulus would seem to contradict previous findings; however, the combined metrics of the small footprint and Young's modulus give these probes one of the smallest overall stiffness factors among implantable electrodes which is well documented by Kozai et al. (Kozai, Langhals, et al. 2012). Instead of the traditional means of insulating the carbon fibers with a glass capillary, which is brittle and can easily break, the devices are insulated with parylene-c, an FDA compliant material (Hsu et al. 2009). This allows the fibers to retain their flexibility or low stiffness while also maintaining their small size.

This aim evaluates methods to successfully insert high density carbon fiber arrays with site distances of approximately 150 μm, which is the smallest recorded electrode pitch for an MEA used in a successful chronic recording. Initially, the carbon fiber spacing negated the ability to insert each fiber individually without causing damage to neighboring sites. This problem was solved with the encapsulation of fibers in a temporary poly(ethylene glycol) (PEG) coating. While the PEG encapsulation step was sufficient for the insertion of arrays with only one or two rows of fibers, it was difficult to extend this method to arrays with three or more rows of fibers, which would allow for greater neuronal sampling within a given cortical area. Hence, a second approach using a stackable silicon support structure was developed, utilizing design cues from the PEG coated arrays, to enable the fabrication and insertion of arrays with three or more rows.

With this new method, single and triple layer devices were fabricated, successfully inserted, and able to record single unit activity in acute surgical preparations.

2.3 Materials & Methods

2.3.1 Carbon Fiber Array Fabrication and Characterization

2.3.1.1 Array Assembly

Custom printed circuit boards (PCBs), designed to fit Tucker-Davis Technologies ZIF headstages, were manufactured by SpeedyCircuits (Huntington Beach, CA) and designed to create a high density array of carbon fibers with a specified site pitch of 0.003 ” or 152.4 µm. The boards contained two vias, one for a reference wire and one for a ground wire, and 16 separate exposed traces at the bottom of the PCB for the carbon fibers. The vias and traces were connected to a set of bond pads on one side of the PCB, while the other side of the PCB had another set of bond pads with no connections. A Hirose connecter (DF30FC-20DS-0.4V, Hirose, Simi Valley, CA) was soldered to each side of the PCB’s bond pads and a shroud placed over the top to conform to ZIF headstages (Tucker-Davis Technologies, Alachua, FL) (figure 2.1(a)). Exposed gold coated traces at the tip of the PCB (figure 2.1(b)) were then individually coated with a conductive silver epoxy (H20E, Epoxy Technology, Billerica, MA) (figure 2.1(c)) using the tip of a pulled glass capillary. A carbon fiber bundle (T-650/35 3K, Cytec Thornel, Woodland Park, NJ) was then separated into individual fibers (d=6.8 µm according to manufacturer specifications (MatWeb 2012)), which were then cut down to lengths of approximately 6 – 7 mm. A single uninsulated fiber piece was placed on each of the silver epoxy coated traces, by hand, under a microscope (figure 2.1(d)). This process of

coating with silver epoxy and placement of the fibers, took approximately 10 minutes for eight traces. The entire assembly was then placed in an oven to heat cure the conductive silver epoxy at 140 °C for 20 minutes. These settings are higher than the manufacturers recommended times, as the original specifications, 140 °C for 8 minutes, were found to be insufficient for fully curing the small amount of epoxy used. This same process was then repeated on the other side of the PCB. A small amount of insulating epoxy (353NDT, Epoxy Technology, Billerica, MA) was used to protect the trace and carbon fiber contacts (figure 2.1(e)). A different bake setting (~120 °C for 20 minutes) was used for the insulating epoxy, as the original specifications, 120 °C for 5 minutes, were found to be insufficient for fully curing the small amount of epoxy used. Fibers were cut to desired lengths (figure 2.1(f)) using a set of surgical scissors (15003-08, Fine Science Tools, Foster City, CA) and a stereoscope equipped with a reticle.

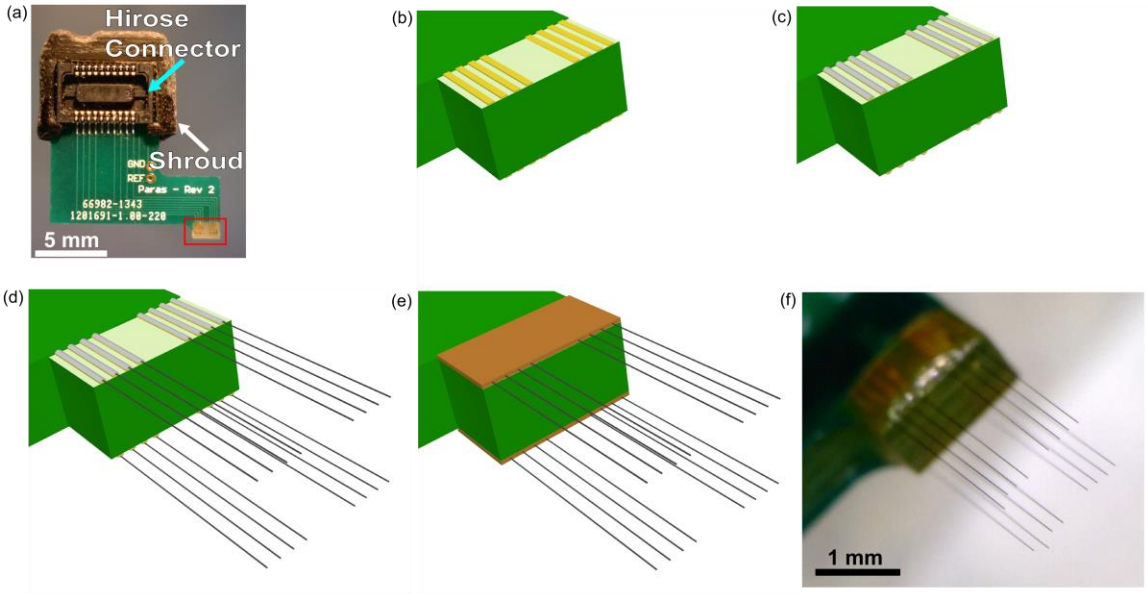

Figure 2.1. Step-by-step assembly of a carbon fiber array. (a) Bare PCB with attached Hirose connector (light blue arrow) and shroud (white arrow). Exposed gold traces highlighted in red box undergo different processing steps which are illustrated in the drawings of (b)-(e). (b) Close up drawing of exposed gold traces from bare PCB. (c) Each trace is coated with a thin layer of silver epoxy using a pulled glass capillary pipette. Silver epoxy that bridged two traces was removed by wiping the whole board with 70% ethanol. (d) Using forceps, a single carbon fiber was placed within each trace. (e) Epoxy is placed on top of

the exposed contacts to insulate and protect them from damage. (f) An image of the final product with fibers cut to their desired length.

To ensure that the initially specified site pitch was well maintained after the placement of each fiber, 6 arrays were imaged with varying numbers of fibers. Using ImageJ 1.48v (http://imagej.nih.gov/ij/) the distance between neighboring fibers was measured. The pitch between fibers was found to be 153.7 ± 1 μm (mean ± standard error of the mean, n=50 distances measured) which was acceptable given the initial design specification of a 152.4 μm pitch.

2.3.1.2 Parylene-c Coating and PEDOT:pTS Electrodeposition

Once fully assembled all carbon fiber arrays used in insertion tests and for neural recordings were coated with an 800 nm thick insulating layer of parylene-c (Kozai, Langhals, et al. 2012) using a Parylene Deposition System 2010 (SCS Coatings, Indianapolis, IN). For those arrays used to record neural activity the tip of each electrode was cut to expose a small bare carbon fiber site. To lower the exposed carbon fiber's site impedance a solution of 0.01 M 3,4-ethylenedioxythiophene (483028, Sigma-Aldrich, St. Louis, MO) and 0.1 M sodium p-toluenesulfonate (152536, Sigma-Aldrich, St. Louis, MO) was electrodeposited by applying 100 pA/channel for 600 seconds to form a layer of poly(3,4-ethylenedioxythiophene):sodium p-toluenesulfonate (PEDOT:pTS) (Green et al. 2012). All active channels were shorted together during the electrodeposition step and the total current delivered was scaled accordingly.

2.3.1.3 Electrochemical Impedance Spectroscopy (EIS) and Cyclic Voltammetry (CV)

To verify all deposition and coatings steps, EIS and CV measurements were taken with a PGSTAT12 Autolab (EcoChemie, Utrecht, Netherlands), controlled by vendor supplied NOVA software. For all measurements, probes were first submerged by 1 mm in a 1x phosphate buffered saline (PBS) solution (BP3994, Fisher, Waltham, MA). A stainless steel rod was used as the counter electrode and an Ag|AgCl electrode (RE-5B, BASi, West Lafayette, IN) served as the reference electrode. EIS measurements were obtained by applying a 10 mV_{RMS} signal from 10 Hz to 31 kHz. CV measurements were obtained by sweeping between 0.8 V to -0.6 V to 0.8 V, a total of three times, at a scan rate of 1 V/s. Custom Matlab (Mathworks, Natick, MA) scripts were used to determine both the charge storage capacity (CSC) by integrating the area under the CV curves and frequency specific impedance values.

2.3.1.4 Accelerated Soak Test Setup

Boards with parylene-c and PEDOT:pTS coated carbon fibers had the fiber only portion submerged in 1x PBS maintained at 60 °C. At each time point the fibers were removed from the heated 1x PBS and rinsed with deionized water. Next the impedance of the fibers at 1 kHz was recorded. Once recordings were complete the assembly was returned to the heated 1x PBS.

According to works by Green et al. (Green et al. 2012) & Hukins et al. (Hukins et al. 2008), equation (2.1) can be used to determine simulated aging time that the fibers have undergone:

$$t_{37} = t_T \times Q10^{(T-37)/10} \quad (2.1)$$

Where t_{37} is the simulated aging time at 37 °C, t_T is the amount of real time that the samples have been kept at the elevated temperature, T, and Q10 is an aging factor that is equal to 2, according to ATSM guidelines for polymer aging (ATSM 2011). Calculating the simulated time for t_T = 1 and T = 60 °C, results in t_{37} = 4.92. This value of 4.92 is the acceleration factor and all real time measurements are scaled by this amount to obtain the simulated time.

2.3.2 PEG Facilitated Array Insertion

2.3.2.1 Application of PEG Coating

The first method developed to insert carbon fibers arrays, with sufficient length to reach cortical depths, used 2050 MW PEG (295906, Sigma Aldrich, St. Louis, MO), a non-toxic material that temporarily stiffened the fibers but could be removed with the application of sterile room temperature saline or Lactated Ringer's (2B2324, Baxter, Deerfield, IL), via a syringe, over the course of 15 - 20 minutes. Carbon fiber arrays were first mounted to a micromanipulator and positioned such that the two rows of fibers were parallel to the benchtop's surface. Next, with the aid of a stereoscope, a razor blade covered in aluminum foil was inserted in between the two rows of fibers. The aluminum foil was lightly coated with sterile mineral oil (M5310, Sigma Aldrich, St. Louis, MO) and all excess oil was removed. The array was then moved such that the top row of fibers (those visible from a top-down view) were gently resting on top of the oiled aluminum surface. Once the fibers were in position, a coil of wire was wrapped around a soldering iron at 350 °F with a portion of the wire left to protrude from the tip. The tip of the wire was then used to pick up a single flake of 2050 PEG. The PEG was then allowed to fully melt at the tip of the wire. Once fully melted the liquid PEG was applied

to the fibers resting on the oiled aluminum surface (figure 2.2(a)). After cooling, the PEG easily released from the oiled surface and the array was retracted. Once clear of the razor blade, the array was turned over and the same operation was performed on the bottom row of fibers.

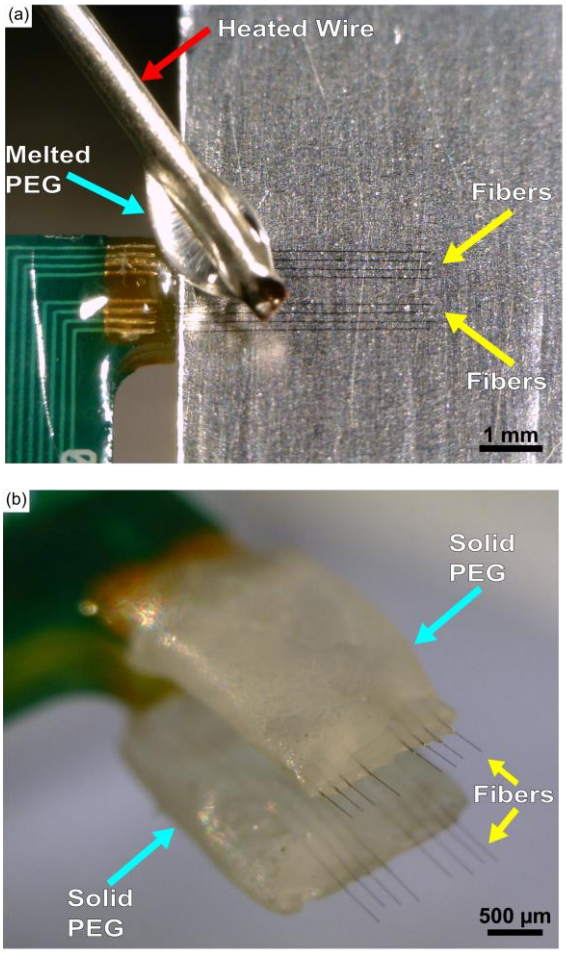

Figure 2.2. PEG coating method. (a) Application of melted 2050 PEG (light blue arrow) using a heated wire (red arrow) while the fibers (yellow arrows) rest on a lightly oiled aluminum surface. (b) Carbon fiber array coated with solidified PEG (light blue arrows) on both sides with submillimeter exposure of the fibers (yellow arrows).

2.3.2.2 Surgery for Chronic Implantation of PEG Coated Carbon Fibers

Chronic implantation of carbon fiber arrays used adult male Long Evans rats (n=5) weighing 300 – 350 g. Rats were first anesthetized using 5% isoflurane (v/v) for induction and then 1 – 3% isoflurane (v/v) to maintain anesthesia. The head was then

shaved at and around the area of the incision site. The shaved area was triple swabbed using alternating applications of betadine and 70% ethanol. Ointment was applied to the eyes to keep them from drying during surgery. Once mounted in the ear bars of the stereotax, the shaved area was swabbed one more time with betadine followed by 70% ethanol. A subcutaneous injection of lidocaine (4 mg/mL) was given at the proposed site of incision at a maximum dosage of 4 mg lidocaine per 1 kg of body weight. After incision, the skin flaps were pulled away using hemostats and the skull surface cleaned using a combination of cotton swabs and 2% hydrogen peroxide (v/v). A burr bit (19008-07, Fine Science Tools, Foster City, CA) was used to drill seven holes around the periphery of the skull for seven bone screws (19010-00, Fine Science Tools, Foster City, CA). Next, a 2 mm x 3 mm craniotomy was made over the right hemisphere's motor cortex using coordinates from a reference atlas (Paxinos & Watson 2007). Before resecting the dura, a layer of Kwik-Sil (World Precision Instruments, Sarasota, FL) was applied to the skull at the medial and anterior sides of the craniotomy.

Following the resection of the dura, the PEG coated carbon fiber array was brought to the surface of the brain. The exposed fibers were driven into the brain manually using the stereotactic manipulator and depth was monitored using a digital readout. The insertion of the exposed fibers took approximately 5 – 10 seconds. Once the PEG coated portion of the fibers reached the brain's surface, manual insertion was halted. Using a syringe filled with room temperature sterile Lactated Ringer's, a small portion of the PEG nearest to the brain was dissolved away while a surgical spear soaked up the PEG/Ringer's solution. The fibers were then manually driven in further, again taking 5 – 10 seconds for insertion, and more PEG dissolved away until the final target

depth was reached. All of the remaining PEG was dissolved away using additional Ringer's. Additional Kwik-Sil was then applied to the skull at the lateral and posterior sides of the craniotomy forming a barrier around the craniotomy. Once the Kwik-Sil had completely cured, the craniotomy, exposed fibers, and surrounding Kwik-Sil barrier were flooded with either Kwik-Cast (World Precision Instruments, Sarasota, FL) or alginate (Nunamaker & Kipke 2010). Kwik-Cast was used directly inside the craniotomy over the Kwik-Sil due to its lower viscosity which allows it to better conform to the fibers and any irregularities within the craniotomy itself. Reference and ground wires originating from the array's PCB were attached to the posterior most bone screw. The PCB was then anchored to all of the skull's bone screws using dental acrylic. The skin flaps were brought up over the dental acrylic headcap on each side and sutured together at the anterior and posterior ends. Triple antibiotic ointment was liberally applied around the headcap. Animals were then removed from the stereotax and allowed to recover on a heated pad placed under their cage. During surgery, animal vitals were monitored using a pulse-oximeter and rectal temperature probe. All procedures and post-operative care complied with the University of Michigan's University Committee on Use and Care of Animals.

2.3.2.3 Electrophysiology Recordings and Spike Sorting

Electrophysiology recordings of spontaneous activity using chronic implants of carbon fiber arrays were done while the rats were awake. Recordings done with acute implants of silicon support structures, as discussed below, took place while the rats were under ketamine/xylazine anesthesia. All acquisition of electrophysiology recordings were taken using a ZC16 headstage, RA16PA pre-amplifier, and RX5 Pentusa base

station (Tucker-Davis Technologies, Alachua, FL). During data acquisition, the pre-amplifier high pass filtered at 2.2 Hz, anti-aliased filtered at 7.5 kHz, and sampled at a rate of ~25 kHz. Each data acquisition session lasted 5 or 10 minutes.

Recording sessions were imported into Offline Sorter (Plexon, Dallas, TX) and first high-pass filtered (250 Hz corner, 4^{th} order Butterworth). Each channel was manually thresholded and the resultant waveforms sorted by a trained operator.

2.3.3 Silicon Support Structure Facilitated Insertion

2.3.3.1 Silicon Support Structure Fabrication

The second method to insert carbon fiber arrays involved the use of a cleanroom fabricated silicon support structure. The process started with the formation of a trench that eventually served as a guide for the placement and securement of each carbon fiber. A 10 µm wide and 10 µm deep trench was formed by silicon deep reactive-ion etching (DRIE) with patterned photoresist as an etch mask (figure 2.3(a)). After thorough organic/ionic cleaning, the silicon wafer was highly doped ($>10^{19}$ cm^{-3}) up to ~12 µm in depth by deep boron doping and diffusion (figure 2.3(b)), which is similar to the methods and dimensions seen in other silicon electrode technologies (Bai et al. 2000; Wise et al. 2004; Vetter et al. 2004). The highly doped region was utilized as an etch stop layer of the final ethylene diamine and pyrocatechol (EDP) silicon etch. A dome-shaped cross section of the eventual individual shanks was achieved by the doping of the exposed trenches. The thickness of doped silicon below the trench was also ~12 µm (figure 2.3(b)) which allowed for sufficient mechanical stiffness during insertion. The shape of the shank tips and backend of the silicon guide structure were defined by another lithography and silicon DRIE step, again using photoresist as an etch mask. The final step

was the release of structures using an EDP etch step that very selectively etched the undoped silicon over the highly doped silicon (figure 2.3(c)).

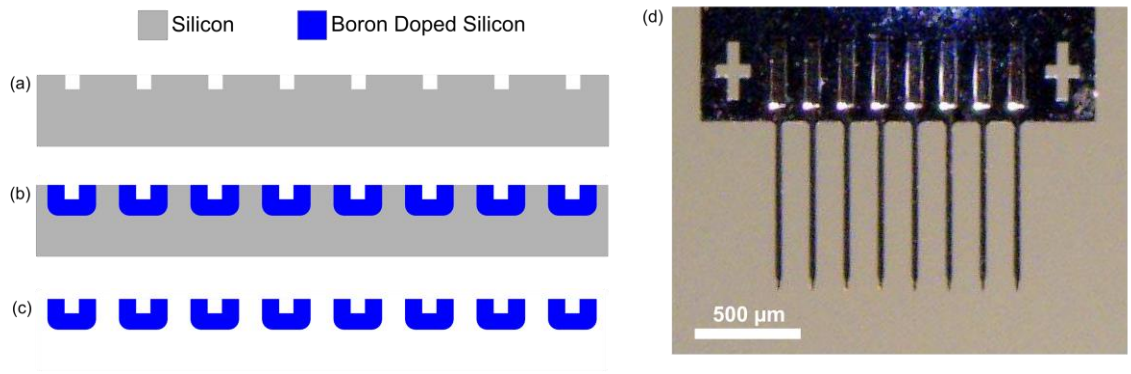

Figure 2.3. Microfabrication steps of silicon support structures. (a) DRIE etch of silicon to form trenches. (b) Boron doping to define overall structure of the device. (c) EDP etch step to selectively etch silicon and release the structures. (d) Final silicon support structure without carbon fibers.

2.3.3.2 Surgery for Acute Testing of Functional Silicon Support Structure

Acute implantation of silicon support structures with functionalized carbon fibers used adult male Long Evans rats (n=3) weighing 300 – 350 g. Rats were first anesthetized using 5% isoflurane (v/v) to induce and then maintained under anesthesia with an intraperitoneal (IP) injection of ketamine (50 mg/mL) / xylazine (5 mg/mL) at a maximum dosage of 0.125 mL per 100 g of body weight. Regular IP injections of ketamine (50 mg/mL) were given. The same procedures from section 2.3.2.2 were then used to prepare the surgical site. Reference and ground wires originating from the probe's PCB were attached to a single bone screw.

Following the resection of the dura, the probe was inserted into the brain to the desired depth by monitoring a digital readout. Electrophysiology recordings were taken and the animal was sacrificed at the end of the experiment. During surgery, animal vitals were monitored using a pulse-oximeter and rectal temperature probe. All procedures and

post-operative care complied with the University of Michigan's University Committee on Use and Care of Animals.

2.3.4 SEM Imaging

A FEI Nova 200 Nanolab Focused Ion Beam Workstation and Scanning Electron Microscope (FEI, Hillsboro, OR) was used for SEM imaging. Prior to imaging, samples were gold sputter coated with a SPI-Module Sputter Coater (SPI Supplies, West Chester, PA).

2.3.5 Statistical Analysis

A one-sided t-test was used to determine if the dimpling of the brain for the pointed silicon shanks was significantly less than that of the blunt silicon shanks.

ANOVA was used to ascertain if there existed any difference in the alignment of fibers using the two fabrication methods and varying silicon shank lengths. This was followed by grouped pairwise t-tests with a Bonferroni correction to determine specific group differences. All calculations were carried out using R 3.0.2 (http://www.r-project.org/).

2.4 Results

2.4.1 Carbon Fiber Array Characterization

2.4.1.1 Carbon Fiber Length vs. Insertion Success

Previous work demonstrated the ability to implant individual carbon fibers, often with the aid of forceps (Kozai, Langhals, et al. 2012). The 153.7 ± 1 μm (mean ± standard error of the mean, n=50 distances measured) pitch of the new carbon fiber arrays

made this previous method impractical during surgery. To alleviate this problem, fibers were continually shortened. It was noted that more fibers would self-insert at shorter lengths. To determine the optimal probe length for reliable insertion, below which isolated fibers would self-insert, one array with 14 parylene-c coated fibers was inserted 5 times (n=70 fibers), for various lengths, into a perfused (PBS only) rat brain (figure 2.4). Lengths of 1 mm or greater were found to insert with a <80% success rate. Lengths of 500 µm were found to insert with 100% success. These tests were also carried out in a 0.6% (w/v) agarose brain phantom (Chen et al. 2004) (figure 2.4) using one 16 fiber array once per length and one 15 fiber array 5 times per length (n=91 fibers). It was observed during *ex vivo* tests that the longer fibers did not achieve the same success rates as equal length fibers used in the agarose test. This is partially attributable to the natural curvature of the brain, which caused the fibers to deflect, and that the agarose phantom is a proxy for the brain and not an exact substitute.

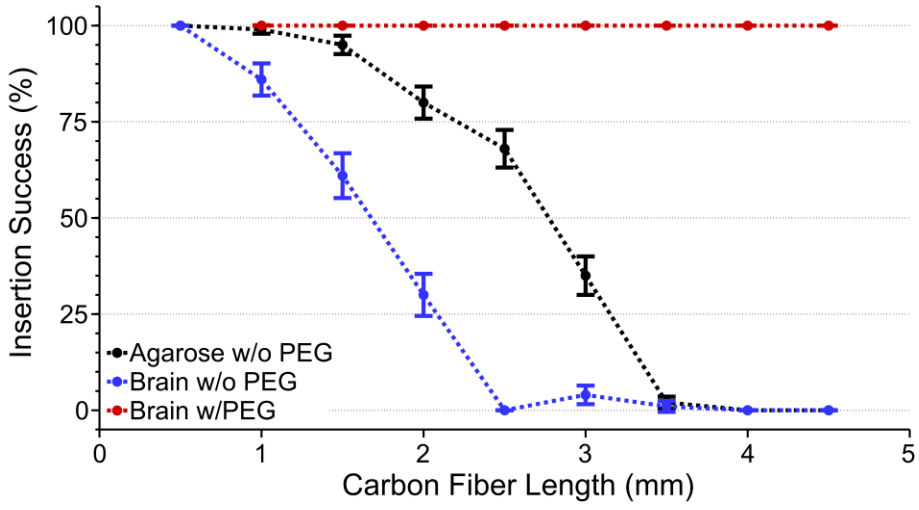

Figure 2.4. Carbon fiber insertion tests. Carbon fiber insertion tests. Insertion success rate (mean ± standard error of the mean) of carbon fiber arrays in agarose without PEG (black, n=91 fibers), an explanted rat brain without PEG (blue, n=70 fibers), and an explanted rat brain with PEG coating (red, n=22 fibers). PEG coating enabled a 100% insertion success rate regardless of length or insertion medium, whereas non-PEG coated arrays suffered from a low success rate at lengths longer than 2 mm.

The results from figure 2.4 were also verified in surgery using non-functional parylene-c coated carbon fiber arrays. As expected, the longest fibers (4 – 5 mm in length) would not insert and any attempt at manipulation with forceps led to many fibers breaking off of the PCB. Attempts to insert the shortest fibers were successful as the very tips were able to penetrate the brain, but they could not go any further as the PCB's back end started to touch the skull's surface before the fibers reached a depth of 500 µm. At these short lengths (500 µm) and with the current PCB design, reaching layer V/VI pyramidal neurons in the rat motor cortex, located 750 – 1750 µm below the cortical surface (Skoglund et al. 1997), would be impossible. Also, this target depth does not account for skull thickness (Li et al. 2006) and curvature, which necessitates the fibers to be even longer, making it more difficult for them to self-insert.

To reach relevant cortical depths, while taking into account factors such as skull curvature, a coating of 2050 PEG was used to temporarily encapsulate non-functional parylene-c coated fibers of various lengths, while leaving the lower ~500 µm exposed (figure 2.2(b)). PEG is a safe, biocompatible material, and poses no toxicity to neural tissue (Mahoney & Anseth 2006). Coating with PEG allowed for a 100% insertion success rate, using three separate arrays with 8, 8, and 6 parylene-c coated fibers one time for each length (n=22 fibers), in a perfused (PBS only) rat brain for fibers of various lengths (figure 2.4) as long as the exposed length was <1 mm. These results were replicated exactly when using a 0.6% (w/v) agarose phantom (data not shown).

2.4.1.2 Accelerated Soak Testing of Carbon Fibers

As a new formulation of PEDOT was used, when compared to previous work (Kozai, Langhals, et al. 2012), an accelerated soak test was carried out to determine if the

new formula could maintain a low impedance that would allow for chronic recordings over at least a one month time course. To test this, fibers were first mounted to printed circuit boards, coated with parylene-c, and then had the tips cut off to expose a bare carbon site. The exposed fiber tips were then coated in PEDOT:pTS. Finally, the fully functionalized carbon fibers (n=23 fibers from 3 arrays) were submerged in 1x PBS that was maintained at 60 °C.

Impedance measurements at multiple time points, including just prior to the PEDOT:pTS deposition, were taken to assess the viability of the PEDOT:pTS coating (figure 2.5). While the impedance at 1 kHz rose from 118 ± 28 kΩ (mean ± standard error of the mean) at simulated day 0, to 321 ± 56 kΩ (mean ± standard error of the mean) at simulated day 29.5, these values were found to be within an acceptable range for detecting unit activity, one month post implant, when compared to similarly sized electrodes (Guitchounts et al. 2013). In addition, subsequent chronic implants also verified the ability of implanted functionalized fibers to record single unit action potentials, one month post implant.

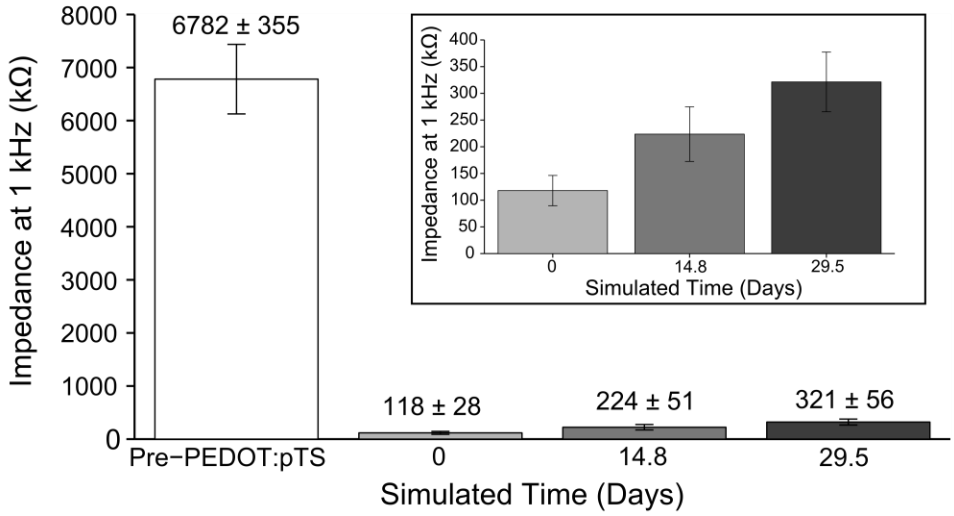

Figure 2.5. Carbon fiber soak test. 1 kHz impedance values (mean ± standard error of the mean) of functionalized carbon fibers undergoing an accelerated soak test. The pre-PEDOT:pTS impedance value of the fibers with exposed carbon tips (n=23 fibers) was 6782 ± 355 kΩ. This impedance decreased to 118 ± 28 kΩ, post-PEDOT:pTS deposition at day 0. From day 0 to simulated day 14.8, impedance increased by roughly 100 kΩ, with a similar increase from simulated day 14.8 to 29.5. The inset shows a magnified plot of the 1 kHz impedances measurements (mean ± standard error of the mean) taken at the three time points post-PEDOT:pTS deposition.

2.4.2 Surgical Implantation of PEG Coated Carbon Fibers

After verifying the ability of PEG coated carbon fibers to self-insert and of PEDOT:pTS coated fibers to maintain their low impedance at 1 kHz, chronic *in vivo* surgeries were carried out using carbon fiber arrays with fibers that were approximately 4 – 5 mm in length. During surgery the short exposed ends (~500 µm) of the PEG coated carbon fibers had no difficulty penetrating the brain. Step-by-step drawings and images illustrating the insertion of PEG coated arrays during surgery, along with removal of the PEG can be seen in figure 2.6.

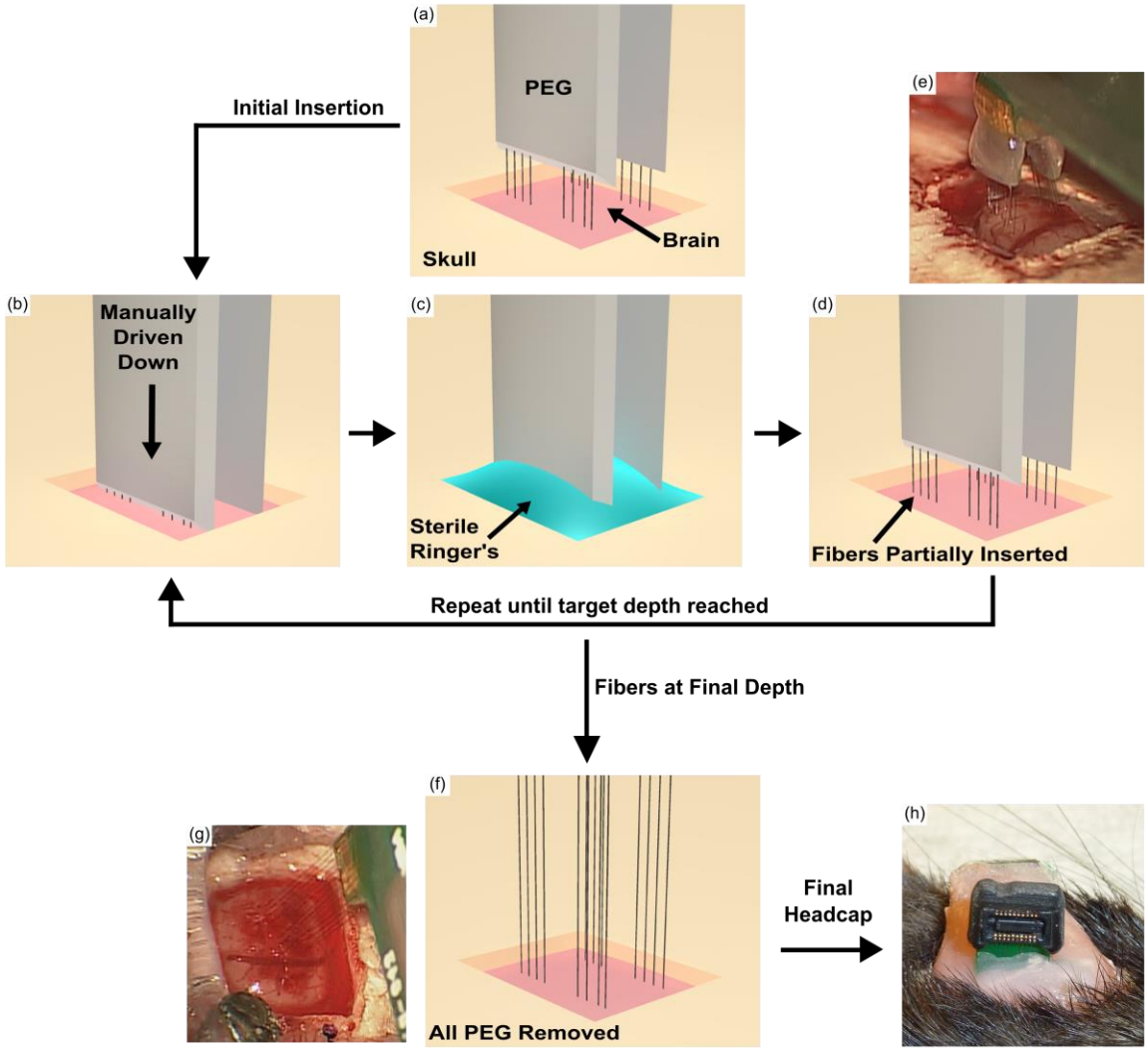

Figure 2.6. Insertion process of PEG coated carbon fiber arrays. (a) The PEG coated array is lowered till the fibers tips are just above the brain. (b) The array is driven down manually over the course of 5 – 10 seconds and stopped just before the PEG touches the brain's surface. (c) The craniotomy is filled with room temperature sterile Lactated Ringer's using a syringe. Any PEG that comes in to contact with the Ringer's will start to dissolve. As the Ringer's becomes saturated with PEG, a surgical spear is used to absorb the solution and the process is repeated until an additional 500 µm – 1 mm of fiber has been exposed. (d) The carbon fiber array is partially inserted into the brain and more of the fibers have been exposed with the selective removal of PEG from (c). The steps illustrated in (b)-(d) are repeated until the final target depth has been reached which takes approximately 15 - 20 minutes. (e) Surgical image of fibers that have been partially driven in and PEG that has been partially removed, similar to (d). (f) After reaching the target depth, the remaining PEG is exposed to Ringer's and is completely removed. (g) An image from surgery showing all fibers inserted into the brain at their final target depth and removal of all remaining PEG, similar to (f). (h) Accessible ZIF connection of a chronically implanted carbon fiber array. PCB was secured to the skull using dental acrylic.

This surgical method was used to chronically implant parylene-c and PEDOT:pTS coated carbon fiber arrays (n=60 fibers from 5 arrays) into five Long Evans rats. Each

processing step was confirmed with both EIS and CV measurements (figures 2.7(a) and 2.7(c)). EIS measurements are reported for 1 kHz (figure 2.7(b)), in addition to the calculated CSC (figure 2.7(d)) from the CV curves.

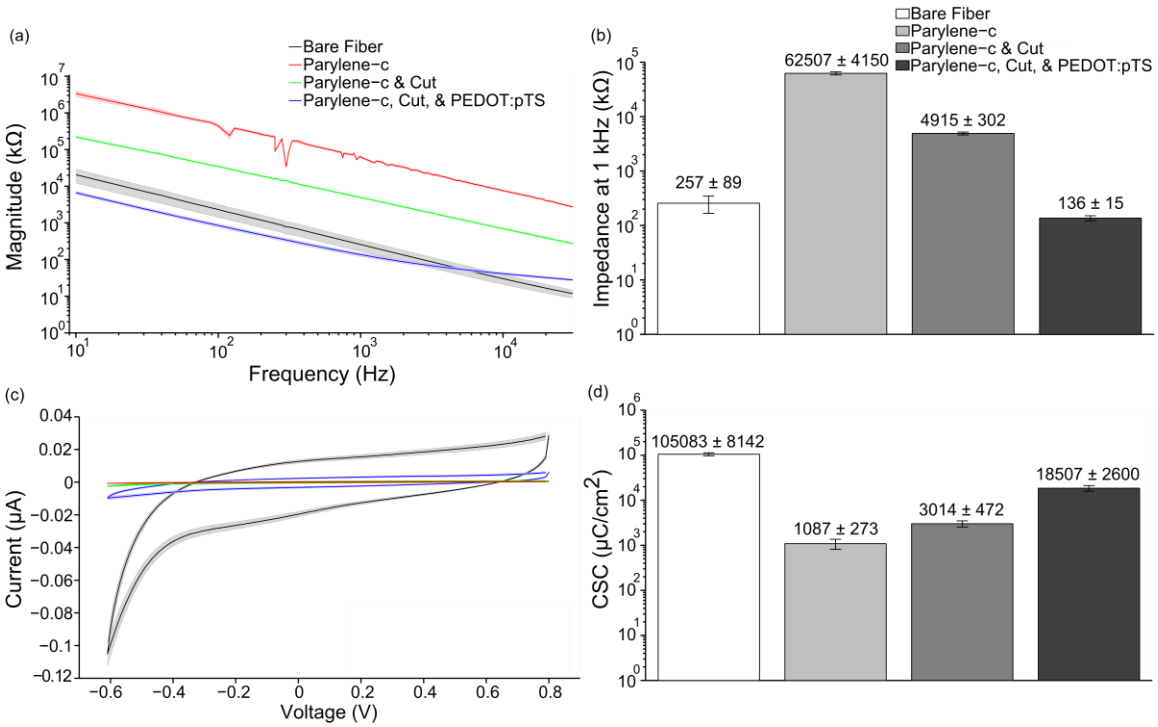

Figure 2.7. Carbon fiber functionalization steps. (a) Impedance magnitude values (mean ± standard error of the mean) were calculated across a range of frequencies at each functionalization step starting with bare fibers, parylene-c coating, exposing carbon fiber tips post parylene-c deposition, and electrochemical deposition of PEDOT:pTS (n=60 fibers from 5 arrays). (b) Impedance magnitude (mean ± standard error of the mean) at 1 kHz for each of the functionalization steps reported in (a). (c) CV plots (mean ± standard error of the mean) for each of the functionalization steps reported in (a). (d) CSC values (mean ± standard error of the mean) for each of the functionalization steps reported in (a).

All rats showed single unit activity. A diagram of each probe's implanted and non-implanted fibers are shown in figure 2.8(a) as blue and red circles, respectively. Representative sorted units and high-speed recordings, from days 1 and 31 post-implant, are shown in figures 2.8(b) and 2.8(c), respectively. Full sorted unit and high speed recording panels for every implanted electrode at days 1 and 31 can be seen in appendix figures A.1 – A.4.

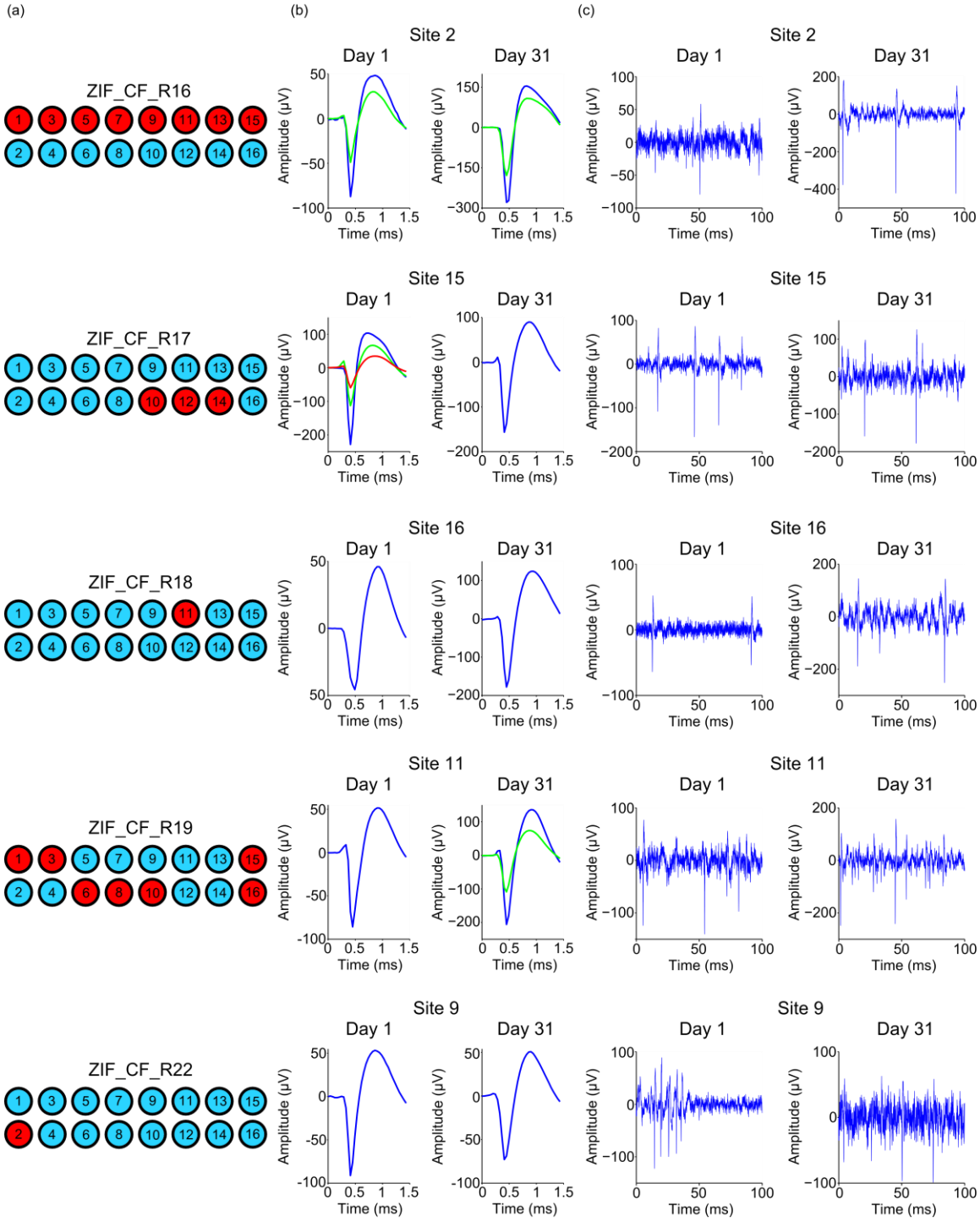

Figure 2.8. Chronically implanted carbon fiber arrays. (a) Schematic for each animal's implanted probe showing broken sites (red) and sites with a successfully implanted fiber (blue). (b) Average waveforms from a single site for each implant in (a) at days 1 and 31 post-implant. (c) Representative filtered (250 Hz corner, 4th order Butterworth, high-pass) high speed recordings, displaying sorted unit from (b).

The number of successfully implanted carbon fibers (n=60) is less than the theoretical number of 80 (one 16 channel array per animal) due to various factors. The first cause for missing fibers is that the arrays were partially damaged at some point during the fabrication process, starting from the initial placement of fibers to the final PEG coating. Second, during implantation, fibers would sometimes stick to one another and need to be separated using forceps or a surgical spear. During this delicate process an unintended movement could lead to a fiber breaking from the PCB. Third, fibers were purposefully removed if their intended path was obstructed by a major surface blood vessel. Lastly, the fibers were actually implanted but their sites were not coated with PEDOT:pTS or in the particular case of one electrode (ZIF_CF_R19, channel 6), day 1 post-operative impedance values and electrophysiology recordings indicated a broken channel. This last group was classified as broken channels as they exhibited the same impedance and recording qualities of those channels that were actually broken.

2.4.3 Silicon Support Structure Characterization

2.4.3.1 Array Design & Assembly

While the application of the PEG coating made insertion of carbon fiber arrays successful, it had some limitations. For carbon fiber arrays with two layers, a PEG coating, which can be difficult to apply at first, is readily achieved in most laboratories due to the minimal equipment needed; however, coating with PEG does not lend itself well to higher density arrays (i.e., more than two rows of fibers) using the application method described earlier. To generate higher density arrays a silicon support structure was fabricated that could be stacked with an interposer.

The silicon support structures were fabricated according to the steps outlined in figure 2.3. Once released from the wafer, the individual devices were mounted on printed circuit boards and a fiber was laid within the groove of each shank. At the end closest to the printed circuit board, the fibers were secured using a heat cured silver epoxy (H20E, Epoxy Technology, Billerica, MA). The portion of the fibers that lay in the grooves were secured using an insulating epoxy (301, Epoxy Technology, Billerica, MA) that was also heat cured. The individual silicon shanks had a pitch of 150 µm with a length of either 750 µm or 1000 µm. This fabrication method, while not significantly faster compared to the arrays using bare traces, has the important advantages of even carbon fiber spacing, stackability for high density arrays, and a design space that allows for the possibility of even closer shanks. The initial parameters of shank length and pitch were largely informed by the previous results of the PEG coated arrays. The pitch of the shanks was closely matched to that of the carbon arrays from previous experiments as it was known that at this close distance the fibers could self-insert. In addition, the two silicon shank lengths were chosen under the assumption that for the fibers to both self-insert and reach layer V/VI of rat motor cortex (Skoglund et al. 1997) they would need to extend approximately 500 µm beyond the shank ends.

Initial designs had the eight shanks either terminating in a blunt (figures 2.9(a) and 2.9(b)) or pointed end (figures 2.9(d) and 2.9(e)), both of which had a maximal width of ~30 µm. Initial experimental surgeries & insertion tests showed the blunt ended shanks causing a large amount of dimpling (figure 2.9(c)). When 6 blunt silicon shanks of 1000 µm length from one support structure were inserted to a depth of ~650 µm, brain dimpling was measured at 150.5 ± 16.9 µm (mean ± standard error of the mean, n=6).

This dimpling was not easily overcome; however, it was partially alleviated by removing every other shank. The tradeoff with this fix was the 50% reduction of carbon fiber density to a 300 µm pitch, which hinders the ability to create a high density device. The pointed shanks however, readily inserted into the brain (figure 2.9(f)). Performing a similar test as before, 6 pointed silicon shanks of 1000 µm length from one support structure were inserted to a depth of ~650 µm, which resulted in brain dimpling of 33.0 ± 4.7 µm (mean ± standard error of the mean, n=6). This dimpling was significantly less ($p<0.001$, one-sided t-test) than that of the blunt shanks and allowed us to maintain the 150 µm pitch needed for the high density arrays.

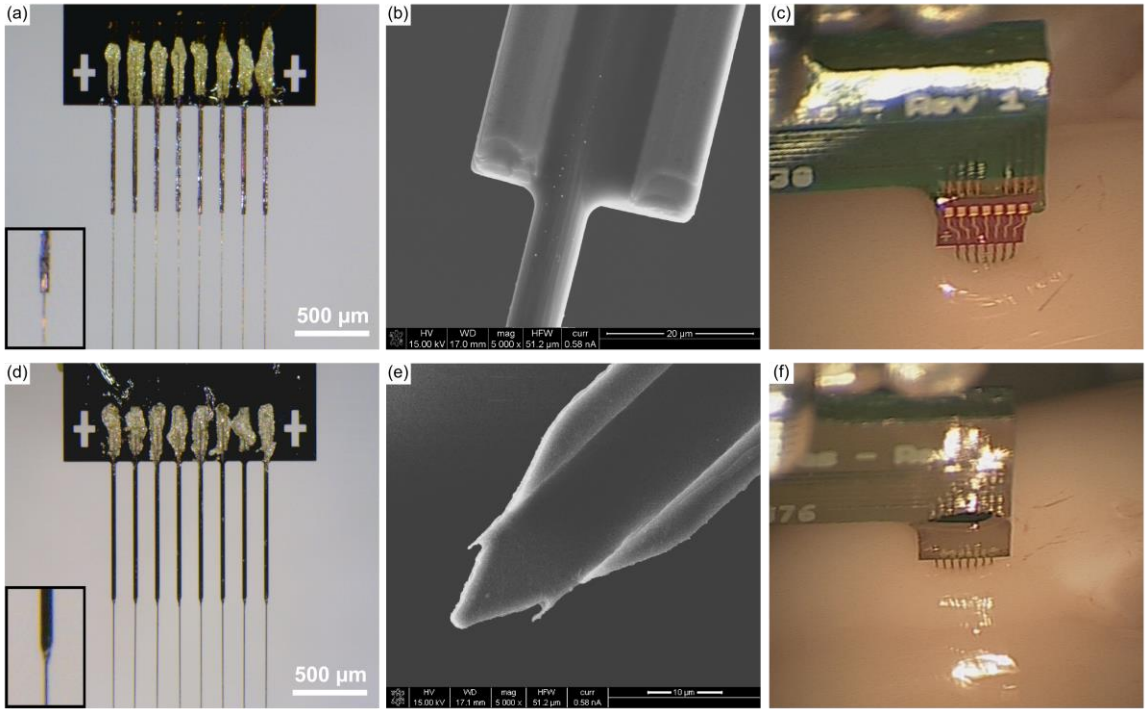

Figure 2.9. Silicon support structure designs. (a) & (b) Photo and SEM image of a silicon support structure with 750 µm long blunt shanks and carbon fibers secured within the shanks. Inset in (a) shows the termination point of a blunt silicon support shank with a carbon fiber protruding from the shank. (c) & (f) Insertion of blunt shank support structures resulted in a large amount of dimpling at the brain's surface (c) as compared to the pointed shank variant (f). (d) Photo of a silicon support structure with 1000 µm long pointed shanks and carbon fibers secured within the shanks. Inset shows the termination point of a pointed silicon support shank with a carbon fiber protruding from the shank. (e) SEM image of a silicon support structure with a pointed shank.

Another important aspect in designing the support shanks was ensuring that the fibers were as straight as possible, such that particular depths could be reached with reasonable certainty. Carbon fibers within shanks of length, 750 µm and 1000 µm, showed a misalignment of 0.208 ± 0.019° (mean ± standard error of the mean, n=69 fibers from 9 support structure arrays) and 0.157 ± 0.016° (mean ± standard error of the mean, n=71 fibers from 9 support structure arrays) respectively, using the edge of the silicon support structure's backend as a reference. When compared to devices with no shanks (0.311 ± 0.030°, mean ± standard error of the mean, n=76 fibers from 6 arrays), using the edge of the PCB backend as a reference, both shank lengths showed significantly improved alignment (figure 2.10). All subsequent insertion tests and experimental surgeries were carried out with the pointed silicon shanks.

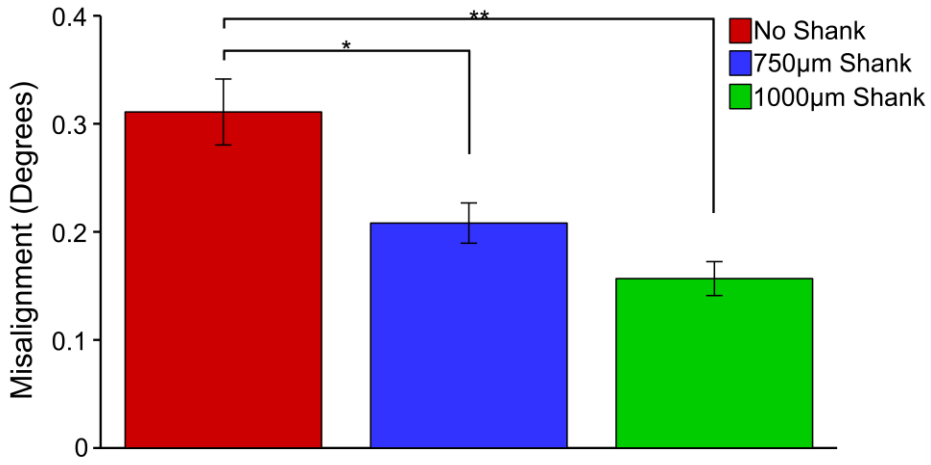

Figure 2.10. Carbon fiber alignment. Silicon shank devices show significantly less misalignment (pairwise t-test, Bonferroni correction) than devices fabricated without silicon support structures. * indicates significance at $p<0.01$, ** indicates significance at $p<0.001$.

2.4.3.2 Insertion Success

To ensure that the silicon support structures could serve as a viable replacement to the PEG coating, insertion tests with non-functional, parylene-c coated devices were

carried out in 0.6% (w/v) agarose and *ex vivo* using a perfused (PBS only) rat brain. For each test group a single 8 fiber+shank array (750 µm or 1000 µm length silicon shanks with 150 µm shank spacing) was inserted 5 times for each length of protruding fiber (n=40 fibers+shanks per test). As expected, fibers extending 1 mm or less beyond the silicon support shanks inserted into the agarose with nearly 100% success (figure 2.11) regardless of shank length. The insertion tests into the brain sample (figure 2.11) were not as successful as the agarose tests, however these metrics do line up well with the previous results seen in figure 2.4, where the overall insertion success was lower across all lengths except for that of 500 µm. This again demonstrates that 500 µm of exposed fiber is the critical length needed for fiber self-insertion.

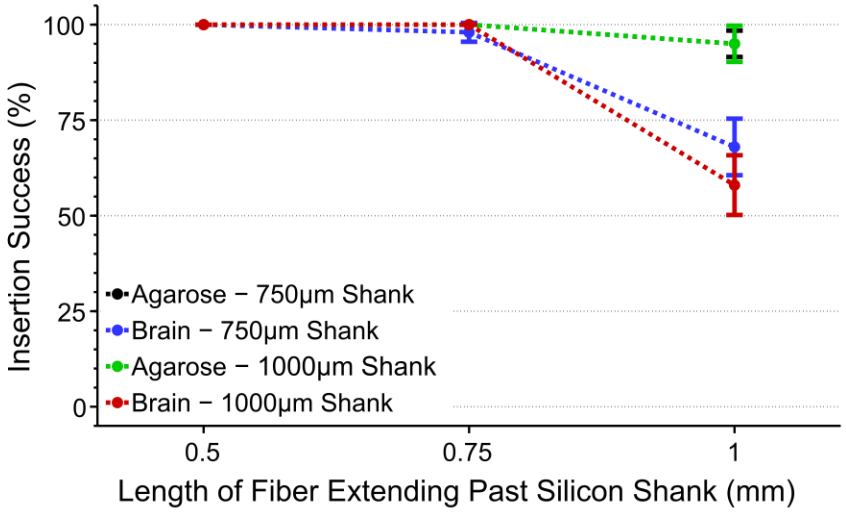

Figure 2.11. Silicon support structure and carbon fiber insertion tests. Insertion success rate (mean ± standard error of the mean) of silicon shanks with various length carbon fibers. Both 750 µm (black, n=40 fibers+shanks) and 1000 µm (green, n=40 fibers+shanks) shank lengths showed high insertion percentages in agarose regardless of fiber length. Tests in an explanted brain showed similar success for 750 µm (blue, n=40 fibers+shanks) and 1000 µm (red, n=40 fibers+shanks) shank lengths when fibers were ≤750 µm. All results, regardless of shank length or insertion medium, showed 100% success when fibers were 500 µm in length.

2.4.3.3 Functionalization & Acute *In Vivo* Testing

Given the high insertion success rate of the 1000 µm long silicon shanks (150 µm shank spacing) plus 500 µm of exposed carbon fibers, functional tests were carried out to validate this design's ability to record neuronal signals. As this first iteration of devices provided no electrical isolation, the entire silicon structure was first coated with an insulating layer of parylene-c once released from the water. Silicon structures were then secured to PCBs, and fibers laid within the individual shanks, secured by silver and insulating epoxy (301, Epoxy Technology, Billerica, MA). The entire assembled device was then coated with parylene-c (t=800 nm) to form an insulating layer around the fibers themselves and finally the tips of the fibers were functionalized with PEDOT:pTS. An electrical connection between the silver epoxy contact point of the carbon fibers and the PCBs exposed traces was made using pieces of small copper wire. Due to the inherent difficulties of placing a wire down for each carbon fiber, only every other shank received a carbon fiber (figure 2.12(a)). Each processing step was confirmed using both EIS and CV measurements (data not shown) that corresponded well to results shown in figure 2.6(a).

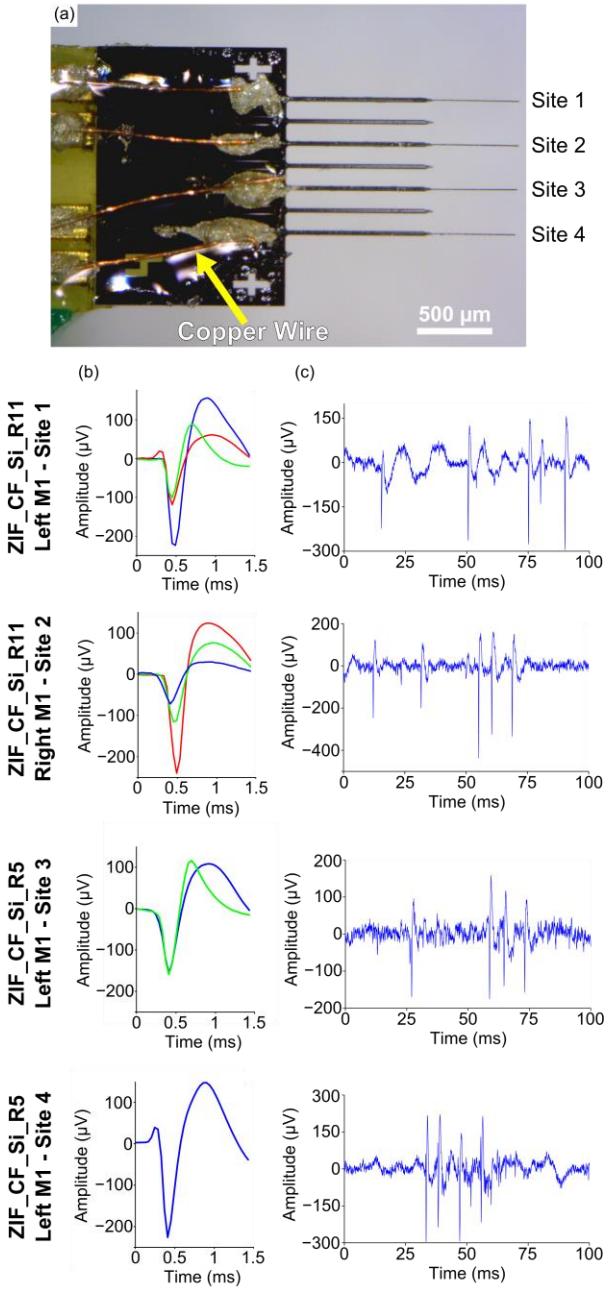

Figure 2.12. Acute testing of single layer silicon support structure. (a) Image of silicon support structure with carbon fibers. Copper wire (yellow arrow) connects each fiber to traces that leads to the backend headstage. (b) Representative waveforms detected on each site across the multiple implants. (c) Representative 100 ms snippet of filtered (250 Hz corner, 4th order Butterworth, high-pass) high speed recordings from each site.

To demonstrate feasibility of this new device, acute surgery on two Long Evans rats was performed under ketamine/xylazine anesthesia wherein the probes were

implanted in the M1 region at a depth of ~1.5 mm. In the first animal (ZIF_CF_Si_R5) a single probe, with four functionalized carbon fibers, was implanted in the left M1 region. In the second animal (ZIF_CF_Si_R11) two different probes, each with three functionalized carbon fibers, were implanted, one in each hemisphere with M1 as the target region. A total of sixteen distinct units were detected across nine of the ten functionalized channels using manual sorting (figures 2.12(b) and 2.12(c)). The average amplitude for all sixteen units was 245.9 ± 122.2 μV (mean ± SD). These results demonstrate the *in vivo* capability of the new silicon support structures to record high quality, single unit action potentials in a repeatable manner.

2.4.3.4 3D Support Structure – Functionalization & Acute *In Vivo* Testing

To fully validate the ability to insert the 3D design of the silicon supports, a stacked non-functional device was fabricated. Three silicon supports with 750 μm long shanks (150 μm shank spacing) and 500 μm of carbon fiber extending past the shanks were stacked with an interposer layer of glass (t=100 μm) (figure 2.13a). This device was successfully implanted 4 times during an acute surgery on a Longs Evans rat.

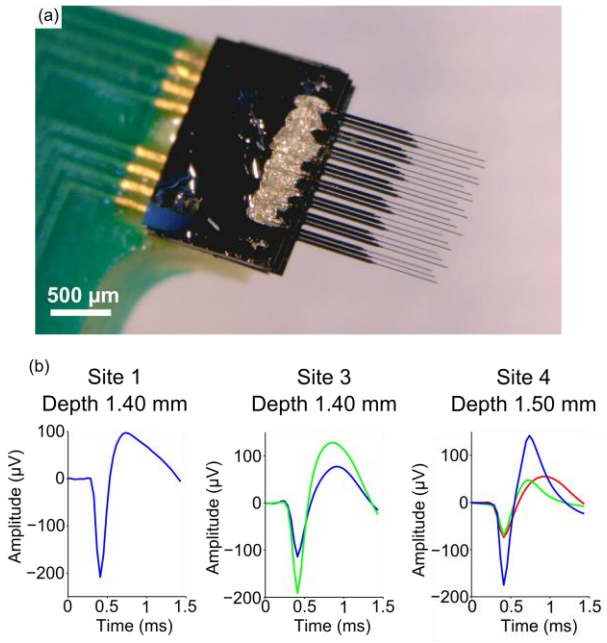

Figure 2.13. Acute testing of multi-layer silicon support structure. (a) Three stacked layers of silicon supports with carbon fibers forming a 3D device. (b) Average waveforms detected on multiple sites at various depths from a fully functionalized 3D device.

Finally, a fully functionalized device (not shown), similar to that in figure 2.12(a) was fabricated. In total, there were three silicon layers with a glass interposer (t=100 µm) between layers. For each silicon support, every other 1000 µm shank (150 µm shank spacing) received a carbon fiber. Due to the limitations of the PCB, only four of the twelve available recordings sites were electrically connected. During an acute procedure on one Long Evans rat under ketamine/xylazine anesthesia, recordings were taken with the functionalized device at multiple recordings depths in the M1 region. Single unit and multiunit action potentials were detected on multiple channels at various depths (figure 2.13(b)).

2.5 Discussion

2.5.1 *Ex Vivo* Characterization & Accelerated Soak Tests

This work first sought to characterize the potential ability of carbon fiber arrays to self-penetrate the brain and record chronic unit activity. Insertion dynamics and recording site stability were evaluated using *ex vivo* and accelerated soak tests, respectively. The *ex vivo* tests were carried out on PBS only perfused rat brains and showed that 500 µm long carbon fibers self-inserted with a 100% success rate. Accelerated soak tests demonstrated an increasing site impedance when aged to a simulated time of ~30 days, but remained low enough for the detection of single units.

While these tests were not designed to be exact substitutes for chronic *in vivo* implantation of the carbon fibers, they did serve as methods for rapid, high throughput characterization. Additionally, later *in vivo* studies confirmed the findings of these benchtop results.

2.5.2 PEG

Following the initial carbon fiber characterization using accelerated soak tests and PBS perfused rat brains, the ability to chronically implant individual arrays of 8.4 µm carbon fiber electrodes, with an electrode pitch of ~150 µm, was established. Self-insertion was achieved by taking advantage of the carbon fibers' high Young's modulus, which allowed them to penetrate the brain at exposed lengths of 500 µm. This unique property, along with a temporary PEG coating allowed us to reach cortical depths of ~1.5 mm without causing substantial insertion injury as evidenced by the detection of single unit action potentials in chronic implants. This penetration depth is sufficient for reaching hippocampus CA1 stratum pyramidale layers in mice, cortical layer VI in rats, and

cortical layer V in primates. With this preparation the use of an insertion shuttle, which can increase the insertion injury to the tissue immediately surrounding the electrode, was avoided. According to an exhaustive literature search, these carbon fiber arrays set a new record for electrode shank pitch when compared to the most commonly used chronically implanted functional MEAs (table 2.1). These higher density arrays can facilitate the study of horizontal cortical communications, such as lateral inhibition and adaptation, in neuroscience studies and BMI applications.

MEA Technology	Shank Pitch	Electrode Shank Size	Recording Site Diameter	Shank Length	Materials
Carbon Fibers	150 – 152.4 µm	8.4 µm diameter with insulation coating	7 µm	0.5 – 5 mm	Carbon Fiber + PEDOT:pTS
Blackrock Microsystems (Utah Array) (Nordhausen et al. 1996; Barrese et al. 2013; Normann et al. 1999; Negi et al. 2010)	400 µm	90 µm x 90 µm at base, 5 µm tip diameter	40 µm tapering to 5 µm	1 – 1.5 mm	Silicon + Platinum
Microprobes (Prasad et al. 2014)	400 µm	75 µm diameter	2 – 3 µm	1.5 mm	Platinum/ Iridium
Tucker-Davis Technologies (Sankar et al. 2014)	250 µm	50 µm diameter	50 µm	5 mm	Tungsten
NeuroNexus, Inc. (Riera et al. 2012)	400 µm	50 µm thickness x variable width	15 µm	1.4 mm (implant depth)	Silicon + Iridium

Table 2.1. MEA properties. Physical parameters of commercially available MEAs commonly used in research labs.

Though the PEG coating method has the ability to chronically implant up to 16 fibers, it is still limited to only two rows of fibers. Increasing the number of rows to three or more would greatly complicate the existing coating method. To address this challenge, the knowledge of carbon fiber insertion dynamics was used to design a platform that could support multiple rows of fibers, while also maintaining a comparable pitch.

2.5.3 Silicon Support Structure

This new platform, a stackable silicon support structure, was fabricated to improve the capabilities and channel count of future carbon fiber arrays. The blunt ended silicon structures that were originally developed were expected to readily penetrate the brain, given their small footprint of ~30 µm (w) x ~24 µm (h). However, upon testing, it was determined that a pitch of 150 µm led to a large amount of dimpling. The same style device with a tapered end, caused significantly less dimpling at the original 150 µm pitch. This highlights the clear tradeoff between a device's shape, no matter how small, and its pitch. This device was then tested with a single layer of carbon fibers and showed similar insertion success rate vs. length dynamics as the PEG coated arrays. Further tests using fully functionalized devices demonstrated the ability to record action potentials in an acute setting. Lastly, a 3D device consisting of multiple stacked silicon supports was constructed and was also shown to work *in vivo*. This new silicon platform will allow for a modular and highly customizable approach to building 3D arrays. Depending upon the application, shank pitch, length, and count can be varied within and between individual stacked layers.

2.6 Conclusion

With the ability for each site to record from a ~75 µm radius (Moffitt & McIntyre 2005), this array theoretically has the potential to record from all active neurons in a given cortical layer. With the current pitch of ~150 µm the detection of more localized neurons was expected. This discrepancy can be partially explained by the larger size and lower count of motor cortex neurons in layer V. In addition, during the sorting analysis using principle component space it was often noticed that large continuous clusters

contained neuronal units with varying amplitudes but no clear distinguishing cutoffs. Occasionally these clusters were separated into two or more units when the peak-to-peak amplitudes of the waveforms exceeded 100 μV between the smallest and largest waveforms. This was done sparingly and more often a large cluster with varying unit amplitudes was classified as a single unit. More refined analysis techniques will be employed in the future to better distinguish individual units that may have been inadvertently grouped together in this study.

Longer term, methods need to be developed that will allow for scaling up manufacturing throughput and even higher densities of carbon fibers. Assembly with silver epoxy could be eliminated using a self-aligning anisotropic epoxy that self-selectively forms electrical connections between fibers and traces (Ramkumar et al. 2011). Innovative methods will be needed for the frontend silicon support structure but also in the backend where dozens if not hundreds of wires (Barrese et al. 2013) will be needed to transmit electrophysiology data. Packaging arrays with an ASIC capable of multiplexing hundreds of channels (Viventi et al. 2011) would alleviate many wiring issues (Du et al. 2011; Berényi et al. 2014) or completely eliminate them (Borton et al. 2013; Miranda et al. 2010; Gao et al. 2012). The convergence of these technologies could lead to an electrode pitch dense enough to record from all neurons in a given space for long periods of time.

2.7 References

Armstrong-James, M. & Millar, J., 1979. Carbon fibre microelectrodes. *Journal of Neuroscience Methods*, 1(3), pp.279–287.

ATSM, F.-07, 2011. Standard Guide for Accelerated Aging of Sterile Barrier Systems for Medical Devices. (ATSM F1980-07).

Bai, Q., Wise, K.D. & Anderson, D.J., 2000. A high-yield microassembly structure for three-dimensional microelectrode arrays. *IEEE Transactions on Biomedical Engineering*, 47(3), pp.281–289.

Barrese, J.C. et al., 2013. Failure mode analysis of silicon-based intracortical microelectrode arrays in non-human primates. *Journal of Neural Engineering*, 10(6), p.66014.

Berényi, A. et al., 2014. Large-scale, high-density (up to 512 channels) recording of local circuits in behaving animals. *Journal of Neurophysiology*, 111(5), pp.1132–1149.

Biran, R., Martin, D.C. & Tresco, P.A., 2005. Neuronal cell loss accompanies the brain tissue response to chronically implanted silicon microelectrode arrays. *Experimental Neurology*, 195(1), pp.115–126.

Bjornsson, C.S. et al., 2008. Associative image analysis: a method for automated quantification of 3D multi-parameter images of brain tissue. *Journal of Neuroscience Methods*, 170(1), pp.165–178.

Borton, D.A. et al., 2013. An implantable wireless neural interface for recording cortical circuit dynamics in moving primates. *Journal of Neural Engineering*, 10(2), p.26010.

Budai, D., 2010. *Carbon Fiber-based Microelectrodes and Microbiosensors, Intelligent and Biosensors* V. S. Somerset, ed., InTech.

Carmena, J.M. et al., 2003. Learning to control a brain-machine interface for reaching and grasping by primates. *PLoS Biology*, 1(2), pp.193–208.

Carter, R.R. & Houk, J.C., 1993. Multiple single-unit recordings from the CNS using thin-film electrode arrays. *IEEE Transactions on Rehabilitation Engineering*, 1(3), pp.175–184.

Chen, Z.J. et al., 2004. A realistic brain tissue phantom for intraparenchymal infusion studies. *Journal of Neurosurgery*, 101(2), pp.314–322.

Dolbow, J. & Gosz, M., 1996. Effect of out-of-plane properties of a polyimide film on the stress fields in microelectronic structures. *Mechanics of Materials*, 23(4), pp.311–321.

Du, J. et al., 2011. Multiplexed, High Density Electrophysiology with Nanofabricated Neural Probes. *PLoS ONE*, 6(10), pp.e26204–e26204.

Edell, D.J. et al., 1992. Factors influencing the biocompatibility of insertable silicon microshafts in cerebral cortex. *IEEE Transactions on Biomedical Engineering*, 39(6), pp.635–643.

Ferris, M.J. et al., 2013. Examining the Complex Regulation and Drug-Induced Plasticity of Dopamine Release and Uptake Using Voltammetry in Brain Slices. *ACS Chemical Neuroscience*, 4(5), pp.693–703.

Gao, H. et al., 2012. HermesE: A 96-Channel Full Data Rate Direct Neural Interface in 0.13 µm CMOS. *IEEE Journal of Solid-state Circuits*, 47(4), pp.1043–1055.

Gilgunn, P.J. et al., 2012. An ultra-compliant, scalable neural probe with molded biodissolvable delivery vehicle. *2012 IEEE 25th International Conference on Micro Electro Mechanical Systems*, pp.56–59.

Grand, L. et al., 2010. Short and long term biocompatibility of NeuroProbes silicon probes. *Journal of Neuroscience Methods*, 189(2), pp.216–229.

Green, R.A. et al., 2012. Substrate dependent stability of conducting polymer coatings on medical electrodes. *Biomaterials*, 33(25), pp.5875–5886.

Guitchounts, G. et al., 2013. A carbon-fiber electrode array for long-term neural recording. *Journal of Neural Engineering*, 10(4), p.46016.

Harris, J.P., Hess, A.E., et al., 2011. In vivo deployment of mechanically adaptive nanocomposites for intracortical microelectrodes. *Journal of Neural Engineering*, 8(4), p.46010.

Harris, J.P., Capadona, J.R., et al., 2011. Mechanically adaptive intracortical implants improve the proximity of neuronal cell bodies. *Journal of Neural Engineering*, 8(6), p.66011.

Heien, M.L.A. V, Johnson, M.A. & Wightman, R.M., 2004. Resolving neurotransmitters detected by fast-scan cyclic voltammetry. *Analytical Chemistry*, 76(19), pp.5697–5704.

Hochberg, L.R. et al., 2006. Neuronal ensemble control of prosthetic devices by a human with tetraplegia. *Nature*, 442(7099), pp.164–171.

Hsu, J.-M. et al., 2009. Encapsulation of an Integrated Neural Interface Device With Parylene C. *IEEE Transactions on Biomedical Engineering*, 56(1), pp.23–29.

Hukins, D.W.L., Mahomed, A. & Kukureka, S.N., 2008. Accelerated aging for testing polymeric biomaterials and medical devices. *Medical Engineering & Physics*, 30(10), pp.1270–1274.

Johnson, M.D., Kao, O.E. & Kipke, D.R., 2007. Spatiotemporal pH dynamics following insertion of neural microelectrode arrays. *Journal of Neuroscience Methods*, 160(2), pp.276–287.

Karumbaiah, L. et al., 2013. Relationship between intracortical electrode design and chronic recording function. *Biomaterials*, 34(33), pp.8061–8074.

Kim, B.J. et al., 2013. 3D Parylene sheath neural probe for chronic recordings. *Journal of Neural Engineering*, 10(4), p.45002.

Kipke, D.R. et al., 2003. Silicon-substrate intracortical microelectrode arrays for long-term recording of neuronal spike activity in cerebral cortex. *IEEE Transactions on Neural Systems and Rehabilitation Engineering*, 11(2), pp.151–155.

Kozai, T.D.Y., Jaquins-Gerstl, A.S., et al., 2015. Brain Tissue Responses to Neural Implants Impact Signal Sensitivity and Intervention Strategies. *ACS Chemical Neuroscience*, 6(1), pp.48–67.

Kozai, T.D.Y., Gugel, Z., et al., 2014. Chronic tissue response to carboxymethyl cellulose based dissolvable insertion needle for ultra-small neural probes. *Biomaterials*, 35(34), pp.9255–9268.

Kozai, T.D.Y., Du, Z., et al., 2015. Comprehensive chronic laminar single-unit, multi-unit, and local field potential recording performance with planar single shank electrode arrays. *Journal of Neuroscience Methods*, 242(0), pp.15–40.

Kozai, T.D.Y., Li, X., et al., 2014. Effects of caspase-1 knockout on chronic neural recording quality and longevity: Insight into cellular and molecular mechanisms of the reactive tissue response. *Biomaterials*, 35(34), pp.9255–9268.

Kozai, T.D.Y., Vazquez, A.L., et al., 2012. In vivo two-photon microscopy reveals immediate microglial reaction to implantation of microelectrode through extension of processes. *Journal of Neural Engineering*, 9(6), p.66001.

Kozai, T.D.Y., Catt, K., et al., 2015. Mechanical failure modes of chronically implanted planar silicon-based neural probes for laminar recording. *Biomaterials*, 37(0), pp.25–39.

Kozai, T.D.Y. et al., 2010. Reduction of neurovascular damage resulting from microelectrode insertion into the cerebral cortex using in vivo two-photon mapping. *Journal of Neural Engineering*, 7(4), p.46011.

Kozai, T.D.Y., Langhals, N.B., et al., 2012. Ultrasmall implantable composite microelectrodes with bioactive surfaces for chronic neural interfaces. *Nature Materials*, 11(12), pp.1065–1073.

Kozai, T.D.Y. & Kipke, D.R., 2009. Insertion shuttle with carboxyl terminated self-assembled monolayer coatings for implanting flexible polymer neural probes in the brain. *Journal of Neuroscience Methods*, 184(2), pp.199–205.

Li, P.C. et al., 2006. Imaging cerebral blood flow through the intact rat skull with temporal laser speckle imaging. *Optics Letters*, 31(12), pp.1824–1826.

Liu, X. et al., 1999. Stability of the interface between neural tissue and chronically implanted intracortical microelectrodes. *IEEE Transactions on Rehabilitation Engineering*, 7(3), pp.315–326.

Mahoney, M.J. & Anseth, K.S., 2006. Three-dimensional growth and function of neural tissue in degradable polyethylene glycol hydrogels. *Biomaterials*, 27(10), pp.2265–2274.

MatWeb, 2012. Cytec Thornel® T-650/35 3K Carbon Fiber, Polyacrylonitrile (PAN) Precursor. Available at: http://www.matweb.com/search/DataSheet.aspx?MatGUID=7e9aca60a2e84538a4e8038784f2b629&ckck=1.

McClain, M. et al., 2011. Highly-compliant, microcable neuroelectrodes fabricated from thin-film gold and PDMS. *Biomedical Microdevices*, 13, pp.361–373.

McConnell, G.C. et al., 2009. Implanted neural electrodes cause chronic, local inflammation that is correlated with local neurodegeneration. *Journal of Neural Engineering*, 6(5), p.56003.

Miranda, H. et al., 2010. HermesD: A High-Rate Long-Range Wireless Transmission System for Simultaneous Multichannel Neural Recording Applications. *IEEE Transactions on Biomedical Circuits and Systems*, 4(3), pp.181–191.

Moffitt, M.A. & McIntyre, C.C., 2005. Model-based analysis of cortical recording with silicon microelectrodes. *Clinical Neurophysiology*, 116(9), pp.2240–2250.

Muthuswamy, J. et al., 2003. Microactuated neural probes to compensate for brain micromotion. *2003 Annual International Conference of the IEEE Engineering In Medicine and Biology Society*, 2, pp.1941–1943.

Negi, S. et al., 2010. In vitro comparison of sputtered iridium oxide and platinum-coated neural implantable microelectrode arrays. *Biomedical Materials*, 5(1), p.15007.

Nicolelis, M.A.L. et al., 2003. Chronic, multisite, multielectrode recordings in macaque monkeys. *Proceedings of the National Academy of Sciences*, 100(19), pp.11041–11046.

Nordhausen, C.T., Maynard, E.M. & Normann, R.A., 1996. Single unit recording capabilities of a 100 microelectrode array. *Brain Research*, 726(1-2), pp.129–140.

Normann, R.A. et al., 1999. A neural interface for a cortical vision prosthesis. *Vision Research*, 39(15), pp.2577–2587.

Nunamaker, E.A. & Kipke, D.R., 2010. An alginate hydrogel dura mater replacement for use with intracortical electrodes. *Journal of Biomedical Materials Research Part B: Applied Biomaterials*, 95B(2), pp.421–429.

Park, J., Takmakov, P. & Wightman, R.M., 2011. In vivo comparison of norepinephrine and dopamine release in rat brain by simultaneous measurements with fast-scan cyclic voltammetry. *Journal of Neurochemistry*, 119(5), pp.932–944.

Paxinos, G. & Watson, C., 2007. *The Rat Brain in Stereotaxic Coordinates*, Academic Press.

Polikov, V.S., Tresco, P.A. & Reichert, W.M., 2005. Response of brain tissue to chronically implanted neural electrodes. *Journal of Neuroscience Methods*, 148(1), pp.1–18.

Ponchon, J.L. et al., 1979. Normal Pulse Polarography With Carbon-fiber Electrodes For Invitro and Invivo Determination of Catecholamines. *Analytical Chemistry*, 51(9), pp.1483–1486.

Potter, K.A. et al., 2012. Stab injury and device implantation within the brain results in inversely multiphasic neuroinflammatory and neurodegenerative responses. *Journal of Neural Engineering*, 9(4), p.46020.

Prasad, A. et al., 2014. Abiotic-biotic characterization of Pt/Ir microelectrode arrays in chronic implants. *Frontiers in neuroengineering*, 7, pp.1–15.

Ramkumar, S.M., Venugopalan, H. & Khanna, K., 2011. Novel Anisotropic Conductive Adhesive for 3D Stacking and Lead-free PCB Packaging - A Review. *2011 IEEE 61st Electronic Components and Technology Conference*, pp.246–254.

Rebec, G. V et al., 1997. Regional and temporal differences in real-time dopamine efflux in the nucleus accumbens during free-choice novelty. *Brain Research*, 776(1-2), pp.61–67.

Rennaker, R.L. et al., 2005. An economical multi-channel cortical electrode array for extended periods of recording during behavior. *Journal of Neuroscience Methods*, 142(1), pp.97–105.

Riera, J.J. et al., 2012. Pitfalls in the dipolar model for the neocortical EEG sources. *Journal of Neurophysiology*, 108(4), pp.956–975.

Rousche, P.J. et al., 2001. Flexible polyimide-based intracortical electrode arrays with bioactive capability. *IEEE Transactions on Biomedical Engineering*, 48(3), pp.361–371.

Sankar, V. et al., 2014. Electrode impedance analysis of chronic tungsten microwire neural implants: understanding abiotic vs. biotic contributions. *Frontiers in Neuroengineering*, 7, pp.1–12.

Saxena, T. et al., 2013. The impact of chronic blood-brain barrier breach on intracortical electrode function. *Biomaterials*, 34(20), pp.4703–4713.

Schmidt, S., Horch, K. & Normann, R., 1993. Biocompatibility of Silicon-based Electrode Arrays Implanted In Feline Cortical Tissue. *Journal of Biomedical Materials Research*, 27(11), pp.1393–1399.

Schwartz, A.B., 2004. Cortical Neural Prosthetics. *Annual Review of Neuroscience*, 27(1), pp.487–507.

Seymour, J.P. & Kipke, D.R., 2007. Neural probe design for reduced tissue encapsulation in CNS. *Biomaterials*, 28(25), pp.3594–3607.

Simeral, J.D. et al., 2011. Neural control of cursor trajectory and click by a human with tetraplegia 1000 days after implant of an intracortical microelectrode array. *Journal of Neural Engineering*, 8(2), p.25027.

Skoglund, T.S., Pascher, R. & Berthold, C.H., 1997. The existence of a layer IV in the rat motor cortex. *Cerebral Cortex*, 7(2), pp.178–180.

Skousen, J.L. et al., 2011. Reducing surface area while maintaining implant penetrating profile lowers the brain foreign body response to chronically implanted planar silicon microelectrode arrays. *Progress in Brain Research*, 194, pp.167–180.

Szarowski, D.H. et al., 2003. Brain responses to micro-machined silicon devices. *Brain Research*, 983(1-2), pp.23–35.

Takeuchi, S. et al., 2005. Parylene flexible neural probes integrated with microfluidic channels. *Lab*, 5, pp.519–523.

Turner, J.N. et al., 1999. Cerebral Astrocyte Response to Micromachined Silicon Implants. *Experimental Neurology*, 156(1), pp.33–49.

Vetter, R.J. et al., 2004. Chronic neural recording using silicon-substrate microelectrode arrays implanted in cerebral cortex. *IEEE Transactions on Biomedical Engineering*, 51(6), pp.896–904.

Viventi, J. et al., 2011. Flexible, foldable, actively multiplexed, high-density electrode array for mapping brain activity in vivo. *Nature Neuroscience*, 14(12), pp.1599–1605.

Ware, T. et al., 2014. Thiol-ene/acrylate substrates for softening intracortical electrodes. *Journal of Biomedical Materials Research Part B: Applied Biomaterials*, 102(1), pp.1–11.

Ware, T. et al., 2012. Three-Dimensional Flexible Electronics Enabled by Shape Memory Polymer Substrates for Responsive Neural Interfaces. *Macromolecular Materials and Engineering*, 297(12), pp.1193–1202.

Wark, H.A.C. et al., 2013. A new high-density (25 electrodes/mm2) penetrating microelectrode array for recording and stimulating sub-millimeter neuroanatomical structures. *Journal of Neural Engineering*, 10(4), p.45003.

Williams, J.C., Rennaker, R.L. & Kipke, D.R., 1999. Long-term neural recording characteristics of wire microelectrode arrays implanted in cerebral cortex. *Brain Research Protocols*, 4(3), pp.303–313.

Winslow, B.D. & Tresco, P.A., 2010. Quantitative analysis of the tissue response to chronically implanted microwire electrodes in rat cortex. *Biomaterials*, 31(7), pp.1558–1567.

Wise, K.D. et al., 2004. Wireless implantable microsystems: High-density electronic interfaces to the nervous system. *Proceedings of the IEEE*, 92(1), pp.76–97.

CHAPTER III

Histological Comparison of Chronically Implanted Carbon Fiber Microelectrode Arrays and Planar Silicon Electrodes

3.1 Abstract

Objective. Individual carbon fiber microelectrodes have been shown to reduce the reactive response typically caused by larger penetrating microelectrodes. New work has also demonstrated the fabrication and insertion of an array using 16 carbon fiber microelectrodes. A 3 month histology study was carried out to compare the reactive response of implanted tissue to both traditional silicon electrodes and the new carbon fiber arrays. *Approach.* Two animals were chronically implanted with both a carbon fiber array and a silicon electrode for 91 days. At the end of the study, animals were perfused and the brain tissue sectioned and sliced. Tissue sections were stained for astrocytes, microglia, and neurons, using immunohistochemistry methods. The local reactive responses were assessed using qualitative and quantitative methods. *Main results.* Carbon fiber arrays showed a minimal to non-existent glial scarring response when compared to silicon electrodes. In the case where the carbon fibers showed an elevated microglial response, neuronal density counts showed no adverse consequences as a result of the increase. Conversely, silicon electrodes showed large glial scarring that

impacted neuronal density. *Significance*. This study has demonstrated the validity of using carbon fiber microelectrode arrays for chronic electrophysiology applications. In addition, the minimal reactive response seen here should hold stable for longer time points, as any response by the immune system will reach a steady state after 12 weeks.

3.2 Introduction

Detecting localized neuronal activity in the brain is crucial to deciphering how a highly intricate communication network of neurons can lead to abilities such as movement (Kaufman et al. 2010; Lecas et al. 1986; Alexander & Crutcher 1990), memory (O'Keefe & Speakman 1987; Ferbinteanu & Shapiro 2003), and vision (Rousche & Normann 1998). This information can then be used for treating individuals suffering from neurological disorders such as Alzheimer's and depression, or aid amputees and spinal cord injury patients through the use of brain machine interface (BMI) systems (Carmena et al. 2003; Simeral et al. 2011; Hochberg et al. 2006; Chestek et al. 2011; Collinger et al. 2013; Velliste et al. 2008; Hochberg et al. 2012; Taylor et al. 2003; Schwartz et al. 2006). Achieving these goals often requires the use of penetrating electrodes inserted into the region(s) of interest for many months if not years. Unfortunately, the electrodes, while excellent at detecting localized activity, also fail over time due to a chronic inflammatory response.

The initial insertion of any electrode is a traumatic event to the local cellular network and vasculature and is greatly influenced by insertion speed (Bjornsson et al. 2006; Johnson et al. 2007), location (Kozai et al. 2010), and technique (Rennaker, Street, et al. 2005; Rousche & Normann 1992). If the electrode is removed soon after insertion, the local area will heal (Potter et al. 2012; Biran et al. 2005). Permanent implantation of

the electrode leads to the eventual formation of a localized glial scar comprised chiefly of astrocytes and microglia (Edell et al. 1992; Carter & Houk 1993; Schmidt et al. 1993; Turner et al. 1999; Liu et al. 1999; Szarowski et al. 2003; Biran et al. 2005; Polikov et al. 2005; McConnell et al. 2009; Grand et al. 2010; Winslow & Tresco 2010; Kozai, Vazquez, et al. 2012; Ersen et al. 2015). Accompanying the scar is a varying degree of neuronal cell death within the immediate vicinty of the electrode (Edell et al. 1992; Liu et al. 1999; Winslow & Tresco 2010; Biran et al. 2005). The persistance of the scar can be attributed to multiple factors including the continual release of inflammatory factors by the locally activated glial cells (Polikov et al. 2005; Guilian et al. 1993; McConnell et al. 2009) and a breached blood brain barrier that can't completely heal, therefore allowing the infiltration of pro-inflammatory cells and chemokines (Saxena et al. 2013; Potter et al. 2012). The impact that these chemokines have on the local environment has been shown through the use of genetic knockouts. The removal of monocyte chemoattractant protein 1 led to improved neuronal density (Sawyer et al. 2014) while caspase-1 knockout mice demonstrated significantly better recording quality as compared to wild type mice (Kozai et al. 2014).

While individual knockout studies help to pinpoint areas that may serve as the best targets for therapeutic interventions, others have taken a different approach. The localized delivery of dexamethasone, an anti-inflammatory drug, has been shown to reduce the glial scar and improve neuronal survivability (Zhong & Bellamkonda 2007; Kolarcik et al. 2015; Grand et al. 2010). Immobilizing anti-inflammatory agents directly at the probe's surface can also attenuate the reactive response (He et al. 2007; Azemi et

al. 2008; He et al. 2006). Another approach is the seeding of stem cells directly on to the electrode prior to implantation (Azemi et al. 2010; Purcell et al. 2009).

Drug and cell seeding techniques may yield short term results, but their lack of availability to the environment in the long term, raises the possibility of a return to a typical reactive response. A more permanent solution explores changing the fundamental design principles used to construct electrodes. While traditional electrodes are made from metals such as silicon (Najafi et al. 1985; Vetter et al. 2005; Campbell et al. 1991; Nordhausen et al. 1996) and tungsten (Rennaker, Ruyle, et al. 2005; Williams et al. 1999; Nicolelis et al. 2003), newer electrodes are being fabricated from softer materials such as polyimide (Rousche et al. 2001; Mercanzini et al. 2008; Lai et al. 2012; Sankar et al. 2013; Xiang et al. 2014; Jeon et al. 2014; Cheung et al. 2007) and parylene-c (Kuo et al. 2013; Takeuchi et al. 2005) that more closely match the Young's modulus of the brain. Many of these softer devices are also larger than traditional electrodes and can cause the same reactive response they intended to prevent.

However, the most promising solution to date has been to drastically reduce the width and thickness of the electrode. Multiple studies using non-functional devices have shown that smaller electrode dimensions leads to a reduction in the inflammatory response and an increase in neuronal density immediately surrounding the electrode (Karumbaiah et al. 2013; Stice et al. 2007; Seymour & Kipke 2007; Skousen et al. 2011). Skousen et al. specifically showed that a lattice style electrode, with its greatly reduced surface area, had significantly improved normalized neuronal density (~90%) within a 50 μm radius, compared to a solid device (~40%) with the same footprint (Skousen et al. 2011). This latter point is crucial as the estimated recording radius of an electrode is

approximately ~75 μm (Moffitt & McIntyre 2005). Therefore, any improvement in neuronal density in the immediate vicinity of the recording electrode would improve detection of unit activity. An added benefit of this design style is its permanence; the electrode does not change over time and any effects seen in the short term should last in the long term.

Recent work has shown the efficacy and minimal reactive response to single carbon fiber electrodes that have been implanted for approximately one month (Kozai, Langhals, et al. 2012). This strongly suggests that an array of carbon fiber electrodes will also cause a minimal reactive response when implanted for 3 months. To test this, two animals were chronically implanted with a set of carbon fiber arrays and standard silicon planar electrodes. Histology results showed macroscopic scarring and widespread elevation of astrocyte and microglia activity surrounding the silicon electrodes, with little to no response in the carbon fiber arrays' implant region. Most importantly, neuronal density surrounding the carbon fiber implants was well maintained, while the area surrounding the silicon implant site showed a decrease in neuronal density.

3.3 Materials & Methods

3.3.1 Carbon Fiber Array Preparation for Chronic Implants

Carbon fiber arrays were fabricated as described in section 2.3.1.1. Once fully assembled all carbon fiber arrays were coated with an 800 nm thick insulating layer of parylene-c using a Parylene Deposition System 2010 (SCS Coatings, Indianapolis, IN). The final preparation step was a coating of poly(ethylene glycol) (PEG) as described in section 2.3.2.1.

3.3.2 Surgery for Chronic Implantation of Carbon Fibers and Silicon Probes

Chronic implantation of carbon fiber arrays used adult male Long Evans rats (n=2) weighing 300 – 350 g. Rats were first anesthetized using 5% isoflurane (v/v) for induction and then 1 – 3% isoflurane (v/v) to maintain anesthesia. The head was then shaved at and around the area of the incision site. The shaved area was triple swabbed using alternating applications of betadine and 70% ethanol. Ointment was applied to the eyes to keep them from drying during surgery. Once mounted in the ear bars of the stereotax, the shaved area was swabbed one more time with betadine followed by 70% ethanol. A subcutaneous injection of lidocaine (4 mg/mL) was given at the proposed site of incision at a maximum dosage of 4 mg lidocaine per 1 kg of body weight. After incision, the skin flaps were pulled away using hemostats and the skull surface cleaned using a combination of cotton swabs and 2% hydrogen peroxide (v/v). A burr bit (19008-07, Fine Science Tools, Foster City, CA) was used to drill seven holes around the periphery of the skull for seven bone screws (19010-00, Fine Science Tools, Foster City, CA). Next, 2 mm x 3 mm craniotomies were made over the left and right motor cortex using coordinates from a reference atlas (Paxinos & Watson 2007). Before resecting the dura, a layer of Kwik-Sil (World Precision Instruments, Sarasota, FL) was applied to the skull at the posterior, anterior, and leftmost sides.

Following the resection of the dura on the rightmost craniotomy, the PEG coated carbon fiber array was brought to the surface of the brain. The exposed fibers were driven into the brain manually using the stereotactic manipulator and depth was monitored using a digital readout. The insertion of the exposed fibers took approximately 5 – 10 seconds. Once the PEG coated portion of the fibers reached the brain's surface, manual insertion was halted. Using a syringe filled with room temperature sterile

Lactated Ringer's, a small portion of the PEG nearest to the brain was dissolved away while a surgical spear soaked up the PEG/Ringer's solution. The fibers were then manually driven in further, again taking 5 – 10 seconds for insertion, and more PEG dissolved away until the final target depth was reached. All of the remaining PEG was dissolved away using additional Ringer's.

To implant the silicon probe (A1x16-3mm-50-177-HZ16_21mm, NeuroNexus Technologies, Ann Arbor, MI), a small metal rod was first attached to the stereotactic manipulator and then positioned above the rat's skull. A drop of melted PEG was applied to the very tip of the rod. The base of the silicon probe, which was attached to a polyimide cable, was then positioned such that it was resting in the still liquid PEG. Once solidified, the PEG held the probe in place which allowed for precise placement with the manipulator. The dura over the leftmost craniotomy was resected and the probe was implanted to the final desired depth. The polyimide cable connecting the probe to the PCB was secured to the nearest bone screws using Kwil-Sil. This ensured that the tension in the cable would not cause the probe to come out of the brain once released from the rod. After the Kwil-Sil had cured, the PEG was dissolved away using sterile Lactated Ringer's and the rod was retracted.

Additional Kwik-Sil was then applied to the skull at the lateral side of the rightmost craniotomy, forming a complete barrier around both craniotomies. Once the Kwik-Sil had completely cured, the Kwik-Sil barrier was flooded with either Kwik-Cast (World Precision Instruments, Sarasota, FL), petroleum jelly, or alginate (Nunamaker & Kipke 2010). Reference and ground wires originating from both PCBs were attached to the posterior most bone screw. The PCBs were then anchored to all of the skull's bone

screws using dental acrylic. The skin flaps were brought up over the dental acrylic headcap on each side and sutured together at the anterior and posterior ends. Triple antibiotic ointment was liberally applied around the headcap. Animals were then removed from the stereotax and allowed to recover on a heated pad placed under their cage. During surgery, animal vitals were monitored using a pulse-oximeter and rectal temperature probe. All procedures and post-operative care complied with the University of Michigan's University Committee on Use and Care of Animals.

3.3.3 Histology

At day 91, both animals were transcardially perfused with 250 – 300 mL of 1x phosphate buffered saline (PBS) (BP3994, Fisher Scientific, Waltham, MA) followed by 250 – 300 mL of 4% (w/v) paraformaldehyde (P6148, Sigma Aldrich, St. Louis, MO) in 1x PBS. The headcaps, which contained the implanted probes, were separated from the brains. Extracted brains were then soaked in 4% (w/v) paraformaldehyde for an additional 24 hours. Once fixed, the tissue was cryoprotected by successive 24 hour long soaks in 10%, 20%, and finally 30% (w/v) sucrose (BP220, Fisher Scientific, Waltham, MA) in 1x PBS. If the tissue sample had not sunk to the bottom of the solution after 24 hours, additional time was given before moving to the next higher concentration of sucrose. Next, tissue was embedded in Optimal Cutting Tissue Compound (4583, Sakura, Netherlands) and frozen to -20 °C. The frozen sample was sectioned into 20 µm slices using a Microm 550 Cryostat (Fisher Scientific, Waltham, MA) and mounted directly onto slides. A hydrophobic barrier using a PAP pen (22312, Ted Pella, Redding, CA) was drawn around each slice and allowed to dry.

To stain the slices they were first rinsed with 1x PBS for 10 minutes. Next, slices were blocked with 10% goat serum (S-1000, Vector Labs, Burlingame, CA) in 1x PBS for one hour at room temperature. Slices were then incubated in a primary antibody solution containing one or more of the following: Rabbit anti-Iba1 (1:500 dilution) (019-19741, Wako, Richmond, VA), Rabbit anti-GFAP (1:500 dilution) (Z033429-2, Dako, Carpinteria, CA), or Mouse anti-Neun (1:500 dilution) (MAB377, Millipore, Billercia, MA), mixed with 0.3% Triton X-100 (T8787, Sigma Aldrich, St. Louis, MO) and 3% goat serum in 1x PBS, overnight in a covered chamber. The next day, slices were triple rinsed with 1x PBS, with each wash allowed to sit for 10 minutes. Slices were then incubated in a solution of Alexa 488 Goat anti-Rabbit IgG (1:200 dilution) (A-11034, Invitrogen, Grand Island, NY), Alexa 555 Goat anti-Mouse IgG (1:200 dilution) (A-11031, Invitrogen, Grand Island, NY), 0.2% Triton X-100, and 5% goat serum in 1x PBS at room temperature for two hours. The slices were then rinsed twice with 1x PBS with each rinse lasting 10 minutes. Slides were then cover slipped using Prolong Gold (P36930, Invitrogen, Grand Island, NY) and allowed to dry overnight before imaging.
A LSM 510-META Laser Scanning Confocal Microscope (Zeiss, Oberkochen, Germany) was used to image the stained slices.

3.3.4 Image Processing

To generate the heat maps, all acquired fluorescent images were first converted to greyscale. Then, images were imported into Matlab (Mathworks, Natick, MA) and passed through an averaging filter (6 x 6 samples). The output of the filtering was plotted using the surface function.

Neuronal density counts were accomplished using the built in cell counting function in ImageJ 1.48v (http://imagej.nih.gov/ij/).

To generate the signal intensity values immediately surrounding the silicon implant site, first an oval was drawn that best fit the site. The oval was then expanded by 50 μm in all directions and the average intensity of this 50 μm oval ring was calculated. This value was divided by the control value which was calculated by averaging together the intensities of each corner (500 μm x 500 μm) of the image. A different approach was taken for the carbon fibers as it was difficult to determine their exact location. First, 10 coordinates within the image were randomly chosen under the worst case assumption that the array's damage would have far each effects. Each coordinate served as the center for an initial circle that represented the fiber's implant site. Then the circle was expanded by 50 μm in all directions and the average intensity of this 50 μm circular ring was calculated. This was divided by the control intensity value, which was calculated in the same manner as before. When a single tissue slice's intensity was calculated multiple times due to multiple stains, the same exact coordinates and dimensions were used for each region of interest. In addition, it was assumed that the corners of each image would serve as appropriate controls as they were reasonably far away from the implants and therefore would be unaffected.

3.4 Results

In a typical glial scarring response the implant site is surrounded by both astrocytes and microglial cells. To assess the reaction profile of the carbon fiber arrays as compared to silicon electrodes, both cell types were stained for and co-stained with neurons when possible. Determining the location of the silicon electrode was made

evident by the formation of a glial scar. The location of each carbon fiber electrode was difficult to pinpoint in large part because there was no obvious scar. Therefore, once the silicon implant side has been imaged, the stage was moved to the contralateral hemisphere over the same region that was imaged for the silicon electrodes. This ensured that the image taken was that of the right motor cortex where the fibers were known to be implanted.

Though more animals were actually implanted with both probe types, explanted brains from these animals showed swelling of the cortex into the craniotomy. This swelling made it difficult to separate the headcap from the brain without damaging the tissue, which ultimately led to only two animals that were available for histology.

3.4.1 Microglia Response

The reaction profile seen by the silicon electrode (figure 3.1(a)) is typical of that seen by other groups (Biran et al. 2007; Biran et al. 2005; Szarowski et al. 2003; McConnell et al. 2009). The microglial response to the silicon electrodes is punctuated by a higher density of cells immediately surrounding the implant site (figure 3.1(a)). The staining of microglia extends out in all directions; however, the highest intensity peaks (dark red) seen in the heat map (figure 3.1(c)), which roughly correspond to individual cell bodies, are spaced further apart as distance from the implant site is increased. In addition, the fluorescent signal intensity in a 50 μm radius surrounding the scar site was 2.62 times higher than the control signal. The global response to the carbon fiber array (figures 3.1(b) and 3.1(d)) is similar to that of the silicon implant with only one area in the lower right region of figure 3.1(d) pointing to the formation of a potential scar around one fiber site. All other regions do show elevated responses, but no additional clustering

or intensity peaks that would indicate multiple carbon fiber scars which is also corroborated by an average signal intensity of 0.75 in a 50 μm radius surrounding 10 randomly chosen coordinates, when compared to controls.

The same sites stained for microglia were also stained for neurons. In the fluorescent image (figure 3.1(e)) and heat map (figure 3.1(g)), neuronal signal in a 50 μm radius around the electrode site had an intensity of 0.53 and an estimated cell count of 35.6 neurons/cm^2, pointing to decreased neuronal density. These results match well with the increased microglia intensity peaks in figure 3.1(c). The carbon fiber array site shows a healthier neuronal population with a cell count of 78.1 neurons/cm^2 and a signal intensity of 0.95 using the same 10 regions analyzed for microglia intensity. This indicates a minimal impact of the prevalent microglial signal seen before.

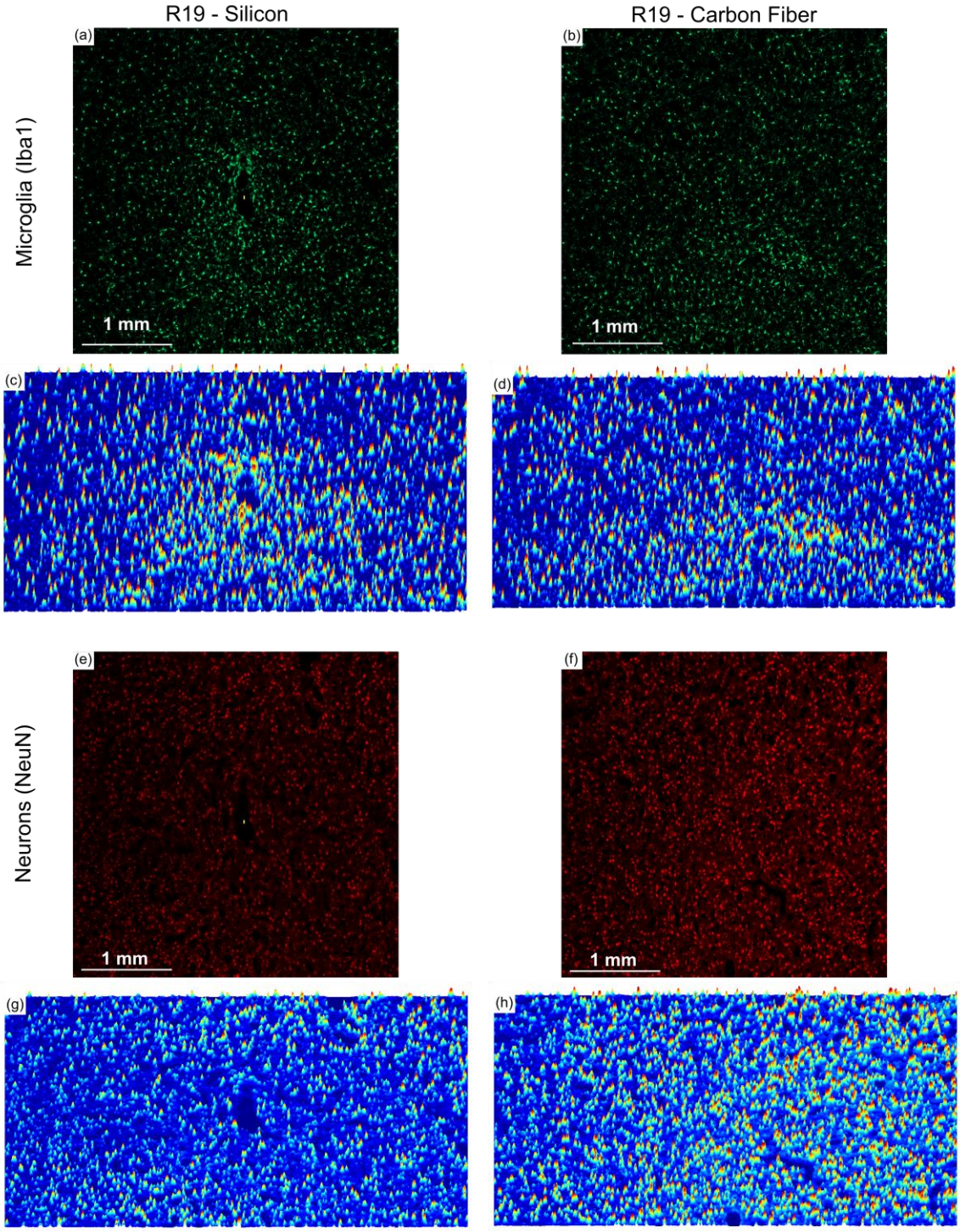

Figure 3.1. Microglia response at electrode depths of ~1.25 mm. (a) & (b) Microglia staining for silicon and carbon fiber electrodes. The yellow rectangle at the center of (a) depicts the approximate location and size (40 µm (w) x 15 µm (h)) of the silicon implant. Though not pictured the footprint of the carbon fiber array is 0.9 mm (w) x 1.74 mm (h). (c) & (d) Heat maps for fluorescent images from (a) & (b). (e) & (f) Neuron staining for silicon and carbon fiber electrodes. The yellow rectangle at the center of the (e) depicts the approximate location and size of the silicon implant. (g) & (h) Heat maps for fluorescent images from (e) & (f).

A more pronounced microglial response can be seen in figure 3.2. The silicon implant site saw the formation of a very large scar that dwarfed the size of the actual electrode (figure 3.2(a) and 3.2(c)) with a 50 µm radial intensity value of 3.17 surrounding the scar. The glial scar that still remains, after what was likely a large piece of tissue being removed during probe explant, indicates that an even larger scar was present during the probe's implant lifetime. Unlike the silicon site, the carbon fiber implant site here shows minimal microglia activity (figure 3.2(b)), with sparse intensity peaks (figure 3.2(d)), and an average signal intensity of 1.14 in a 50 µm radius surrounding 10 randomly chosen coordinates.

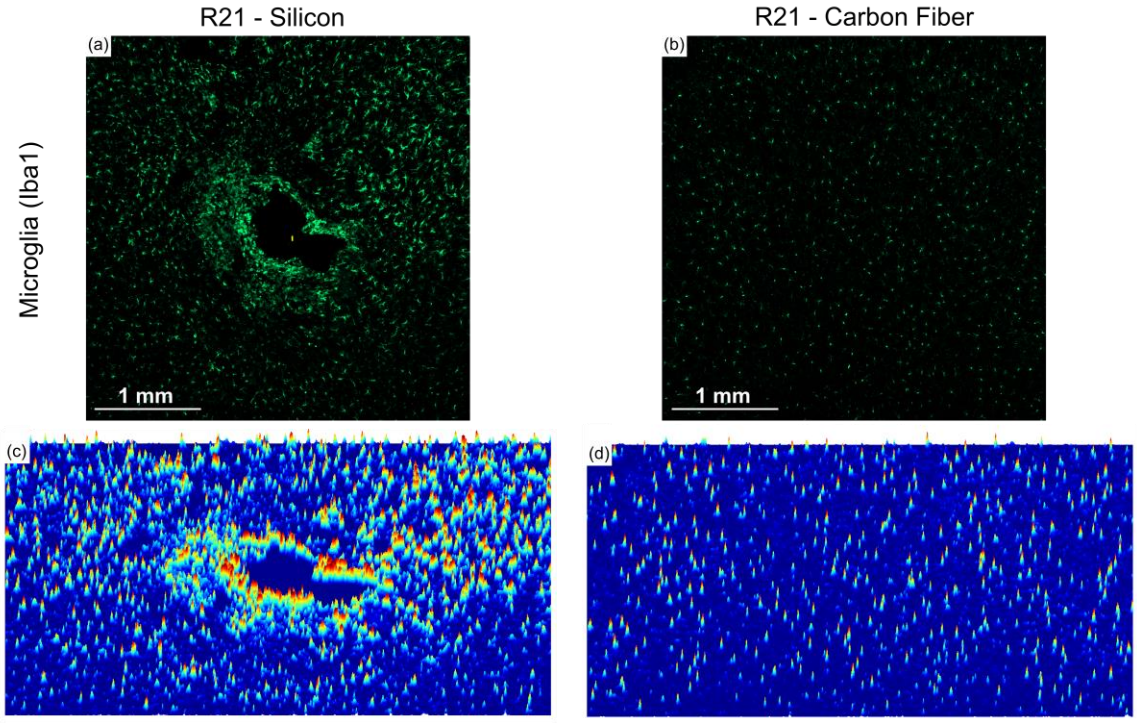

Figure 3.2. Pronounced microglia response. (a) & (b) Microglia staining for silicon and carbon fiber electrodes. The yellow rectangle at the center of (a) depicts the approximate location and size (15 µm (w) x 49 µm (h)) of the silicon implant. Though not pictured the footprint of the carbon fiber array is 0.9 mm (w) x 1.74 mm (h). (c) & (d) Heat maps for fluorescent images from (a) & (b). Response to the silicon electrode was much larger than the actual electrode, pointing to a highly inflamed tissue environment.

3.4.2 Astrocyte Response

The astrocytes have formed a tight scar in the immediate vicinity of the electrode site, with elevated activity that extends outward by as much 1000 μm (figure 3.3(a)). Signal intensity immediately surrounding the first 50 μm of the scar showed a normalized value of 8.68 when compared to control areas. In contrast, the implant site of the carbon fiber array (figure 3.3(b)) shows no visible scarring sites coupled with a lower signal intensity of 2.29 surrounding the first 50 μm of 10 randomly chosen coordinates. Heat maps of both images (figures 3.3(c) and 3.3(d)) allow for a better comparison of the reactive responses. The highest can be seen in the area immediately surrounding the silicon implant site. Moving outward, the intensity is still elevated and extends radially in all directions. The carbon fiber array heat map shows a few scattered peaks of activity, but no discernable pattern to indicate the formation of a scar around each carbon fiber site.

The same tissue slice seen in figures 3.3(a) and 3.3(b), were also stained for neurons (figures 3.3(e) and 3.3(f)), to visualize the impact that scarring may have had on neuronal density. Cell counting in each image yielded a neuronal density of 77.8 neurons/cm^2 for the silicon implant and 84.9 neurons/cm^2 for the carbon fiber array implant. The heat map for the silicon electrode indicates that the peak astrocytic activity in figure 3.3(d) may roughly correspond with areas of possible decreased neuronal signal surrounding the silicon electrode (figure 3.3(g)). In addition, a large cluster of neurons in the lower left region of the image may be skewing the population count to a higher value. The heat map for the carbon fiber implant site (figure 3.3(h)) shows no region specific decrease in neuronal signal that can be matched to the astrocyte heat map (figure 3.3(d)).

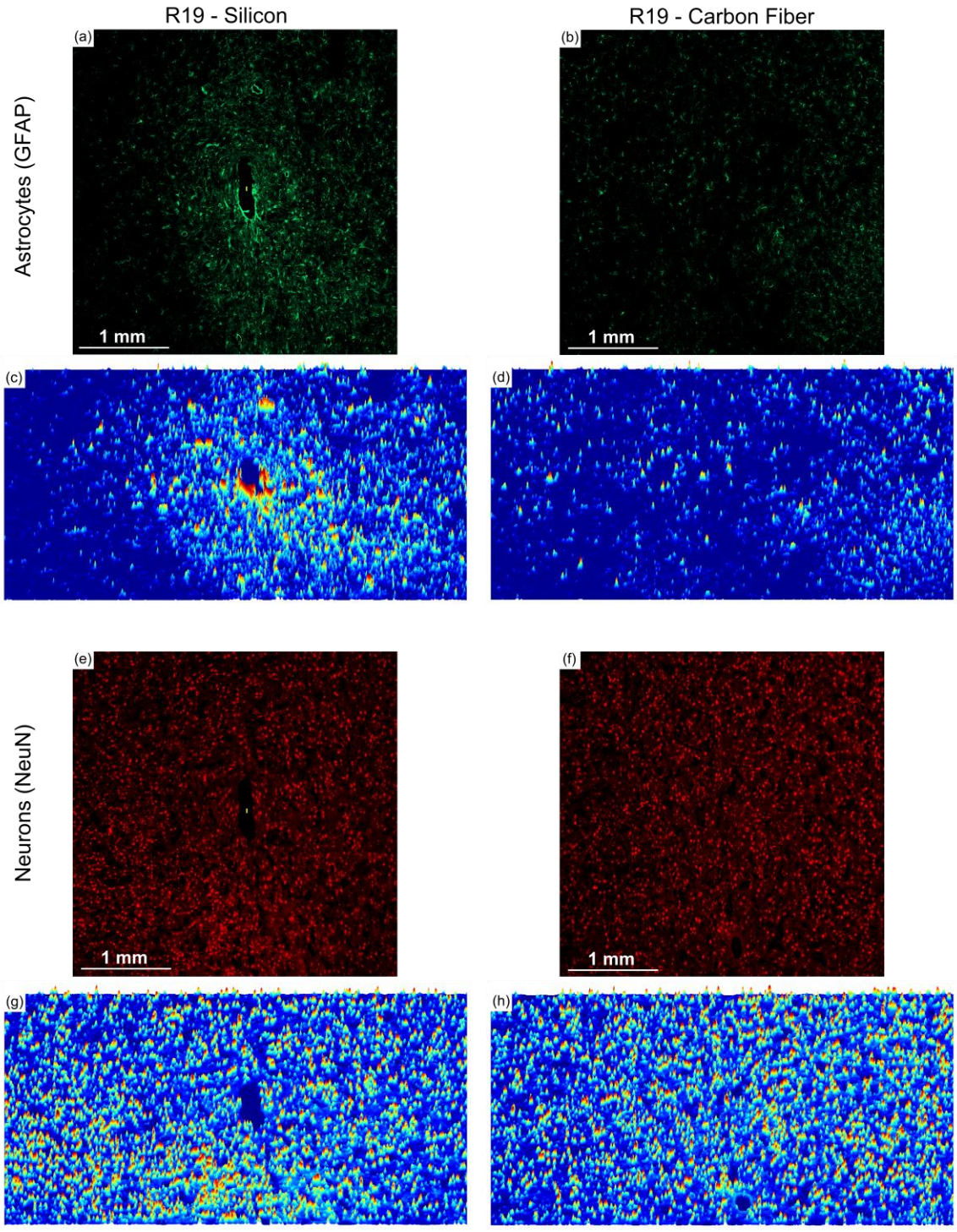

Figure 3.3. Astrocyte response at electrode depths of ~1.2 mm. (a) & (b) Astrocyte staining for silicon and carbon fiber electrodes. The yellow rectangle at the center of (a) depicts the approximate location and size (15 µm (w) x 52 µm (h)) of the silicon implant. Though not pictured the footprint of the carbon fiber array is 0.9 mm (w) x 1.74 mm (h). (c) & (d) Heat maps for fluorescent images from (a) & (b). (e) & (f) Neuron staining for silicon and carbon fiber electrodes. The yellow rectangle at the center of the (e) depicts the approximate location and size of the silicon implant. (g) & (h) Heat maps for fluorescent images from (e) & (f).

The lack of neuronal cell death surrounding both the first 50 μm of the silicon electrode implant site in figure 3.3(e) and of 10 randomly chosen sites in figure 3.3(f) is reflected in the respective signal intensity values of 1.05 and 0.88.

In the same animal that saw a more pronounced microglial response a similar response was seen with astrocytes. Figures 3.4(a) and 3.4(c), show a dense and high intensity astrocytic response around the silicon implant site, with a 50 μm radial intensity value of 87.7 surrounding the scar. While a sizeable portion of the tissue was likely removed during probe extraction, there still remains a tight and highly elevated astrocytic response indicating a far reaching response to the implanted electrode. In the same tissue section in the other hemisphere, implanted carbon fibers saw a much less pronounced astrocytic response (figures 3.4(b) and 3.4(d)) with an average signal intensity of 3.77 in a 50 μm radius surrounding 10 randomly chosen coordinates.

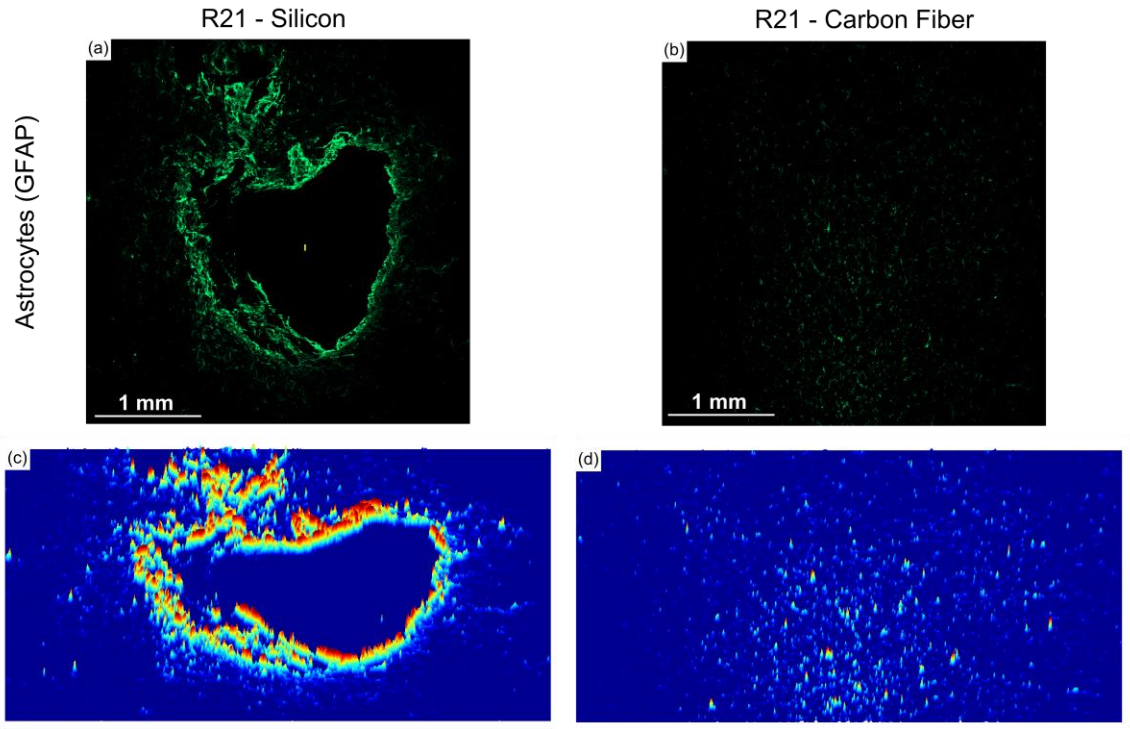

Figure 3.4. Pronounced astrocyte response. (a) & (b) Astrocyte staining for silicon and carbon fiber electrodes. The yellow rectangle at the center of (a) depicts the approximate location and size (15 µm (w) x 61 µm (h)) of the silicon implant. Though not pictured the footprint of the carbon fiber array is 0.9 mm (w) x 1.74 mm (h). (c) & (d) Heat maps for fluorescent images from (a) & (b). Response to the silicon electrode was much larger than the actual electrode, pointing to a highly inflamed tissue environment.

3.5 Discussion

The scarring response for both silicon electrodes varied from compact scars to extremely large reactions that spanned 100s of µm. These reactive responses were coupled with a local decrease in neuronal density as seen in the fluorescent images, their corresponding heat maps, actual density counts, and signal intensity analysis. This reaction is to be expected as glial scarring is often associated with local neuronal death. Unlike the silicon electrodes, the reactive response to the carbon fiber arrays was minimal in most cases. Most important was the healthy neuronal density in all images, even when the reactive response appeared elevated as seen in figure 3.1(b).

As both animals were sacrificed at day 91, it is unlikely that the local tissue environment for either probe type would change significantly after this time (Polikov et al. 2005; Turner et al. 1999). While the chronic response is clear, there is the possibility that damage to the tissue was done during the initial insertion of the carbon fibers; however, the chronic tissue response points to no residual effects as indicated by a healthy neuronal population and low activity of astrocytes and microglia. The specific response to the carbon fiber arrays matches well with other groups who have studied the use of small probe architectures and their corresponding chronic reactive response (Seymour & Kipke 2006; Skousen et al. 2011).

With the most important properties of this electrode having been demonstrated with histological staining and analysis, another benefit from implanting such a small electrode is the ability to slice the electrode in place. In a separate surgery, individual carbon fibers were manually placed in the brain, without any specific spacing, before sacrificing the animal. With fibers in place, the sample was sectioned into 20 μm thick slices. Though no specific staining was carried out, the fibers can clearly been seen in the tissue (figure 3.5). This unique property of the carbon fiber electrodes greatly enhances their attractiveness as a recording technology.

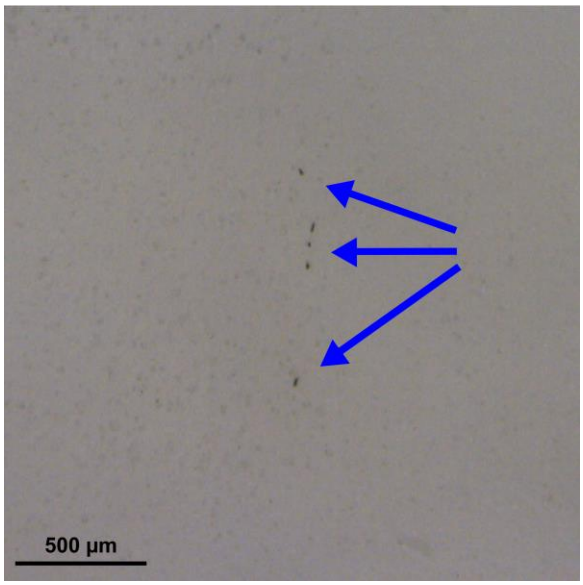

Figure 3.5. Sliced carbon fibers. Carbon fibers (blue arrows) that were implanted and then sliced in place when the brain underwent cryosectioning.

3.6 Conclusion

This work has shown that the small footprint and minimally damaging nature of the carbon fibers has been maintained when fabricated into an array, demonstrating the validity of this material to serve as a long-term recording electrode. Any elevated astrocytic or microglial activity is unlikely to worsen as the time point studied here is when traditional scars are known to stabilize. In addition, the neuronal density of the carbon fiber implants was equal to or better than that of sites with traditional silicon implants, further illustrating their non-damaging nature. The data presented here show that carbon fiber arrays will enable us to record from functioning neural circuitry from freely moving animals over long time periods.

3.7 References

Alexander, G.E. & Crutcher, M.D., 1990. Preparation for movement: neural representations of intended direction in three motor areas of the monkey. *Journal of Neurophysiology*, 64(1), pp.133–150.

Azemi, E. et al., 2008. Surface immobilization of neural adhesion molecule L1 for improving the biocompatibility of chronic neural probes: In vitro characterization. *Acta Biomaterialia*, 4(5), pp.1208–1217.

Azemi, E., Gobbel, G.T. & Cui, X.T., 2010. Seeding neural progenitor cells on silicon-based neural probes. *Journal of Neurosurgery*, 113(3), pp.673–681.

Biran, R., Martin, D.C. & Tresco, P.A., 2005. Neuronal cell loss accompanies the brain tissue response to chronically implanted silicon microelectrode arrays. *Experimental Neurology*, 195(1), pp.115–126.

Biran, R., Martin, D.C. & Tresco, P.A., 2007. The brain tissue response to implanted silicon microelectrode arrays is increased when the device is tethered to the skull. *Journal of Biomedical Materials Research Part A*, 82(1), pp.169–178.

Bjornsson, C.S. et al., 2006. Effects of insertion conditions on tissue strain and vascular damage during neuroprosthetic device insertion. *Journal of Neural Engineering*, 3(3), pp.196–207.

Campbell, P.K. et al., 1991. A Silicon-Based, Three-Dimensional Neural Interface - Manufacturing Processes For An Intracortical Electrode Array. *IEEE Transactions On Biomedical Engineering*, 38(8), pp.758–768.

Carmena, J.M. et al., 2003. Learning to control a brain-machine interface for reaching and grasping by primates. *PLoS Biology*, 1(2), pp.193–208.

Carter, R.R. & Houk, J.C., 1993. Multiple single-unit recordings from the CNS using thin-film electrode arrays. *IEEE Transactions on Rehabilitation Engineering*, 1(3), pp.175–184.

Chestek, C.A. et al., 2011. Long-term stability of neural prosthetic control signals from silicon cortical arrays in rhesus macaque motor cortex. *Journal of Neural Engineering*, 8(4), p.45005.

Cheung, K.C. et al., 2007. Flexible polyimide microelectrode array for in vivo recordings and current source density analysis. *Biosensors and Bioelectronics*, 22(8), pp.1783–1790.

Collinger, J.L. et al., 2013. High-performance neuroprosthetic control by an individual with tetraplegia. *The Lancet*, 381(9866), pp.557–564.

Edell, D.J. et al., 1992. Factors influencing the biocompatibility of insertable silicon microshafts in cerebral cortex. *IEEE Transactions on Biomedical Engineering*, 39(6), pp.635–643.

Ersen, A. et al., 2015. Chronic tissue response to untethered microelectrode implants in the rat brain and spinal cord. *Journal of Neural Engineering*, 12(1), p.16019.

Ferbinteanu, J. & Shapiro, M.L., 2003. Prospective and Retrospective Memory Coding in the Hippocampus. *Neuron*, 40(6), pp.1227–1239.

Grand, L. et al., 2010. Short and long term biocompatibility of NeuroProbes silicon probes. *Journal of Neuroscience Methods*, 189(2), pp.216–229.

Guilian, D. et al., 1993. Reactive Mononuclear Phagocytes Release Neurotoxins After Ischemic and Traumatic Injury To the Central-nervous-system. *Journal of Neuroscience Research*, 36(6), pp.681–693.

He, W. et al., 2007. A Novel Anti-inflammatory Surface for Neural Electrodes. *Advanced Materials*, 19(21), pp.3529–3533.

He, W., McConnell, G.C. & Bellamkonda, R. V, 2006. Nanoscale laminin coating modulates cortical scarring response around implanted silicon microelectrode arrays. *Journal of Neural Engineering*, 3(4), pp.316–326.

Hochberg, L.R. et al., 2006. Neuronal ensemble control of prosthetic devices by a human with tetraplegia. *Nature*, 442(7099), pp.164–171.

Hochberg, L.R. et al., 2012. Reach and grasp by people with tetraplegia using a neurally controlled robotic arm. *Nature*, 485(7398), pp.372–375.

Jeon, M. et al., 2014. Partially flexible MEMS neural probe composed of polyimide and sucrose gel for reducing brain damage during and after implantation. *Journal of Micromechanics and Microengineering*, 24(2), p.25010.

Johnson, M.D., Kao, O.E. & Kipke, D.R., 2007. Spatiotemporal pH dynamics following insertion of neural microelectrode arrays. *Journal of Neuroscience Methods*, 160(2), pp.276–287.

Karumbaiah, L. et al., 2013. Relationship between intracortical electrode design and chronic recording function. *Biomaterials*, 34(33), pp.8061–8074.

Kaufman, M.T. et al., 2010. Roles of Monkey Premotor Neuron Classes in Movement Preparation and Execution. *Journal of Neurophysiology*, 104(2), pp.799–810.

Kolarcik, C.L. et al., 2015. Evaluation of poly(3,4-ethylenedioxythiophene)/carbon nanotube neural electrode coatings for stimulation in the dorsal root ganglion. *Journal of Neural Engineering*, 12(1), p.16008.

Kozai, T.D.Y. et al., 2014. Effects of caspase-1 knockout on chronic neural recording quality and longevity: Insight into cellular and molecular mechanisms of the reactive tissue response. *Biomaterials*, 35(34), pp.9255–9268.

Kozai, T.D.Y., Vazquez, A.L., et al., 2012. In vivo two-photon microscopy reveals immediate microglial reaction to implantation of microelectrode through extension of processes. *Journal of Neural Engineering*, 9(6), p.66001.

Kozai, T.D.Y. et al., 2010. Reduction of neurovascular damage resulting from microelectrode insertion into the cerebral cortex using in vivo two-photon mapping. *Journal of Neural Engineering*, 7(4), p.46011.

Kozai, T.D.Y., Langhals, N.B., et al., 2012. Ultrasmall implantable composite microelectrodes with bioactive surfaces for chronic neural interfaces. *Nature Materials*, 11(12), pp.1065–1073.

Kuo, J.T.W. et al., 2013. Novel flexible Parylene neural probe with 3D sheath structure for enhancing tissue integration. *Lab On A Chip*, 13, pp.554–561.

Lai, H.-Y. et al., 2012. Design, simulation and experimental validation of a novel flexible neural probe for deep brain stimulation and multichannel recording. *Journal of Neural Engineering*, 9(3), p.36001.

Lecas, J.C. et al., 1986. Changes in neuronal activity of the monkey precentral cortex during preparation for movement. *Journal of Neurophysiology*, 56(6), pp.1680–1702.

Liu, X. et al., 1999. Stability of the interface between neural tissue and chronically implanted intracortical microelectrodes. *IEEE Transactions on Rehabilitation Engineering*, 7(3), pp.315–326.

McConnell, G.C. et al., 2009. Implanted neural electrodes cause chronic, local inflammation that is correlated with local neurodegeneration. *Journal of Neural Engineering*, 6(5), p.56003.

Mercanzini, A. et al., 2008. Demonstration of cortical recording using novel flexible polymer neural probes. *Sensors and Actuators A: Physical*, 143(1), pp.90–96.

Moffitt, M.A. & McIntyre, C.C., 2005. Model-based analysis of cortical recording with silicon microelectrodes. *Clinical Neurophysiology*, 116(9), pp.2240–2250.

Najafi, K., Wise, K.D. & Mochizuki, T., 1985. A high-yield IC-compatible multichannel recording array. *IEEE Transactions on Electron Devices*, 32(7), pp.1206–1211.

Nicolelis, M.A.L. et al., 2003. Chronic, multisite, multielectrode recordings in macaque monkeys. *Proceedings of the National Academy of Sciences*, 100(19), pp.11041–11046.

Nordhausen, C.T., Maynard, E.M. & Normann, R.A., 1996. Single unit recording capabilities of a 100 microelectrode array. *Brain Research*, 726(1-2), pp.129–140.

Nunamaker, E.A. & Kipke, D.R., 2010. An alginate hydrogel dura mater replacement for use with intracortical electrodes. *Journal of Biomedical Materials Research Part B: Applied Biomaterials*, 95B(2), pp.421–429.

O'Keefe, J. & Speakman, A., 1987. Single unit activity in the rat hippocampus during a spatial memory task. *Experimental Brain Research*, 68(1), pp.1–27.

Paxinos, G. & Watson, C., 2007. *The Rat Brain in Stereotaxic Coordinates*, Academic Press.

Polikov, V.S., Tresco, P.A. & Reichert, W.M., 2005. Response of brain tissue to chronically implanted neural electrodes. *Journal of Neuroscience Methods*, 148(1), pp.1–18.

Potter, K.A. et al., 2012. Stab injury and device implantation within the brain results in inversely multiphasic neuroinflammatory and neurodegenerative responses. *Journal of Neural Engineering*, 9(4), p.46020.

Purcell, E.K. et al., 2009. In vivo evaluation of a neural stem cell-seeded prosthesis. *Journal of Neural Engineering*, 6(2), p.26005.

Rennaker, R.L., Street, S., et al., 2005. A comparison of chronic multi-channel cortical implantation techniques: manual versus mechanical insertion. *Journal of Neuroscience Methods*, 142(2), pp.169–176.

Rennaker, R.L., Ruyle, A.M., et al., 2005. An economical multi-channel cortical electrode array for extended periods of recording during behavior. *Journal of Neuroscience Methods*, 142(1), pp.97–105.

Rousche, P. & Normann, R., 1992. A method for pneumatically inserting an array of penetrating electrodes into cortical tissue. *Annals of Biomedical Engineering*, 20(4), pp.413–422.

Rousche, P.J. et al., 2001. Flexible polyimide-based intracortical electrode arrays with bioactive capability. *IEEE Transactions on Biomedical Engineering*, 48(3), pp.361–371.

Rousche, P.J. & Normann, R.A., 1998. Chronic recording capability of the Utah Intracortical Electrode Array in cat sensory cortex. *Journal of Neuroscience Methods*, 82(1), pp.1–15.

Sankar, V. et al., 2013. A highly compliant serpentine shaped polyimide interconnect for front-end strain relief in chronic neural implants. *Frontiers in Neurology*, 4(124), pp.1–11.

Sawyer, A.J. et al., 2014. The effect of inflammatory cell-derived MCP-1 loss on neuronal survival during chronic neuroinflammation. *Biomaterials*, 35(25), pp.6698–6706.

Saxena, T. et al., 2013. The impact of chronic blood-brain barrier breach on intracortical electrode function. *Biomaterials*, 34(20), pp.4703–4713.

Schmidt, S., Horch, K. & Normann, R., 1993. Biocompatibility of Silicon-based Electrode Arrays Implanted In Feline Cortical Tissue. *Journal of Biomedical Materials Research*, 27(11), pp.1393–1399.

Schwartz, A.B. et al., 2006. Brain-Controlled Interfaces: Movement Restoration with Neural Prosthetics. *Neuron*, 52(1), pp.205–220.

Seymour, J.P. & Kipke, D.R., 2006. Fabrication of polymer neural probes with sub-cellular features for reduced tissue encapsulation. *2006 Annual International Conference of the IEEE Engineering In Medicine and Biology Society*, 1, pp.4606–4609.

Seymour, J.P. & Kipke, D.R., 2007. Neural probe design for reduced tissue encapsulation in CNS. *Biomaterials*, 28(25), pp.3594–3607.

Simeral, J.D. et al., 2011. Neural control of cursor trajectory and click by a human with tetraplegia 1000 days after implant of an intracortical microelectrode array. *Journal of Neural Engineering*, 8(2), p.25027.

Skousen, J.L. et al., 2011. Reducing surface area while maintaining implant penetrating profile lowers the brain foreign body response to chronically implanted planar silicon microelectrode arrays. *Progress in Brain Research*, 194, pp.167–180.

Stice, P. et al., 2007. Thin microelectrodes reduce GFAP expression in the implant site in rodent somatosensory cortex. *Journal of Neural Engineering*, 4(2), p.42.

Szarowski, D.H. et al., 2003. Brain responses to micro-machined silicon devices. *Brain Research*, 983(1-2), pp.23–35.

Takeuchi, S. et al., 2005. Parylene flexible neural probes integrated with microfluidic channels. *Lab*, 5, pp.519–523.

Taylor, D.M., Tillery, S.I.H. & Schwartz, A.B., 2003. Information conveyed through brain-control: cursor versus robot. *IEEE Transactions on Neural Systems and Rehabilitation Engineering*, 11(2), pp.195–199.

Turner, J.N. et al., 1999. Cerebral Astrocyte Response to Micromachined Silicon Implants. *Experimental Neurology*, 156(1), pp.33–49.

Velliste, M. et al., 2008. Cortical control of a prosthetic arm for self-feeding. *Nature*, 453(7198), pp.1098–1101.

Vetter, R.J. et al., 2005. Development of a Microscale Implantable Neural Interface (MINI) Probe System. *2005 Annual International Conference of the IEEE Engineering In Medicine and Biology Society*, 7, pp.7341–7344.

Williams, J.C., Rennaker, R.L. & Kipke, D.R., 1999. Long-term neural recording characteristics of wire microelectrode arrays implanted in cerebral cortex. *Brain Research Protocols*, 4(3), pp.303–313.

Winslow, B.D. & Tresco, P.A., 2010. Quantitative analysis of the tissue response to chronically implanted microwire electrodes in rat cortex. *Biomaterials*, 31(7), pp.1558–1567.

Xiang, Z. et al., 2014. Ultra-thin flexible polyimide neural probe embedded in a dissolvable maltose-coated microneedle. *Journal of Micromechanics and Microengineering*, 24(6), p.65015.

Zhong, Y. & Bellamkonda, R. V, 2007. Dexamethasone-coated neural probes elicit attenuated inflammatory response and neuronal loss compared to uncoated neural probes. *Brain Research*, 1148(0), pp.15–27.

CHAPTER IV

Chronic *In Vivo* Stability Assessment of Carbon Fiber Microelectrode Arrays

4.1 Abstract

Objective. Individual flexible carbon fiber microelectrodes can record unit activity in both acute and semi-chronic (~1 month) implants. Additionally, new methods have been developed to insert a 16 channel array of carbon fiber microelectrodes. Before assessing the *in vivo* long-term viability of these arrays, accelerated soak tests were carried out to determine the most stable site coating material. Next, a multi-animal, multi-month, chronic implantation study was carried out with carbon fiber microelectrode arrays and standard silicon electrodes serving as a control. *Approach.* Carbon fibers were first functionalized with one of two different formulations of PEDOT and subjected to accelerated aging in a heated water bath. After determining the best PEDOT formula to use, fully functionalized high-density carbon fiber arrays were chronically implanted in rat motor cortex. Some rodents were also implanted with a single silicon electrode in the motor cortex, while other animals received both implants, one in each hemisphere's motor cortex. Impedance and electrophysiology measurements were taken regularly post-implant. *Main results.* Results from electrophysiology recordings show the carbon fibers detecting unit activity for at least 3 months with average amplitudes of

approximately 200 μV. The chronically implanted silicon electrodes detected very few units, with average amplitudes between 50 – 100 μV. In addition, units detected on the carbon fibers had an average SNR that held steady at 4 for the first three months. Lastly, a noise analysis was conducted for each probe type. While the carbon fibers displayed a higher overall noise floor, this was readily accounted for by a larger biological component which indicates a healthier local tissue environment and is further corroborated by detected unit activity. *Significance*. This study has validated the use of carbon fiber microelectrode arrays as a chronic neural recording technology. These electrodes have demonstrated the ability to detect quality single units with high amplitude and SNR values over a 3 month period, and show the potential to record for even longer time periods.

4.2 Introduction

Recording stable, low-noise, high-amplitude unit activity in the motor cortex is crucial for the long-term stability of any brain machine interface (BMI) system (Carmena et al. 2003; Simeral et al. 2011; Hochberg et al. 2006; Chestek et al. 2011; Collinger et al. 2013; Velliste et al. 2008; Hochberg et al. 2012; Taylor et al. 2003; Schwartz et al. 2006) and can be equally important in many neuroscience studies (Davidson et al. 2009; Cohen et al. 2012; Berke et al. 2009; Xie et al. 2014; Royer et al. 2010). To accomplish this goal, a system of electrodes should ideally illicit little to no immune response, have the capacity to concurrently record from a large population of neurons to either access more information content or to better understand local population dynamics, and demonstrate the ability to chronically record neural activity.

One approach to reduce the immune response typically caused by recording electrodes is to create a better mechanical match between the Young's moduli of the brain and the implanted electrodes. While no material has been able to reach the extremely low Young's modulus of the brain, 3 – 5 kPa (Subbaroyan et al. 2005; Gefen et al. 2003), many groups have designed, tested, and acutely validated neural probes using materials with a Young's modulus that approaches that of the brain (Rousche et al. 2001; Mercanzini et al. 2008; Lai et al. 2012; Sankar et al. 2013; Xiang et al. 2014; Jeon et al. 2014; Cheung et al. 2007; Kim et al. 2013; Kuo et al. 2013; Takeuchi et al. 2005; Ware et al. 2012; Ware et al. 2014). These electrodes can be very large, which is necessary to penetrate and overcome the brain's critical buckling force (Najafi & Hetke 1990; Wester et al. 2009; Harris et al. 2011), but this can also lead to even more damage, negating any possible benefit of such a soft probe. Unfortunately, many of these designs have not demonstrated the ability to achieve high channel counts and - more importantly - they have not been validated in chronic animal implants.

The most widely adopted approach to achieving high channel counts in electrodes has been through the use of micromachined neural probes. In this field, there are two primary designs. The first utilizes multiple individual shanks of a conductive material with an exposed electrode site at the tip of each shank, such as microwires (Cheung 2007; Gray et al. 1995; Nicolelis et al. 2003; Williams et al. 1999; Rennaker et al. 2005; Prasad et al. 2014) or the Utah array (Nordhausen et al. 1996; Campbell et al. 1991). The second group of electrodes utilizes a planar structure such as the Michigan probe (Wise & Angell 1975; Najafi et al. 1985; Wise et al. 2004; Vetter et al. 2005), where multiple electrodes sites are incorporated along the length of the device.

While both styles of technology have been shown to work chronically, they have been unable to miniaturize both width and thickness to a sub-cellular level. Decreasing the size of the electrode would improve both channel density and therefore, channel counts, as well reduce local tissue inflammation (Seymour & Kipke 2007; Stice et al. 2007; Skousen et al. 2011), preserving the local circuity being investigated. A reduced probe footprint has been shown to lessen the long-term glial response and improve the survival rates of the local neuronal population (Seymour & Kipke 2007; Stice et al. 2007; Skousen et al. 2011). It should be noted that these studies demonstrating an improved tissue response made use of hard materials, such as silicon (Stice et al. 2007; Skousen et al. 2011), and softer materials, such as SU-8 & parylene (Seymour & Kipke 2007). While an electrode's material properties may play an important role in bridging the mechanical mismatch between an implant and the brain, the previous studies on electrode dimensions point to probe size as being a more critical factor.

We have recently proposed a multi-electrode array design using carbon fibers as the basis for the recording electrode (Kozai et al. 2012; Patel et al. 2015). Carbon fiber electrodes are small (d = 6.8 μm), and with the addition of a parylene-c insulating coating (t = 800 nm), the overall diameter is only increased to 8.4 μm. This critical dimension is well below of that all probe technologies that have been demonstrated *in vivo*. In addition, this electrode material is extremely amenable to creating high density arrays and with a site coating of poly(3,4-ethylenedioxythiophene) (PEDOT) has been shown to record high quality unit activity (Ludwig et al. 2006; Kozai et al. 2012; Venkatraman et al. 2011).

This work first evaluates two different formulations of the site coating material, PEDOT, using an accelerated aging test. Carbon fiber arrays functionalized with parylene-c and PEDOT were chronically implanted into the rat motor cortex of one hemisphere. Additionally, some animals were implanted with a commercially available planar silicon electrode in the contralateral hemisphere's motor cortex. Impedance and electrophysiology recordings were taken on a regular basis and analyzed to demonstrate the carbon fiber's viability as a chronic electrode technology.

4.3 Materials & Methods

4.3.1 Soak Test Probe Assembly

Printed circuit boards were first roughened in the non-trace and non-bond pad areas with a Dremel tool, to allow for better adherence of the final epoxy coating (figure 4.1(a)). Once roughened, eight individual carbon fibers (T-650/35 3K, Cytec Thornel, Woodland Park, NJ), with length of approximately 1 cm, were placed on the individual bond pads using conductive silver epoxy (H20E, Epoxy Technology, Billerica, MA) (figure 4.1(b)). The conductive epoxy was then oven cured using the manufacturer's recommended settings. The silver epoxy bond was then covered with insulating epoxy (353NDT, Epoxy Technology, Billerica, MA) and oven cured using the manufacturer's recommended settings (figure 4.1(c)).

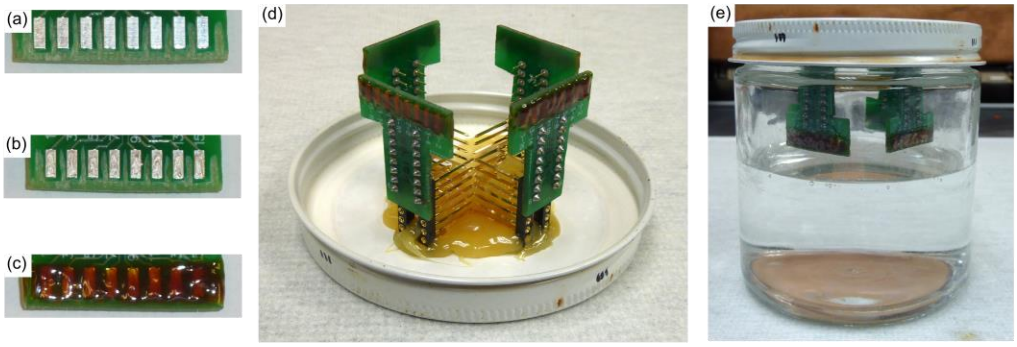

Figure 4.1. Soak test probe assembly and setup. (a) Areas between and surrounding the bond pads have been roughened. (b) Silver epoxy on each bond pad for the carbon fibers. (c) Exposed bond pads with carbon fibers are covered with insulating epoxy. (d) Four PCBs with functionalized fibers are secured to the underside of the soak jar's lid. (e) Lids are secured to jars containing 1x PBS. Jars are then placed in a heated water bath.

Probes were then insulated with a conformal coating of parylene-c (t=800 nm) using a Parylene Deposition System 2010 (SCS Coatings, Indianapolis, IN). After insulation, the tips of each probe were cut to re-expose a bare carbon fiber site. At this site, one of two solutions (see section 4.4.1) was electrodeposited. The first was a solution of 0.01 M 3,4-ethylenedioxythiophene (483028, Sigma-Aldrich, St. Louis, MO):0.1 M sodium p-toluenesulfonate (152536, Sigma-Aldrich, St. Louis, MO). The second solution was composed of 0.01 M 3,4-ethylenedioxythiophene (483028, Sigma-Aldrich, St. Louis, MO):0.1 M polystyrene sulfonate (222271000, Acros, NJ). For each solution the electrodeposition was carried out by applying 100 pA/channel for 600 seconds to form a layer of poly(3,4-ethylenedioxythiophene):sodium p-toluenesulfonate (PEDOT:pTS) or poly(3,4-ethylenedioxythiophene):polystyrene sulfonate (PEDOT:PSS). All channels to be coated with a given solution were shorted together during the electrodeposition step and the current delivered was scaled accordingly.

4.3.2 Accelerated Soak Test Setup

Boards with parylene-c and PEDOT:pTS or PEDOT:PSS coated carbon fibers were mounted to the underside of a jar lid (figure 4.1(d)). The lids were then secured to jars that contained 1x phosphate buffered saline (PBS) solution (BP3994, Fisher, Waltham, MA) (figure 4.1(e)). The 1x PBS was at a level such that only the fibers were submerged and not the entire printed circuit board. The jars were then lowered into a water bath maintained at 60 °C. At each time point the fibers were removed from the heated 1x PBS and rinsed once with deionized water. Next, the impedance of the fibers was recorded. Once recordings were complete the assembly was returned to the heated 1x PBS.

According to works by Green et al. (Green et al. 2012) & Hukins et al. (Hukins et al. 2008), equation (4.1) can be used to determine simulated aging time that the fibers have undergone:

$$t_{37} = t_T \times Q10^{(T-37)/10} \tag{4.1}$$

Where t_{37} is the simulated aging time at 37 °C, t_T is the amount of real time that the samples have been kept at the elevated temperature, T, and Q10 is an aging factor that is equal to 2, according to ATSM guidelines for polymer aging (ATSM 2011). Calculating the simulated time for t_T = 1 and T = 60 °C results in t_{37} = 4.92. This value of 4.92 is the acceleration factor and all real time measurements are scaled by this amount to obtain the simulated time.

4.3.3 Electrochemical Impedance Spectroscopy (EIS)

EIS measurements were taken with a PGSTAT12 Autolab (EcoChemie, Utrecht, Netherlands), controlled by vendor-supplied NOVA software. Measurements were

obtained by applying a 10 mV_{RMS} signal from 10 Hz to 31 kHz. Custom Matlab (Mathworks, Natick, MA) scripts were used to determine frequency specific impedance values. All reported values are mean ± standard error of the mean.

4.3.4 Statistical Analysis

A one-sided t-test was used to determine if the 1 kHz impedance of the PEDOT:pTS coated fibers was significantly less than that of the PEDOT:PSS coated fibers. All calculations were carried out using R 3.0.2 (http://www.r-project.org/).

4.3.5 Carbon Fiber Array Preparation for Chronic Implants

Carbon fiber arrays were fabricated as described in section 2.3.1.1. Once fully assembled, all carbon fiber arrays for neural recordings were coated with an 800 nm thick insulating layer of parylene-c using a Parylene Deposition System 2010 (SCS Coatings, Indianapolis, IN). Probe tips also received a site coating of PEDOT:pTS with the same formula and deposition parameters used on the fibers that underwent soak testing. The final preparation step was a coating of poly(ethylene glycol) (PEG) as described in section 2.3.2.1.

4.3.6 Surgery for Chronic Implantation of Carbon Fibers and Silicon Probes

Surgical implantation of the carbon fiber arrays and silicon electrodes (A1x16-3mm-50-177-HZ16_21mm, site size 177 μm^2, NeuroNexus Technologies, Ann Arbor, MI) was carried out using methods described in section 3.3.2. A detailed breakdown of each animal's implant(s) and implant depth can be found in table 4.1.

4.3.7 Electrophysiology Recordings and Spike Sorting

Electrophysiology recordings using chronic implants of carbon fiber arrays and silicon probes were done while the rats were awake and moving about freely in their cage. All acquisition of electrophysiology recordings were taken using a ZC16 headstage, RA16PA pre-amplifier, and RX5 Pentusa base station (Tucker-Davis Technologies, Alachua, FL). During data acquisition, the pre-amplifier high pass filtered at 2.2 Hz, anti-aliased filtered at 7.5 kHz, and sampled at a rate of ~25 kHz. Each recording session lasted 5 or 10 minutes.

Recording sessions were imported into Offline Sorter (Plexon, Dallas, TX) and first high-pass filtered (250 Hz corner, 4^{th} order Butterworth). Each channel was manually thresholded and the resultant waveforms sorted by a trained operator. Sorted waveforms belonging to the same neuronal unit were averaged together to obtain a peak-to-peak amplitude for that unit, which was averaged with all other unit peak-to-peak amplitude values to obtain the mean value for each recording day for each probe type. All reported values are mean ± standard error of the mean.

4.3.8 Noise Floor, Thermal Noise, and Signal-to-Noise Ratio Calculations

To determine the noise floor for each recording channel, a trained operator picked out five 100 ms snippets of filtered electrophysiology recording data that did not contain sorted units and did not display amplifier saturation indicative of a motion artifact. The snippets of data were then joined together in a single 500 ms block which was used to calculate $V_{RMS\text{-}Channel}$. The signal-to-noise ratio (SNR) of each sorted unit was calculated by dividing the peak-to-peak voltage of the waveform by $3 \cdot V_{RMS\text{-}Channel}$.

To calculate thermal noise, first the power spectral density (PSD) at each frequency between 250 Hz and 7.8 kHz was calculated using the following equation:

$$V_{PSD}^2 = 4kTRe(Z(f)) \quad (4.2)$$

Where k = Boltzman's constant, T = absolute temperate, $Re(Z(f))$ = real component of impedance at the given frequency, f (Ludwig et al. 2006; Lempka et al. 2011; Lempka et al. 2006). Frequency range was determined by the high-pass corner set during data processing and the low-pass corner set by the recording equipment. As there was no impedance measurement taken at the low-pass corner of 7.5 kHz, the next closest value was used. Body temperature was set to 310 K. To calculate the root mean square of the thermal noise, the following integration took place between the frequency band of interest:

$$V_{RMS-Thermal\ noise} = \sqrt{\int_{f_{low}}^{f_{high}} V_{PSD}^2 df} \quad (4.3)$$

All reported noise and SNR values are mean ± standard error of the mean.

4.3.9 Channel Exclusion Criterion

It was discovered throughout the study that certain carbon fiber channels showed signs of breakage, mostly likely at the point where the fibers initially extended off of the PCB. To prevent these channels from skewing the analysis, an elimination criterion was created. If a recording channel's 10 Hz impedance magnitude closely matched that of a known broken channel on the same device, for three consecutive days, the channel was removed from the study from that point onwards.

In addition, there were instances where impedance values were taken incorrectly and not discovered until later. In these cases, impedance values indicated an open circuit

at every channel and were removed; however, the recorded electrophysiology data from the same day, which used a different headstage connector, remained in the study.

Lastly, at one point in the study it was noticed that the headstage used to record electrophysiology from the silicon electrodes was partially damaged. To ensure the fidelity of the data analysis, all data from those damaged channels (8 of 16 for the entirety of ZIF_CF_R19's implant and for the first 23 days of ZIF_CF_R22's implant) were removed. The remaining good sites were kept and analyzed. In addition, once the silicon electrode's headstage was repaired all channels were again included in the study.

The number of channels used for impedance analysis at each time point can be seen in appendix figure B.1. The number of channels used for calculating the percentage of channels with units and the noise levels at each time point can be seen in appendix figure B.2. The number of units detected used for amplitude analysis at each time point can be seen in appendix figure B.3.

4.3.10 SEM Imaging

A FEI Nova 200 Nanolab Focused Ion Beam Workstation and Scanning Electron Microscope (FEI, Hillsboro, OR) was used for SEM imaging. Prior to imaging, samples were gold sputter coated with a SPI-Module Sputter Coater (SPI Supplies, West Chester, PA).

Animal Name	Carbon Fiber Depth	Silicon Probe Depth	Days in study
ZIF_CF_R16	1.56 mm	No Implant	154
ZIF_CF_R17	1.505 mm	No Implant	154
ZIF_CF_R18	1.505 mm	No Implant	91
ZIF_CF_R19	1.495 mm	1.45 mm	91
ZIF_CF_R22	1.45 mm	1.45 mm	73
ZIF_CF_R28	No Implant	1.5 mm	31
ZIF_CF_R29	No Implant	1.5 mm	31
ZIF_CF_R30	No Implant	1.5 mm	31

Table 4.1. Animal implant information. Probe implant depth and duration for each animal.

4.4 Results

4.4.1 Accelerated Soak Test

Previous work has shown that parylene-c coated carbon fibers with only an exposed carbon tip site are unable to record unit activity due to the high site impedance (Kozai et al. 2012). To alleviate this issue, PEDOT:PSS was electrodeposited at the tip of each site which greatly reduced the site impedance (Kozai et al. 2012; Cui & Martin 2003). Recent studies by Green et al. have demonstrated that other formulations of PEDOT are more stable over time when compared to PEDOT:PSS (Green et al. 2012; Harris et al. 2013). To determine the best site coating for the carbon fiber electrodes, an accelerated soak test was carried out between the original PEDOT:PSS (n=8 fibers) formulation and a different formulation, PEDOT:pTS (n=23 fibers) (Green et al. 2012). In addition to determining the best site coating, the values from this study will establish a baseline which can be compared to later chronic animal implants.

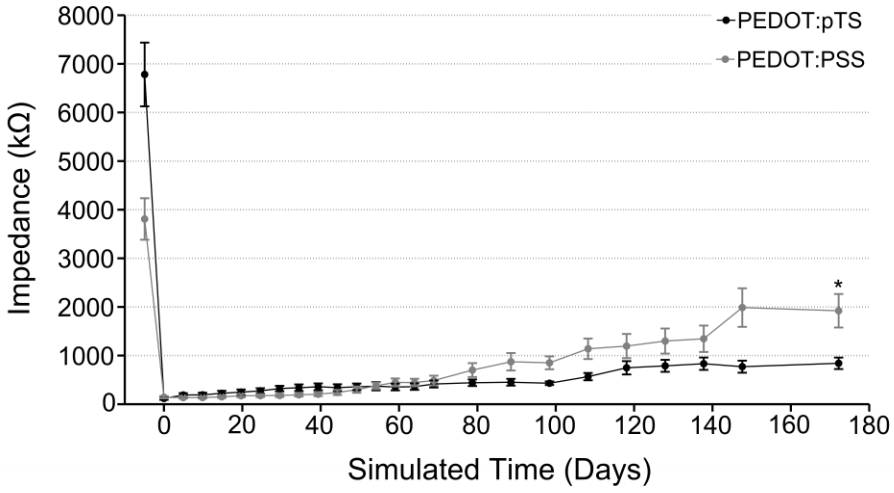

Figure 4.2. PEDOT soak test. Impedance values (mean ± standard error of the mean) at 1 kHz for PEDOT:PSS and PEDOT:pTS coated carbon fiber electrodes over the simulated time from the accelerated soak test. * indicates significance at $p<0.01$.

At day 0, when the initial PEDOT depositions took place, both sets of impedance values at 1 kHz (PEDOT:PSS 142.79 ± 23.24 kΩ & PEDOT:pTS 117.89 ± 28.35 kΩ) were similar (figure 4.2). As time progressed the average impedance of the PEDOT:PSS coated fibers increased faster than those coated with PEDOT:pTS. On the final day of testing the fibers coated with PEDOT:PSS had a significantly higher impedance of 1921.44 ± 344.51 kΩ while the PEDOT:pTS fibers had an impedance of 840.46 ± 117.69 kΩ. During the repeated measurements carried out over the course of 35 days, one PEDOT:PSS coated fiber and three PEDOT:pTS coated fibers were accidentally broken off of the test boards, which resulted in lower sample sizes over the duration of the study.

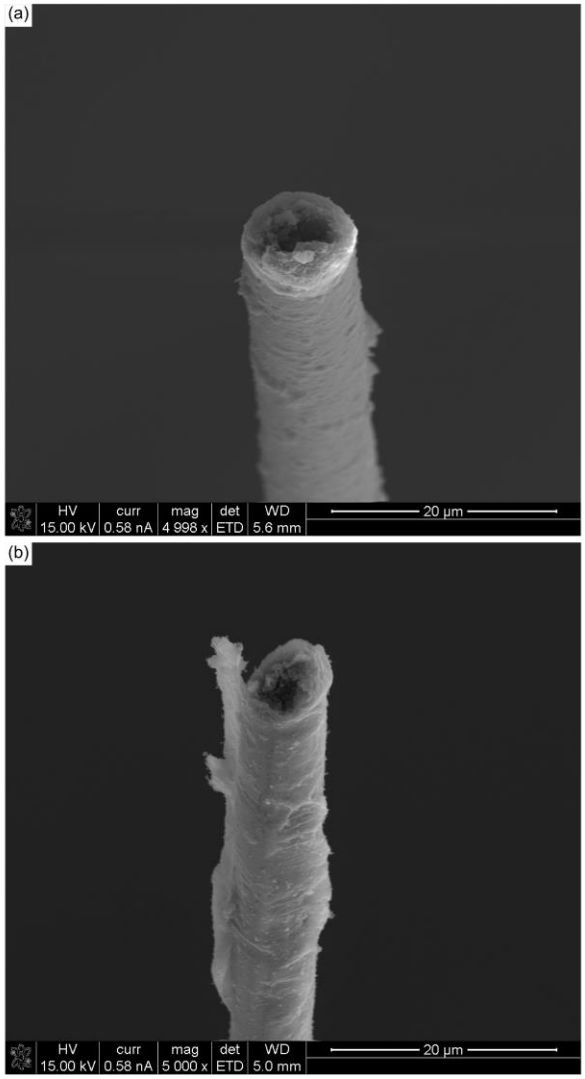

Figure 4.3. SEM images of PEDOT coated and soak tested fibers. (a) SEM image of a PEDOT:pTS coated carbon fiber aged to simulated day 172.2 showing PEDOT still at the tip, but with a possible void or loss of PEDOT:pTS in the center. (b) SEM image of a PEDOT:PSS coated carbon fiber aged to simulated day 172.2 showing similar properties to that of the PEDOT:pTS coated fiber.

SEM images (figures 4.3(a) and 4.3(b)) show good adherence of both PEDOT formulations to the carbon fiber tip's outer edges. A visible void of PEDOT can be seen in the center of both PEDOT formulations, which may help to explain the steady increases in impedance.

Based on the impedance results, all chronic implants of carbon fibers received a site coating of PEDOT:pTS.

4.4.2 Chronic Implant Impedance

To assess the longevity and viability of the carbon fiber arrays, 5 Long Evans rats were implanted chronically with carbon fiber arrays (n=60 fibers) in the right motor cortex. Two of those rats were also implanted with silicon electrodes (n=2 electrodes with 16 sites each) in the left motor cortex. In addition, 3 more rats were implanted with only silicon electrodes (n=3 electrodes with 16 sites each). A detailed breakdown of each animal's implant type, duration, and depth, can be found in table 4.1. For all results no differences were noted between animals that received one or both probe types.

Impedance measurements were taken every day for the first 13 days, every other day from days 13 to 31, and then every third day from days 31 to 91. For the two animals continued out to day 154, measurements were taken once a week after day 91. One animal, ZIF_CF_R22, was sacrificed at day 73 for histological and surgical technique evaluations.

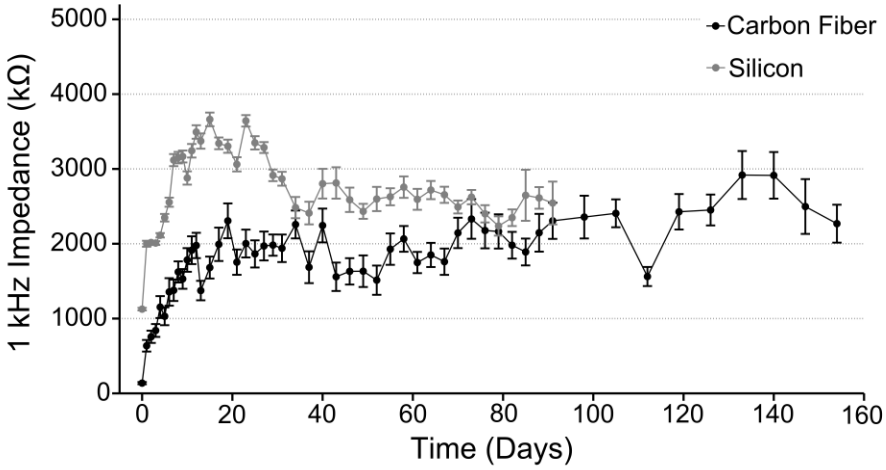

Figure 4.4. Chronic implant impedances. Impedance values (mean ± standard error of the mean) for each probe type across time. Both electrode types saw an approximately 2 MΩ increase in impedance within the first two weeks. Values for the carbon fibers then leveled off while the silicon electrode values dropped before leveling off. The number of channels used for impedance analysis at each time point can be seen in appendix figure B.1.

The pre-implant 1 kHz impedances (figure 4.4) at day 0 for the carbon fibers was 136.43 ± 14.75 kΩ while those of the silicon probes were 1125.54 ± 17.57 kΩ. At day 1, post-implantation impedances for carbon fibers increased to 636.23 ± 77.76 kΩ while the silicon sites also increased to 2000.0 ± 39.94 kΩ. The impedance for both sets of probes continued upward until day 12 for the carbon fibers and day 15 for the silicon probes. At these time points the impedance values were 1976.84 ± 169.59 kΩ for the carbon fibers and 3662.20 ± 91.27 kΩ for the silicon probes.

Following the initial upward increases in impedance, the carbon fiber electrodes saw a leveling off in the impedance values which fluctuated between 1500 – 2500 kΩ from days 11 to 91. The silicon probes saw much greater variability after day 9 with average impedance values ranging from approximately 2000 kΩ to 4000 kΩ. The large variation in average impedance for the silicon probes before and after day 31 is likely due to the drop in electrode sample size after day 31. On the final day of recording, the carbon fiber electrodes had a mean 1 kHz impedance of 2306.57 ± 241.87 kΩ while the silicon probes had a mean 1 kHz impedance of 2544.25 ± 286.35 kΩ.

Two animals, ZIF_CF_R16 & ZIF_CF_R17, were not sacrificed at day 91 and were recorded from for an additional two months. Recordings were taken at one week intervals in this extended period. The carbon fiber electrode impedance values rose slightly during this period and fluctuated between 2000 – 3000 kΩ.

4.4.3 Chronic Unit Activity

Electrophysiology recordings followed the same points as those used for the impedance measurements. On day 1 post-implant, 66.7% of the implanted carbon fiber

electrodes detected unit activity with a mean peak-to-peak amplitude of 133.2 ± 9.5 µV (figures 4.5(a) and 4.5(b)).

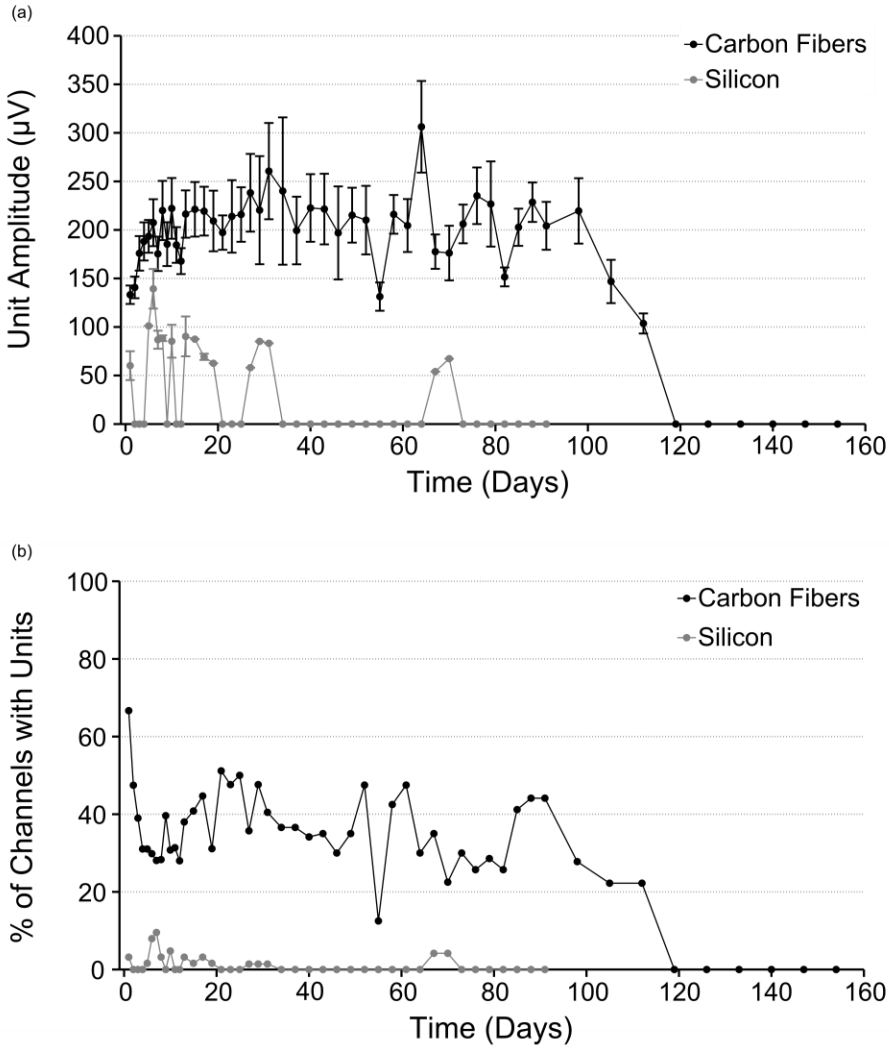

Figure 4.5. Chronic unit amplitudes and percentage of channels with units. (a) Carbon fiber electrodes detected an average unit amplitude of 200 µV across three months. Units detected on silicon electrodes had a mean amplitude of 50 – 100 µV. All values are mean ± standard error of the mean. The number of units detected used for amplitude analysis at each time point can be seen in appendix figure B.3. (b) On average 20% to 40% of viable carbon fiber electrodes detected unit activity across time, while silicon electrodes did so with a peak of 9.5% at day 10 and most other days detecting no unit activity. The number of channels used for calculating the percentage of channels with units at each time point can be seen in appendix figure B.2.

At the same time point the silicon electrodes detected unit activity on 3.17% of the electrodes sites with an average peak-to-peak amplitude of 60.2 ± 14.9 µV. By day 6,

mean unit amplitude on the 29.82% of carbon fiber electrodes with activity continued to climb to 207.5 ± 24.2 μV while the silicon electrodes showed a small climb in activity with 7.94% of electrode sites detecting units with an average peak-to-peak amplitude of 139.3 ± 20.4 μV. At day 13 the number of carbon fiber electrodes with detectable units had increased to 38%, but with an average detected peak-to-peak amplitude that was maintained at 216.4 ± 24.4 μV. During this same period the silicon electrode detection rate remained in the single percentage range and at day 13, 3.17% of electrode sites showed an average peak-to-peak amplitude of 90.3 ± 20.6 μV.

Following this two week post-implant period the carbon fiber electrodes demonstrated mean peak-to-peak unit activity that stayed within the range of 150 – 250 μV through day 91. During this same period the silicon electrodes had a very low detection rate, which was often at 0% for consecutive recording periods. When single units were detected the mean peak-to-peak amplitude was typically between 50 – 100 μV. After day 73, no additional units were detected on the silicon probes. At day 91, 44.12% of the remaining carbon fiber implanted sites were still able to detect units with a mean peak-to-peak amplitude of 204.2 ± 24.7 μV.

The two animals that were carried out to day 154 showed continued unit activity until day 112, with 22.22% of the sites detecting a mean peak-to-peak unit amplitude of 103.6 ± 10.4 μV. After this time point no units were detected across the remaining carbon fiber electrodes.

Filtered snippets of recording data and sorted unit panels for every implanted carbon fiber electrode at days 7, 49, and 91, can be seen in figures 4.6 – 4.11.

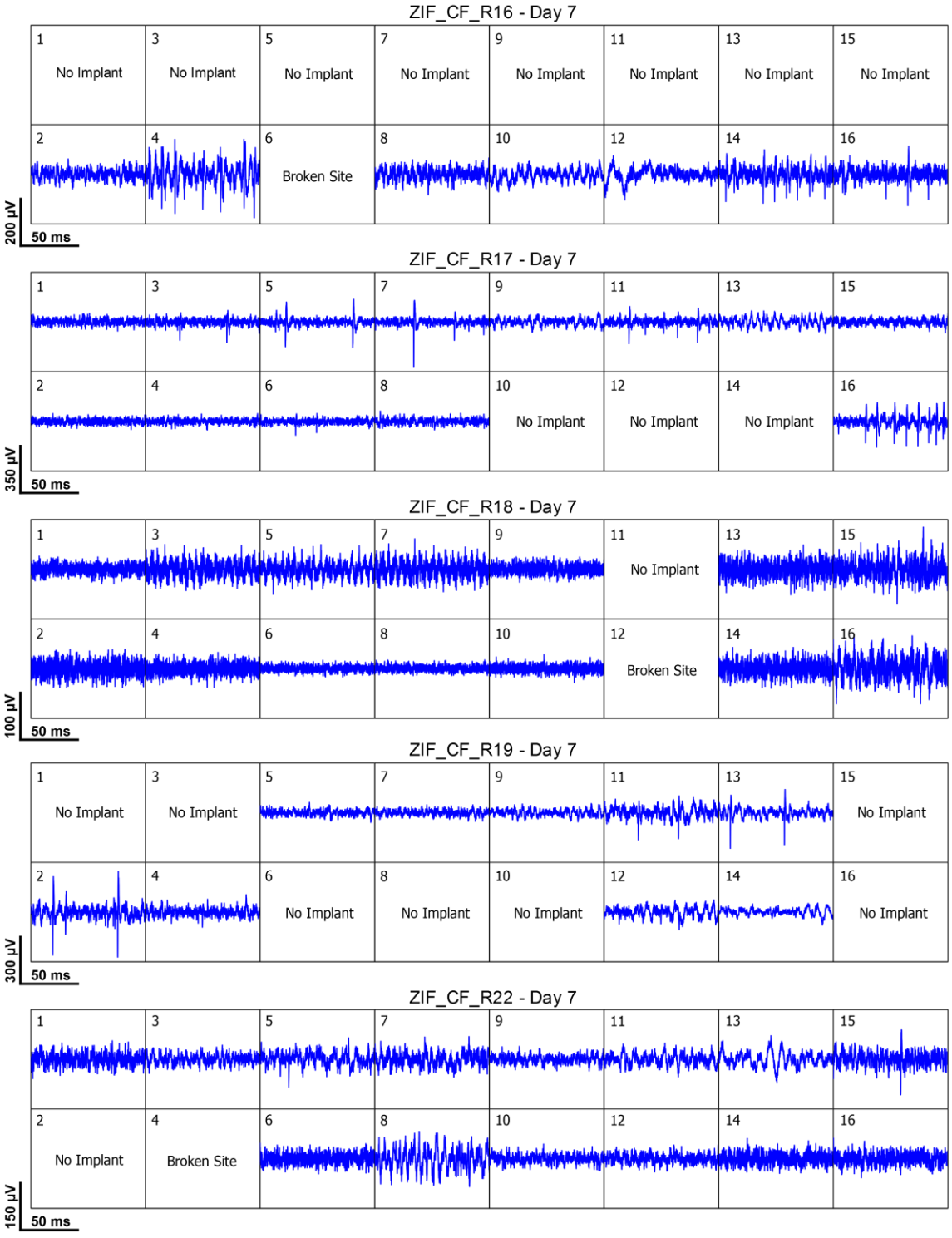

Figure 4.6. Carbon fiber electrode recordings at day 7. Representative filtered (250 Hz corner, 4th order Butterworth, high-pass) recording snippets from each implanted carbon fiber at day 7 post-operatively.

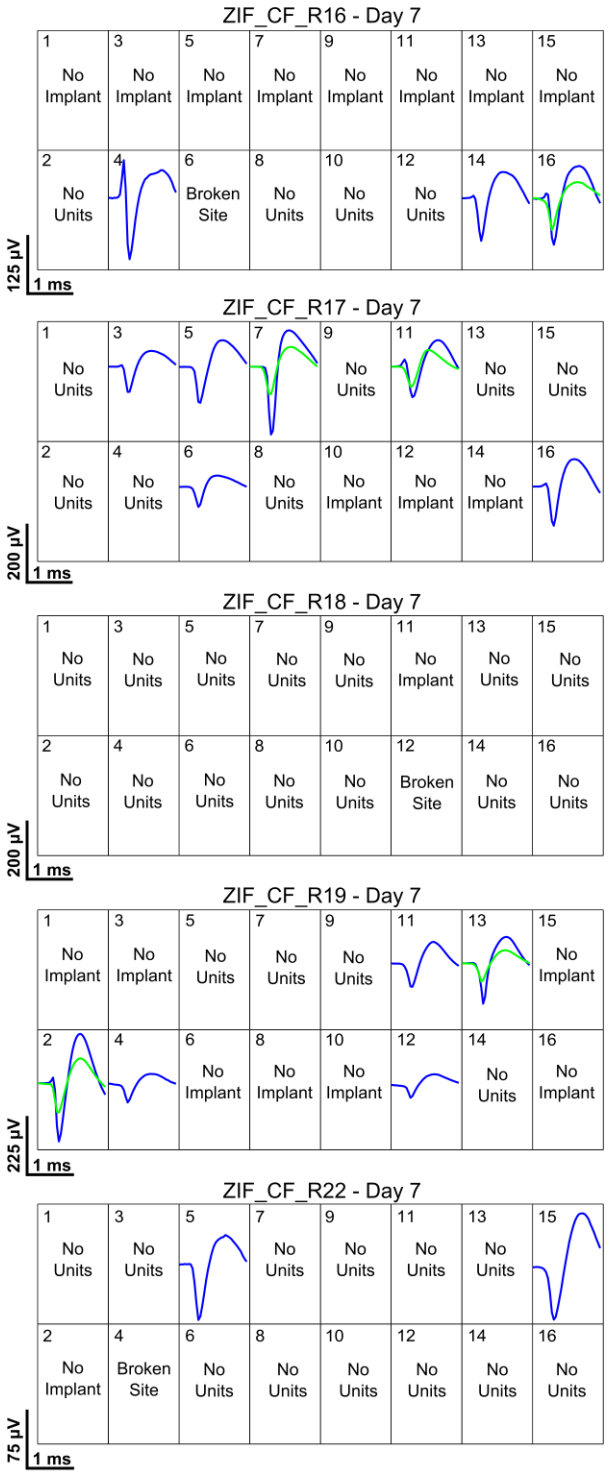

Figure 4.7. Carbon fiber electrode unit activity at day 7. Average waveforms of sorted units detected on each implanted carbon fiber at day 7 post-operatively.

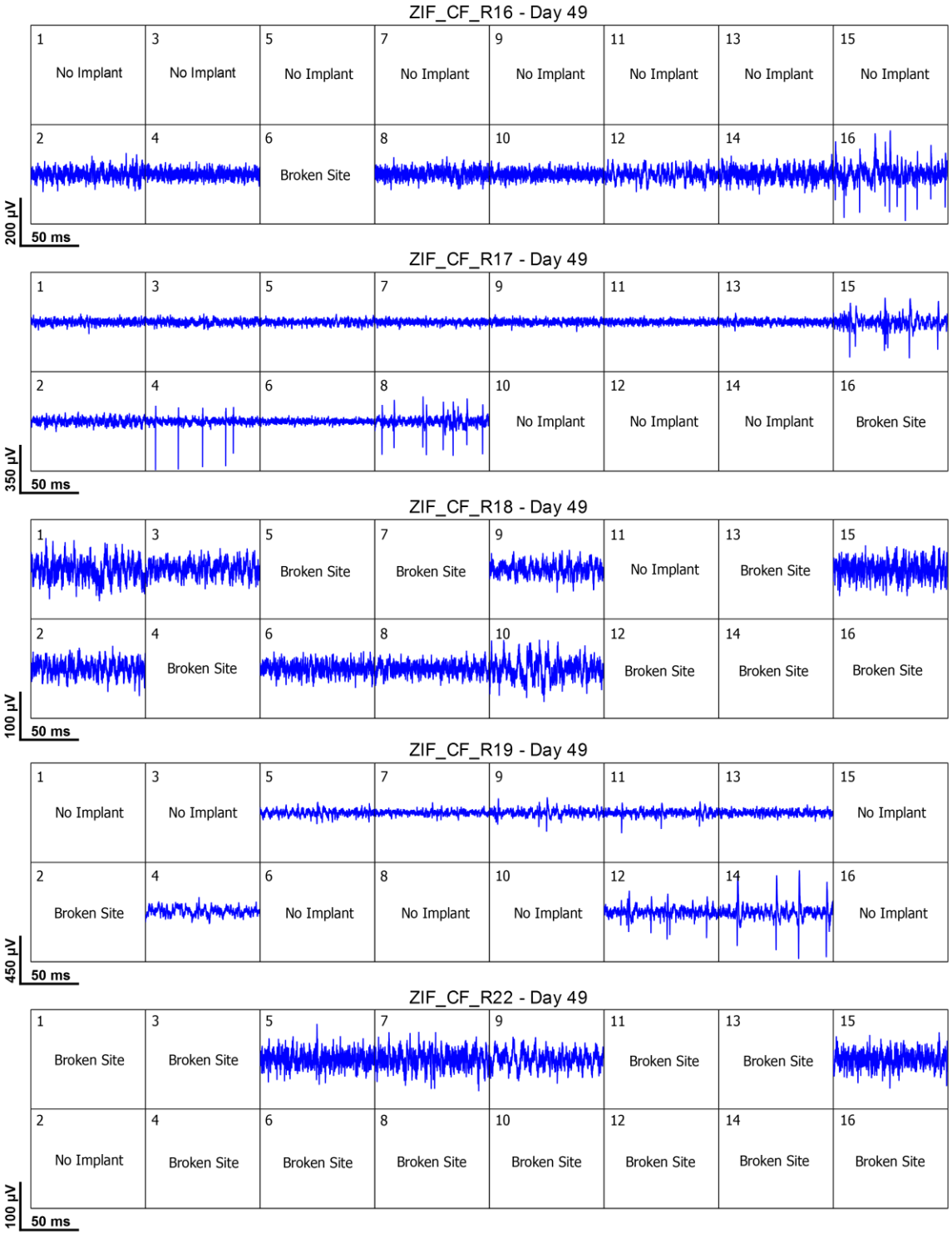

Figure 4.8. Carbon fiber electrode recordings at day 49. Representative filtered (250 Hz corner, 4th order Butterworth, high-pass) recording snippets from each implanted carbon fiber at day 49 post-operatively.

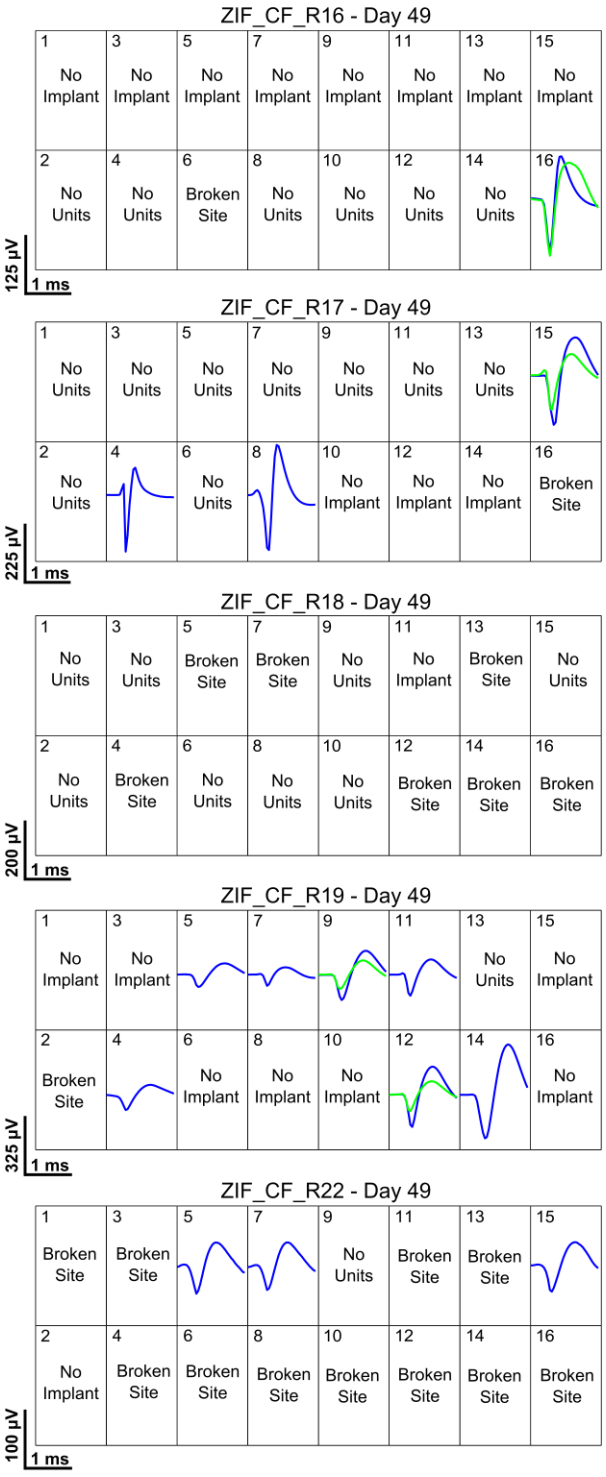

Figure 4.9. Carbon fiber electrode unit activity at day 49. Average waveforms of sorted units detected on each implanted carbon fiber at day 49 post-operatively.

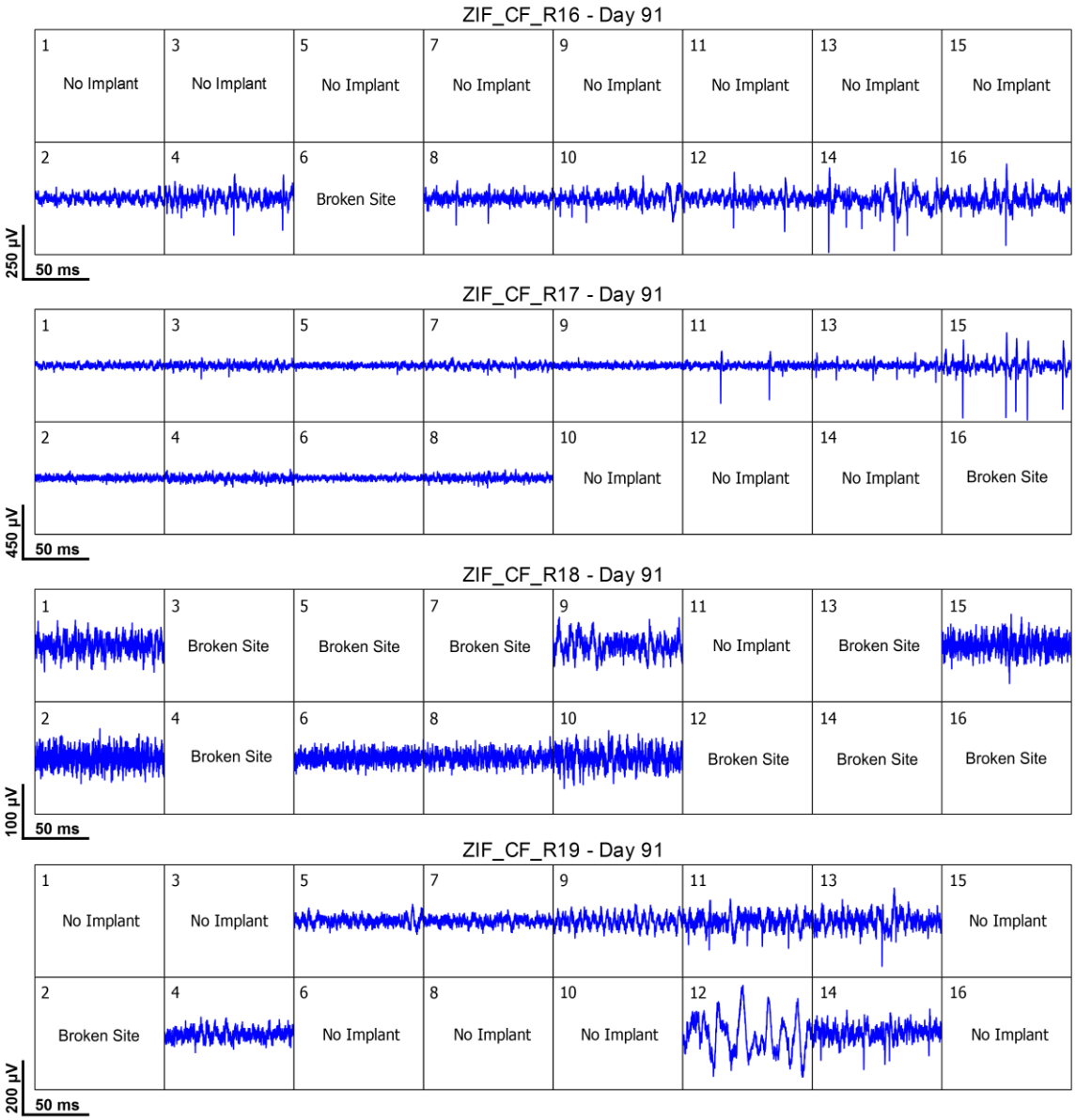

Figure 4.10. Carbon fiber electrode recordings at day 91. Representative filtered (250 Hz corner, 4th order Butterworth, high-pass) recording snippets from each implanted carbon fiber at day 91 post-operatively. Data for ZIF_CF_R22 is no longer presented as it was removed from the study at day 73.

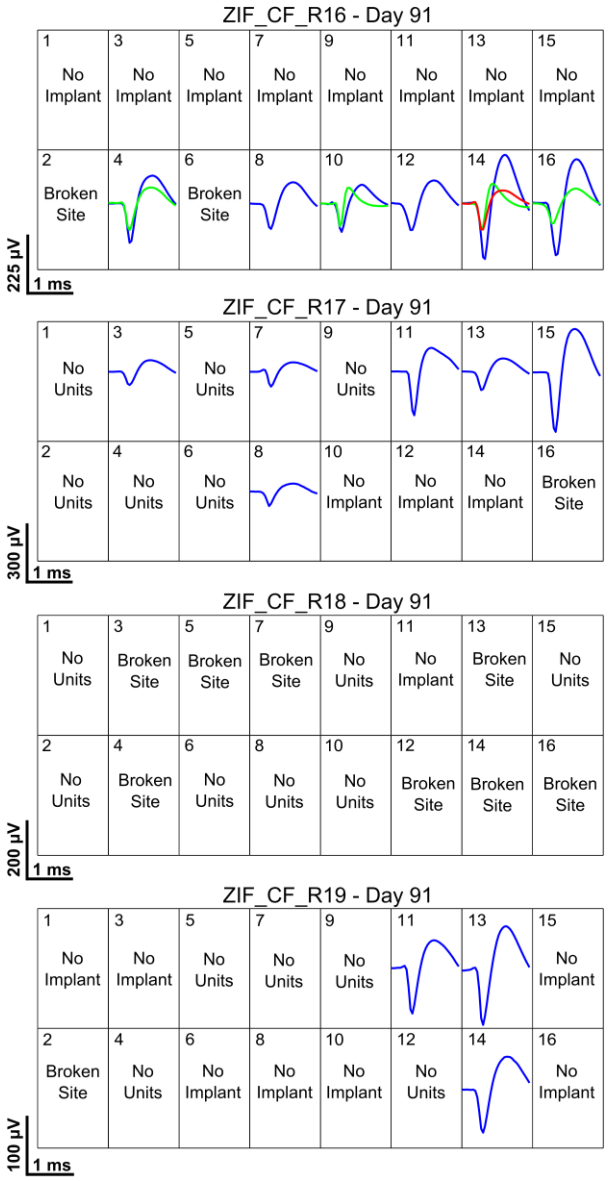

Figure 4.11. Carbon fiber electrode unit activity at day 91. Average waveforms of sorted units detected on each implanted carbon fiber at day 91 post-operatively. Data for ZIF_CF_R22 is no longer presented as it was removed from the study at day 73.

4.4.4 Noise and Signal-to-Noise Ratio

In addition to unit activity, the baseline noise level (figure 4.12(a)) was quantified for both implant types. This was in turn was used to calculate the signal-to-noise ratio (SNR) (figure 4.12(b)) for only the carbon fiber electrodes, as the silicon electrodes saw minimal to no unit activity over time.

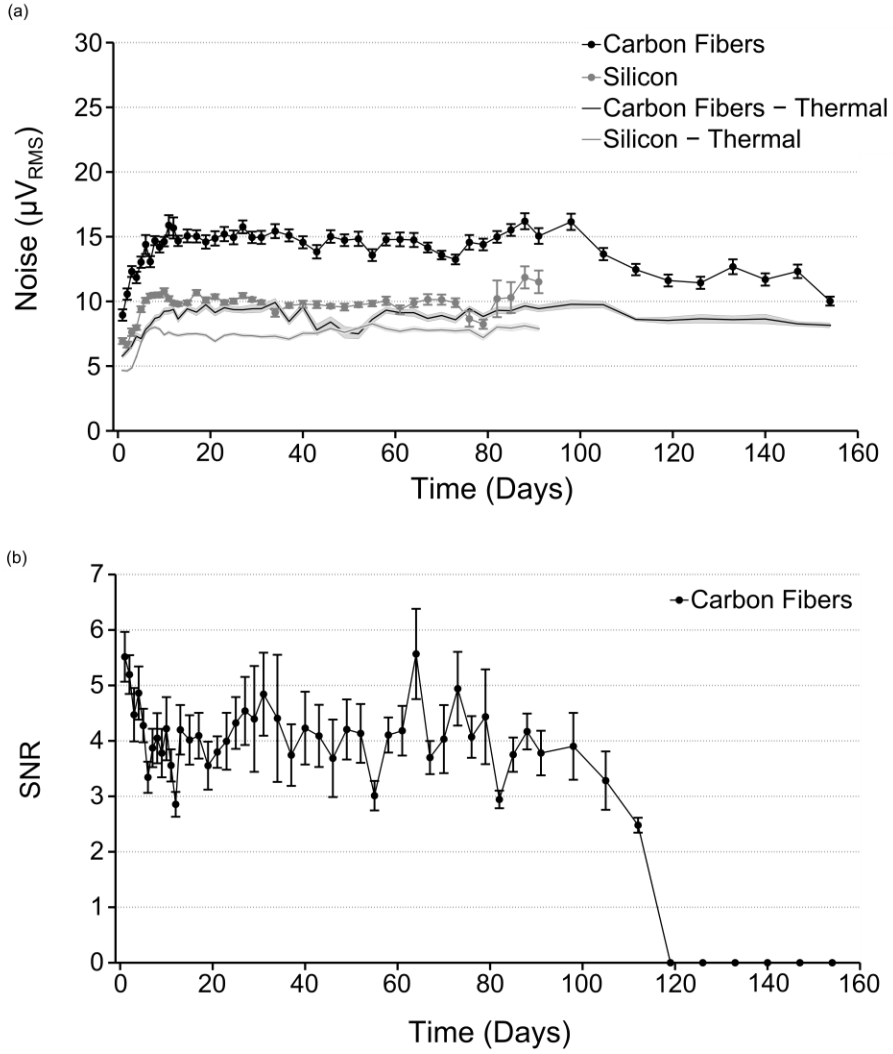

Figure 4.12. Chronic noise floor, thermal noise, and SNR. (a) Recorded noise levels (mean ± standard error of the mean) and thermal noise levels (mean ± standard error of the mean) for both carbon fiber and silicon electrodes across time. All noise trends rise during the first two weeks of recording and then level off to steady state values. Carbon fibers demonstrate a higher overall recorded noise level than silicon, which can be explained by a larger biological noise contribution as evidenced by the high amplitude recordings reported in previous sections. (b) The SNR (mean ± standard error of the mean) for all units detected on the carbon fiber electrodes across time. After an initial drop-off within the first week, values level off and hold between 3.5 and 5. The number of channels used for calculating the noise levels and SNR at each time point can be seen in appendix figure B.2.

Noise levels for both the carbon fiber electrodes and silicon electrodes rose for roughly the first 11 days. The initial noise level for the carbon fiber electrodes (8.9 ± 0.4 μV) and silicon electrodes (6.9 ± 0.2 μV) were similar at day 1 and initially peaked at

days 11 (15.9 ± 0.8 µV) and 10 (10.8 ± 0.2 µV), respectively. After this time, both sets of noise levels stayed remarkably consistent with the carbon fibers displaying a noise level around 15µV and the silicon electrodes around 10 µV, with some slight day to day variations. At approximately day 91 for the carbon fiber electrodes and day 76 for the silicon electrodes the stability of the noise levels starts to change rapidly. The larger variations in noise levels for both probe types near their respective ends is likely attributable to the decreased sample size.

Thermal noise was also calculated for each probe type and found to closely match the trends of the 1 kHz impedance values. Carbon fiber thermal noise, after starting at ~6 µV, climbed to just below 10 µV and remained there for the duration of the study. The silicon electrodes' thermal noise had a similar trend starting at ~4.5 µV and climbing to a steady state of approximately 7.5 µV.

SNR levels for the carbon fiber electrodes initially started at 5.5 ± 0.4 and then decreased to 3.3 ± 0.3 at day 6. After this time the average SNR increased and was largely maintained between 3.5 and 5 with some days deviating from this pattern. At day 91, when 4 animals remained in the study, average SNR was still 3.8 ± 0.4. After this time point SNR values rapidly dropped off as the remaining animals (n=2) showed decreased unit activity amplitude as seen in figure 4.5(a).

4.4.5 SEM Imaging of Explanted Carbon Fiber Electrodes.

Carbon fiber electrodes from chronic implants were explanted at the end of each animal's time point and imaged (figures 4.13(a) – 4.13(d)) to better understand any physical changes the electrodes underwent.

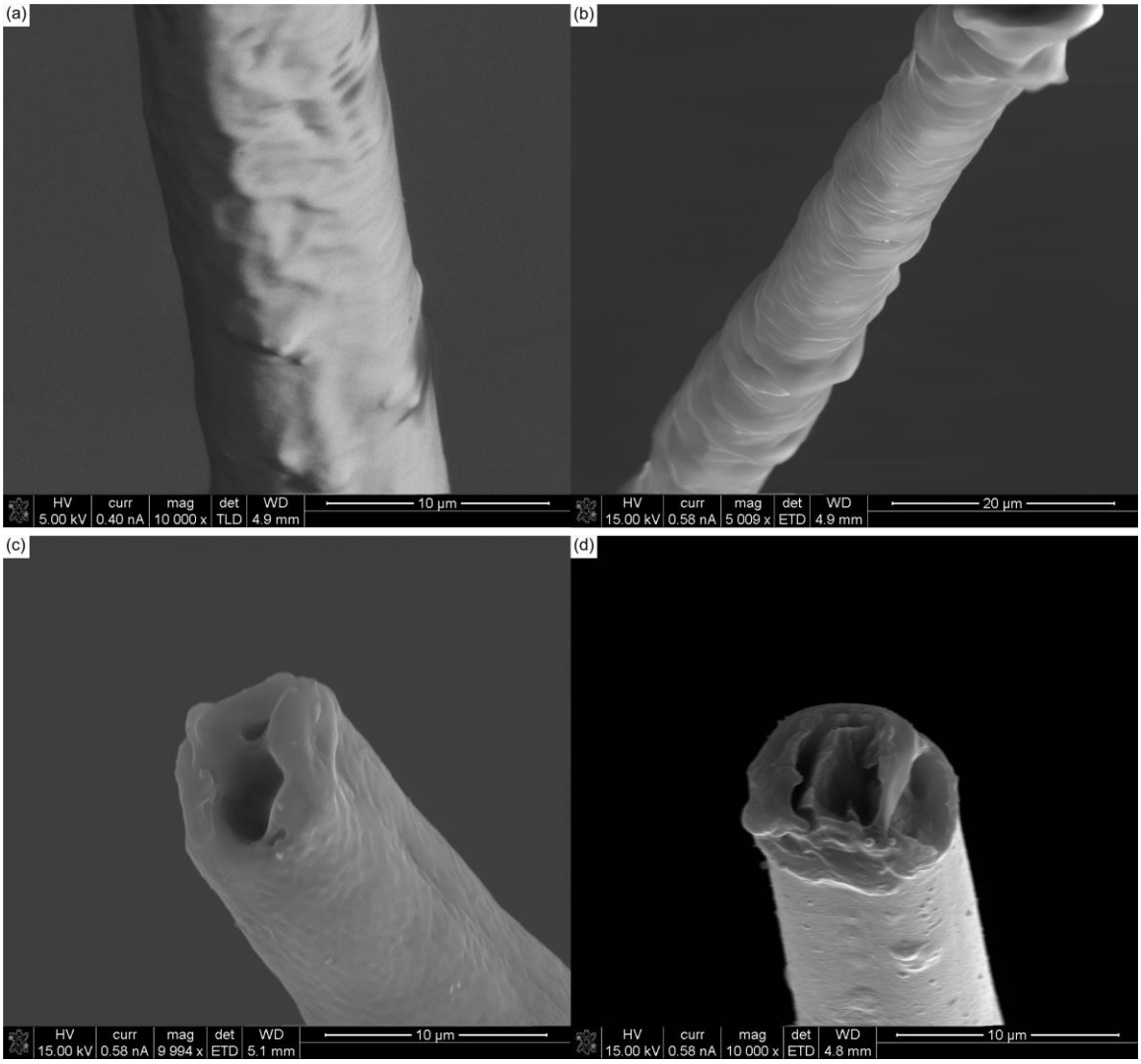

Figure 4.13. SEM images of chronically implanted carbon fibers. (a) & (b) SEM images of chronically implanted carbon fibers that may be experiencing parylene-c delamination. (c) & (d) SEM images of chronically implanted carbon fiber with a loss of surface roughness at the electrode tip indicating a loss of PEDOT in the center, the attachment of a thin adherence layer, or a combination of both.

Figures 4.13(a) and 4.13(b) highlight possible parylene-c delamination along the shank of the carbon fiber electrodes. This delamination, especially near the tip site can affect the probes ability to detect local activity. Figure 4.13(c) shows what may be a thin coating of biological material that could affect the PEDOT:pTS coating. In addition, the center of the electrode tip demonstrates a void similar to that seen with the soak test fibers. This void may initially be caused by an uneven PEDOT:pTS electrodeposition, where more

PEDOT:pTS is deposited around the edges (Cui & Martin 2003). As the PEDOT degrades, the center shows the most pronounced change as it likely has the thinnest coating (Cui & Martin 2003). This center voiding phenomenon is also seen in figure 4.13(d).

4.5 Discussion

4.5.1 Accelerated Aging Evaluation

This work first sought to validate a new site tip coating for the carbon fiber arrays. Accelerated soak tests were implemented to rapidly assess the viability of PEDOT:pTS as compared to PEDOT:PSS. For the first 70 simulated days, the impedances of both sets of fibers remained similar. After this time point the PEDOT:PSS fibers saw a more rapid increase in impedance as compared to the PEDOT:pTS coated fibers. The overall increase in impedance can be attributed to the slow degradation of both PEDOT formulations (Mandal et al. 2014; Green et al. 2012). This is further is corroborated by SEM images which show a lack of PEDOT in the center of the electrodes. The greater stability of the PEDOT:pTS coating agrees well with results seen by others (Green et al. 2012) and led to the decision to switch to a different formulation of PEDOT for the site coating.

4.5.2 *In Vivo* Assessment of Carbon Fibers and Silicon Electrodes

Impedance levels for both probe types increased dramatically over the course of the first three weeks. These results are typical for chronically implanted electrodes (Mandal et al. 2014; Ludwig et al. 2006; Vetter et al. 2004; Prasad & Sanchez 2012; Williams et al. 2007). Historically, this increase in impedance has been largely attributed

to the glial scar creating a resistive layer around the probe (Williams et al. 2007; Sankar et al. 2014; McConnell et al. 2009). And as previously seen, this glial scar can also lead to widespread neuronal death (Biran et al. 2005) and therefore a loss of signal. Unfortunately, the lack of a macroscopic scar seen in previous carbon fiber work (Kozai et al. 2012) makes it difficult to account for the impedance increase seen with the carbon fibers. We propose a more nuanced model, which argues that even the largest of glial scars cannot fully account for the impedance rise seen in implanted Utah arrays (Malaga et al. 2014), which are made of stable materials (Negi et al. 2010), and in our own case where the carbon fibers do not create a traditional macroscopic scarring response (Kozai et al. 2012). Instead, dramatic increases in impedance can best be accounted for by an extremely thin resistive layer (~0.5 μm) made up biological material, such as cells or proteins, that is directly adhering to the recording site's surface.

Determining a first order approximation of this hypothesized thin layer's resistivity can be accomplished using the following equation:

$$R = \frac{\rho L}{A} \tag{4.4}$$

where R = impedance at 1 kHz, ρ = resistivity, L = length or thickness, and A = area of the probe interface. It can be assumed that the probes' own internal resistances are unchanging in the first three weeks, which is a reasonable approximation for implanted metal electrodes and for the carbon fiber site coatings given the results from the soak test. Therefore, any change in resistance can be attributed to the thin adherence layer. The area of the carbon fiber electrodes was scaled by a factor of 10 to conservatively account for the PEDOT:pTS coating's increase on effective surface area (Cui et al. 2001).

Calculating the resistivity from our own results (Malaga et al. 2014), leads to the values seen in table 4.2.

Probe Type	$R_{Pre\text{-}Implant}$ (MΩ)	$R_{Week\ 3}$ (MΩ)	ΔR (MΩ)	Area (μm^2)	Length (μm)	ρ (Ω-cm)
Carbon Fiber	0.136	1.75	1.614	363.1	0.5	23,435
Silicon	1.126	3.061	1.935	177	0.5	13,708
Utah Array	0.3787	0.8441	0.2315	1,100	0.5	20,476

Table 4.2. Adherence layer resistivity. Calculated resistivity values for adherence layers on each probe type are shown to be on the same order of magnitude and similar in value.

Across all probe types the resistivity of the adherence layer is within the same order of magnitude and similar in value. The leveling off of all impedance values after approximately the 3rd week is likely due to the adherence layer reaching a steady state in thickness and coverage. The large unit amplitudes seen immediately and well after week 3 on the carbon fiber electrodes indicate that this thin adhesion layer is not severely affecting the ability of the fibers to record activity.

Noise levels rose in a similar time course to that of the 1 kHz impedance values for both probe types, though the increase was more pronounced for the carbon fibers, which is counterintuitive given the lower impedance of the carbon fibers over time. This however, can be explained by separating the elements that contribute to overall background noise. Baseline noise is a combination of thermal and biological sources (Lempka et al. 2011; Lempka et al. 2006). Calculating thermal noise shows that for both probe types, values rose in a similar time course as both the 1 kHz impedance and overall noise levels. This is to be expected as the minimal adherence layer on the electrode surfaces will impact impedance, which will also affect the calculated thermal noise values. While the thermal and overall noise levels did track together, they are not the same, indicating that there is also a biological noise component. This biological component is larger for the carbon fiber electrodes than it is for the silicon probes

pointing to a greater survival rate of neurons around the carbon fibers as compared to the silicon electrodes. This is also reflected by the carbon fibers' consistent ability to detect unit activity. The greater number of neurons around the carbon fiber electrodes may not always be detected as individual units, but can still contribute to the overall background noise, indicating a healthier local tissue environment. This is also supported by the sparse number of units detected on the silicon probes, which may be suffering from mechanical failures (Kozai et al. 2015).

While the biological noise may be a contributing factor to overall noise, power spectral density (PSD) analysis indicates that there may be another noise source. PSD analysis of random pairings of noise snippets between carbon fiber sites and silicon sites from the same time point can be seen in figure 4.14. In the lower band of frequencies (< 3 kHz) the carbon fibers demonstrate higher power which is where spiking activity is known to occur and these spikes were also detected by the carbon fiber electrodes. The carbon fibers and silicon sites show varying differences in the upper frequency (> 3 kHz) power levels which is a region not known to contain neural content or information. In this region an outside noise source is likely making a contribution.

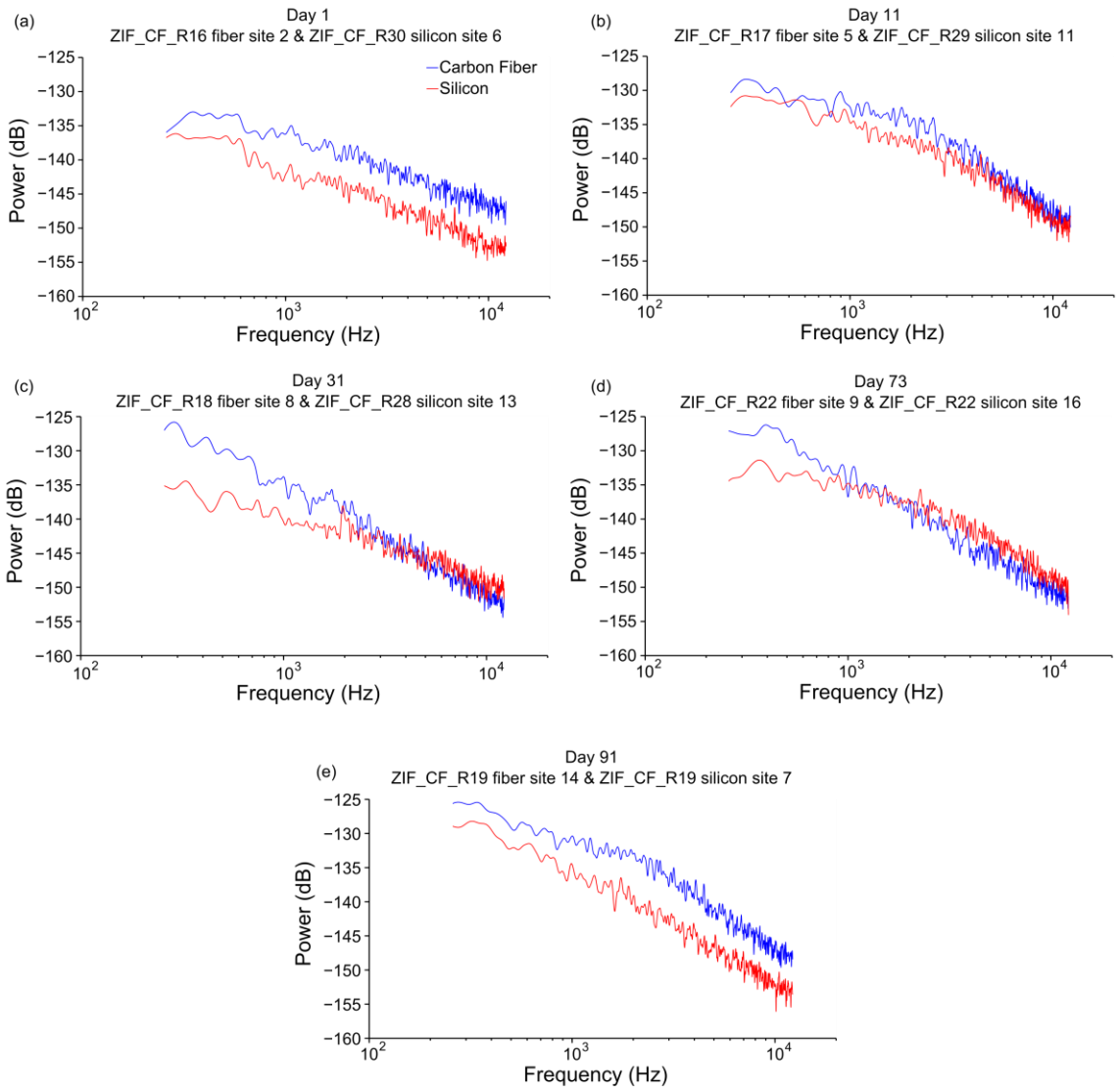

Figure 4.14. Power spectral density of recording snippets. (a)-(e) Power spectral density of recording snippets that were used to calculate noise levels. Each plot contains the PSD of a single fiber site and a single silicon site from the same time period. In each plot the carbon fiber site tends to show a higher power in the lower frequency band (< 3 kHz). The varying relative power between the fiber and silicon sites in the upper band (> 3 kHz) for each plot indicates that additional noise factors, other than biological or thermal, may be contaminating the recorded signal.

The carbon fiber arrays were able to detect unit activity until day 112, or week 16, after which no more activity was detected. This can be partially attributed to the low number of animals (n=2) at the later time point. In addition, explanted brains from earlier implants showed swelling of the cortex into the craniotomy which likely caused the electrodes to move and not record from their target layer. Unfortunately, this swelling

also made it difficult to separate the headcap from the brain without damaging the tissue, which ultimately led to a much lower number of animals that were available for histology. Swelling was alleviated by filling the craniotomy with Kwik-Cast in later animal surgeries. It is important to note that the large unit amplitudes detected on the carbon fiber electrodes point to a minimal if not non-existent scar around the electrode. This is further corroborated by ZIF_CF_R19's tissue response which was seen in chapter III. This animal's histology showed the formation of a scar around the silicon electrode coupled with decreased neuronal density and no evident scar around the carbon fiber arrays coupled with a healthy neuronal population. These histology results correlate well with the electrophysiology results seen in this study.

Amplitude values obtained by averaging the largest unit on each channel across time (figure 4.15) compare favorably to those seen in chronic implants of Utah arrays in primates (Chestek et al. 2011).

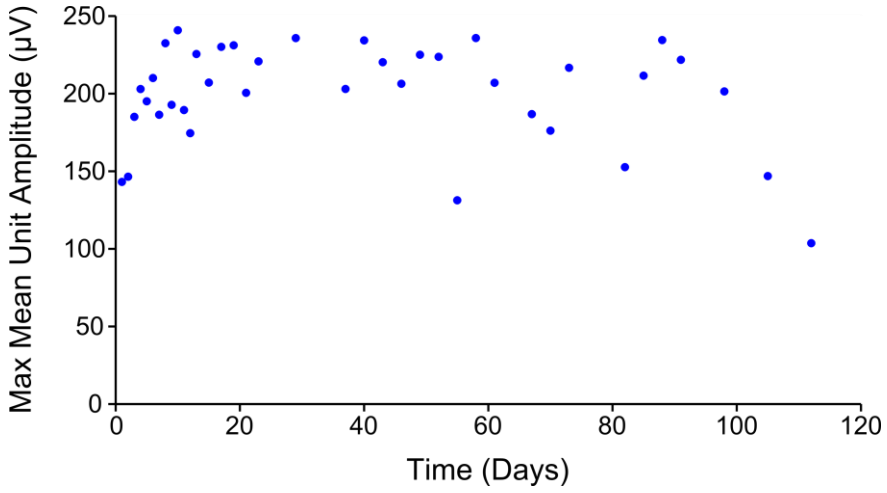

Figure 4.15. Mean of maximum amplitude for carbon fiber electrodes. The mean of the largest unit detected on each carbon fiber was calculated for each time point. These values compare well to those calculated by Chestek et al. using chronically implanted Utah arrays in primates (Chestek et al. 2011).

The high unit amplitudes and low noise levels also contribute to a high SNR on the carbon fiber electrodes. This SNR remained stable for the first three months after an initial drop off. This drop off was caused by an increasing baseline noise level (figure 4.12(a)) and not decreasing unit amplitude, which was rising during the same period (figure 4.5(a)).

4.6 Conclusion

This work has demonstrated the ability of carbon fiber electrodes to chronically record unit activity in the rat motor cortex out to 16 weeks. The units detected were of large amplitude and showed a high SNR. The carbon fibers greatly outperformed silicon electrodes with comparable site sizes and were also shown to detect a larger level of biological noise, indicating a healthier local tissue environment. This is also corroborated by the quality of detected unit activity. It is important to note that the stability of detected unit activity was not tracked across time as this was beyond the scope of the current study, but more analysis will be needed in this area to assess the viability of these electrodes for BMI applications. In addition, while both electrode types were implanted directly in the motor cortex no specific muscle group or region was targeted. This in turn may have led to a lower yield as this study relied on spontaneous awake activity and not activity associated with a specific task which may have resulted in a higher electrode yield.

Further work will seek to improve the performance of the PEDOT and parylene-c coatings. Methods to reduce brain swelling and shield the carbon fibers from mechanical damage are being explored with improved array packaging and fabrication. Improvements in all of these areas could lead to high density recording arrays that cause

minimal damage to the surrounding tissue and record high quality unit activity for many years.

4.7 References

ATSM, F.-07, 2011. Standard Guide for Accelerated Aging of Sterile Barrier Systems for Medical Devices. (ATSM F1980-07).

Berke, J.D., Breck, J.T. & Eichenbaum, H., 2009. Striatal Versus Hippocampal Representations During Win-Stay Maze Performance. *Journal of Neurophysiology*, 101(3), pp.1575–1587.

Biran, R., Martin, D.C. & Tresco, P.A., 2005. Neuronal cell loss accompanies the brain tissue response to chronically implanted silicon microelectrode arrays. *Experimental Neurology*, 195(1), pp.115–126.

Campbell, P.K. et al., 1991. A Silicon-Based, Three-Dimensional Neural Interface - Manufacturing Processes For An Intracortical Electrode Array. *IEEE Transactions On Biomedical Engineering*, 38(8), pp.758–768.

Carmena, J.M. et al., 2003. Learning to control a brain-machine interface for reaching and grasping by primates. *PLoS Biology*, 1(2), pp.193–208.

Chestek, C.A. et al., 2011. Long-term stability of neural prosthetic control signals from silicon cortical arrays in rhesus macaque motor cortex. *Journal of Neural Engineering*, 8(4), p.45005.

Cheung, K.C. et al., 2007. Flexible polyimide microelectrode array for in vivo recordings and current source density analysis. *Biosensors and Bioelectronics*, 22(8), pp.1783–1790.

Cheung, K.C., 2007. Implantable microscale neural interfaces. *Biomedical Microdevices*, 9(6), pp.923–938.

Cohen, J.Y. et al., 2012. Neuron-type-specific signals for reward and punishment in the ventral tegmental area. *Nature*, 482, pp.85–88.

Collinger, J.L. et al., 2013. High-performance neuroprosthetic control by an individual with tetraplegia. *The Lancet*, 381(9866), pp.557–564.

Cui, X. et al., 2001. Electrochemical deposition and characterization of conducting polymer polypyrrole/PSS on multichannel neural probes. *Sensors and Actuators A: Physical*, 93(1), pp.8–18.

Cui, X. & Martin, D.C., 2003. Electrochemical deposition and characterization of poly(3,4-ethylenedioxythiophene) on neural microelectrode arrays. *Sensors and Actuators B: Chemical*, 89(1-2), pp.92–102.

Davidson, T.J., Kloosterman, F. & Wilson, M.A., 2009. Hippocampal Replay of Extended Experience. *Neuron*, 63(4), pp.497–507.

Gefen, A. et al., 2003. Age-Dependent Changes in Material Properties of the Brain and Braincase of the Rat. *Journal of Neurotrauma*, 20(11), pp.1163–1177.

Gray, C.M. et al., 1995. Tetrodes markedly improve the reliability and yield of multiple single-unit isolation from multi-unit recordings in cat striate cortex. *Journal of Neuroscience Methods*, 63(1-2), pp.43–54.

Green, R.A. et al., 2012. Substrate dependent stability of conducting polymer coatings on medical electrodes. *Biomaterials*, 33(25), pp.5875–5886.

Harris, A.R. et al., 2013. Conducting polymer coated neural recording electrodes. *Journal of Neural Engineering*, 10(1), p.16004.

Harris, J.P. et al., 2011. In vivo deployment of mechanically adaptive nanocomposites for intracortical microelectrodes. *Journal of Neural Engineering*, 8(4), p.46010.

Hochberg, L.R. et al., 2006. Neuronal ensemble control of prosthetic devices by a human with tetraplegia. *Nature*, 442(7099), pp.164–171.

Hochberg, L.R. et al., 2012. Reach and grasp by people with tetraplegia using a neurally controlled robotic arm. *Nature*, 485(7398), pp.372–375.

Hukins, D.W.L., Mahomed, A. & Kukureka, S.N., 2008. Accelerated aging for testing polymeric biomaterials and medical devices. *Medical Engineering & Physics*, 30(10), pp.1270–1274.

Jeon, M. et al., 2014. Partially flexible MEMS neural probe composed of polyimide and sucrose gel for reducing brain damage during and after implantation. *Journal of Micromechanics and Microengineering*, 24(2), p.25010.

Kim, B.J. et al., 2013. 3D Parylene sheath neural probe for chronic recordings. *Journal of Neural Engineering*, 10(4), p.45002.

Kozai, T.D.Y. et al., 2015. Mechanical failure modes of chronically implanted planar silicon-based neural probes for laminar recording. *Biomaterials*, 37(0), pp.25–39.

Kozai, T.D.Y. et al., 2012. Ultrasmall implantable composite microelectrodes with bioactive surfaces for chronic neural interfaces. *Nature Materials*, 11(12), pp.1065–1073.

Kuo, J.T.W. et al., 2013. Novel flexible Parylene neural probe with 3D sheath structure for enhancing tissue integration. *Lab On A Chip*, 13, pp.554–561.

Lai, H.-Y. et al., 2012. Design, simulation and experimental validation of a novel flexible neural probe for deep brain stimulation and multichannel recording. *Journal of Neural Engineering*, 9(3), p.36001.

Lempka, S.F. et al., 2006. Optimization of Microelectrode Design for Cortical Recording Based on Thermal Noise Considerations. *2006 Annual International Conference of the IEEE Engineering In Medicine and Biology Society*, pp.3361–3364.

Lempka, S.F. et al., 2011. Theoretical analysis of intracortical microelectrode recordings. *Journal of Neural Engineering*, 8(4), p.45006.

Ludwig, K.A. et al., 2006. Chronic neural recordings using silicon microelectrode arrays electrochemically deposited with a poly(3,4-ethylenedioxythiophene) (PEDOT) film. *Journal of Neural Engineering*, 3(1), pp.59–70.

Malaga, K.A. et al., 2014. Data-driven model comparing the effects of glial scarring and tip metallization loss on chronic neural recordings. *44th Annual Meeting of the Society for Neuroscience*.

Mandal, H.S. et al., 2014. Improving the performance of poly(3,4-ethylenedioxythiophene) for brain-machine interface applications. *Acta Biomaterialia*, 10(6), pp.2446–2454.

McConnell, G.C., Butera, R.J. & Bellamkonda, R. V, 2009. Bioimpedance modeling to monitor astrocytic response to chronically implanted electrodes. *Journal of Neural Engineering*, 6(5), p.55005.

Mercanzini, A. et al., 2008. Demonstration of cortical recording using novel flexible polymer neural probes. *Sensors and Actuators A: Physical*, 143(1), pp.90–96.

Najafi, K. & Hetke, J.F., 1990. Strength characterization of silicon microprobes in neurophysiological tissues. *IEEE Transactions on Biomedical Engineering*, 37(5), pp.474–481.

Najafi, K., Wise, K.D. & Mochizuki, T., 1985. A high-yield IC-compatible multichannel recording array. *IEEE Transactions on Electron Devices*, 32(7), pp.1206–1211.

Negi, S. et al., 2010. In vitro comparison of sputtered iridium oxide and platinum-coated neural implantable microelectrode arrays. *Biomedical Materials*, 5(1), p.15007.

Nicolelis, M.A.L. et al., 2003. Chronic, multisite, multielectrode recordings in macaque monkeys. *Proceedings of the National Academy of Sciences*, 100(19), pp.11041–11046.

Nordhausen, C.T., Maynard, E.M. & Normann, R.A., 1996. Single unit recording capabilities of a 100 microelectrode array. *Brain Research*, 726(1-2), pp.129–140.

Patel, P.R. et al., 2015. Insertion of linear 8.4 μm diameter 16 channel carbon fiber electrode arrays for single unit recordings. *Journal of Neural Engineering*, (accepted with minor revisions).

Prasad, A. et al., 2014. Abiotic-biotic characterization of Pt/Ir microelectrode arrays in chronic implants. *Frontiers in neuroengineering*, 7, pp.1–15.

Prasad, A. & Sanchez, J.C., 2012. Quantifying long-term microelectrode array functionality using chronic in vivo impedance testing. *Journal of Neural Engineering*, 9(2), p.26028.

Rennaker, R.L. et al., 2005. An economical multi-channel cortical electrode array for extended periods of recording during behavior. *Journal of Neuroscience Methods*, 142(1), pp.97–105.

Rousche, P.J. et al., 2001. Flexible polyimide-based intracortical electrode arrays with bioactive capability. *IEEE Transactions on Biomedical Engineering*, 48(3), pp.361–371.

Royer, S. et al., 2010. Distinct Representations and Theta Dynamics in Dorsal and Ventral Hippocampus. *Journal of Neuroscience*, 30(5), pp.1777–1787.

Sankar, V. et al., 2013. A highly compliant serpentine shaped polyimide interconnect for front-end strain relief in chronic neural implants. *Frontiers in Neurology*, 4(124), pp.1–11.

Sankar, V. et al., 2014. Electrode impedance analysis of chronic tungsten microwire neural implants: understanding abiotic vs. biotic contributions. *Frontiers in Neuroengineering*, 7, pp.1–12.

Schwartz, A.B. et al., 2006. Brain-Controlled Interfaces: Movement Restoration with Neural Prosthetics. *Neuron*, 52(1), pp.205–220.

Seymour, J.P. & Kipke, D.R., 2007. Neural probe design for reduced tissue encapsulation in CNS. *Biomaterials*, 28(25), pp.3594–3607.

Simeral, J.D. et al., 2011. Neural control of cursor trajectory and click by a human with tetraplegia 1000 days after implant of an intracortical microelectrode array. *Journal of Neural Engineering*, 8(2), p.25027.

Skousen, J.L. et al., 2011. Reducing surface area while maintaining implant penetrating profile lowers the brain foreign body response to chronically implanted planar silicon microelectrode arrays. *Progress in Brain Research*, 194, pp.167–180.

Stice, P. et al., 2007. Thin microelectrodes reduce GFAP expression in the implant site in rodent somatosensory cortex. *Journal of Neural Engineering*, 4(2), p.42.

Subbaroyan, J., Martin, D.C. & Kipke, D.R., 2005. A finite-element model of the mechanical effects of implantable microelectrodes in the cerebral cortex. *Journal of Neural Engineering*, 2(4), pp.103–113.

Takeuchi, S. et al., 2005. Parylene flexible neural probes integrated with microfluidic channels. *Lab*, 5, pp.519–523.

Taylor, D.M., Tillery, S.I.H. & Schwartz, A.B., 2003. Information conveyed through brain-control: cursor versus robot. *IEEE Transactions on Neural Systems and Rehabilitation Engineering*, 11(2), pp.195–199.

Velliste, M. et al., 2008. Cortical control of a prosthetic arm for self-feeding. *Nature*, 453(7198), pp.1098–1101.

Venkatraman, S. et al., 2011. In Vitro and In Vivo Evaluation of PEDOT Microelectrodes for Neural Stimulation and Recording. *IEEE Transactions on Neural Systems and Rehabilitation Engineering*, 19(3), pp.307–316.

Vetter, R.J. et al., 2004. Chronic neural recording using silicon-substrate microelectrode arrays implanted in cerebral cortex. *IEEE Transactions on Biomedical Engineering*, 51(6), pp.896–904.

Vetter, R.J. et al., 2005. Development of a Microscale Implantable Neural Interface (MINI) Probe System. *2005 Annual International Conference of the IEEE Engineering In Medicine and Biology Society*, 7, pp.7341–7344.

Ware, T. et al., 2014. Thiol-ene/acrylate substrates for softening intracortical electrodes. *Journal of Biomedical Materials Research Part B: Applied Biomaterials*, 102(1), pp.1–11.

Ware, T. et al., 2012. Three-Dimensional Flexible Electronics Enabled by Shape Memory Polymer Substrates for Responsive Neural Interfaces. *Macromolecular Materials and Engineering*, 297(12), pp.1193–1202.

Wester, B.A., Lee, R.H. & LaPlaca, M.C., 2009. Development and characterization of in vivo flexible electrodes compatible with large tissue displacements. *Journal of Neural Engineering*, 6(2), p.24002.

Williams, J.C. et al., 2007. Complex impedance spectroscopy for monitoring tissue responses to inserted neural implants. *Journal of Neural Engineering*, 4(4), pp.410–423.

Williams, J.C., Rennaker, R.L. & Kipke, D.R., 1999. Long-term neural recording characteristics of wire microelectrode arrays implanted in cerebral cortex. *Brain Research Protocols*, 4(3), pp.303–313.

Wise, K.D. et al., 2004. Wireless implantable microsystems: High-density electronic interfaces to the nervous system. *Proceedings of the IEEE*, 92(1), pp.76–97.

Wise, K.D. & Angell, J.B., 1975. A Low-Capacitance Multielectrode Probe for Use in Extracellular Neurophysiology. *IEEE Transactions on Biomedical Engineering*, BME-22(3), pp.212–219.

Xiang, Z. et al., 2014. Ultra-thin flexible polyimide neural probe embedded in a dissolvable maltose-coated microneedle. *Journal of Micromechanics and Microengineering*, 24(6), p.65015.

Xie, X. et al., 2014. Self-aligned tip deinsulation of atomic layer deposited Al2O3 and parylene C coated Utah electrode array based neural interfaces. *Journal of Micromechanics and Microengineering*, 24(3), p.35003.

CHAPTER V

Conclusion and Future Directions

5.1 Conclusion

This work has shown the design, fabrication, and validation of novel carbon fiber microelectrode arrays. To the best of my knowledge these arrays have the smallest electrode shank pitch of any existing device. Moreover they were able to detect unit activity for 16 weeks without the development of a macroscopic scar.

Chapter II investigated the insertion dynamics of a high density carbon fiber array. Initial results showed that for the fibers to self-insert they would need to be 750 μm or less in length. This constraint made reaching layer V of the motor cortex, an important region of the brain for BMIs, impossible. To overcome this limitation, the fibers, 4 – 5 mm in length, were temporarily stiffened with an encapsulating coating of PEG, leaving only a small portion uncoated. After this small portion was inserted into the brain the remaining PEG was dissolved away and the fibers driven to their final target. This method allowed for the insertion of 16 channel carbon fiber arrays. These insertion results also helped to inform the design of an even higher density array using a silicon support structure as a backbone for the carbon fibers. The new design was shown

to record unit activity in acute animal preparations and can be scaled to allow for the sampling of every neuron in a given cortical plane.

Chapter III sought to compare the tissue response of silicon electrodes, which are known to elicit a glial scar, and carbon fiber arrays, which should cause minimal tissue disruption due to their size. Two animals were implanted with one of each probe type, in each brain hemisphere, for three months. Histology results showed a large glial scarring response to the silicon electrodes coupled with a local decrease in neuronal density. The carbon fiber arrays showed some elevated response by glial cells but no scarring was evident. In addition, neuronal density remained healthy in the implant region. Taken together, this data strongly suggests that carbon fiber arrays can be implanted chronically without causing a scarring response or decrease in neuronal density as seen with other chronically implanted electrodes.

Chapter IV presented long-term electrophysiology and impedance data for chronically implanted carbon fiber arrays and planar silicon electrodes. The data showed carbon fibers recording unit activity with an average amplitude of 200 μV and average SNR of 4, over a three month period. During the same time period the silicon electrodes detected minimal unit activity with most time points detecting no units. While the carbon fibers also had a higher overall baseline noise level as compared to their silicon counterparts, this could be partially accounted for by a large biological noise component which points to a healthy tissue environment surrounding the carbon fibers. This was further corroborated by the high quality units that were detected on the carbon fibers and also by the lack of units detected by the silicon electrodes.

5.2 Future Directions

The carbon fiber arrays presented in this work show that they are capable of detecting unit activity with high amplitudes and quality SNRs, for long periods of time, while causing minimal disruption to the surrounding tissue. These results as a whole are an important first step in developing even higher density, non-damaging, electrode arrays that can be used in applications ranging from fundamental neuroscience studies to restoring the lost motor functions of amputees using BMIs. Before they can be widely adopted, numerous design aspects need to be explored that will help to ensure an even more robust and reliable neural interface.

The carbon fiber arrays used throughout this dissertation had an electrode pitch of approximately 150 µm. This same pitch was also used in the initial development of the silicon support structures presented in chapter II. While not explored here, this new structure can be fabricated with an electrode pitch of 90 µm. This design coupled with a recording radius of ~75 µm could allow us to record from every neuron in a given cortical layer (Moffitt & McIntyre 2005). In addition, the support structures are fabricated using cleanroom processes which means precise control over the length of each individual shank. This would enable the targeting of even deeper structures in the brain such as the hippocampus. Creating these new, customizable, high-density arrays will also require unique packaging strategies to help minimize the need for hundreds of wires to transmit recording data. The use of ASICs that can multiplex hundreds of channels (Viventi et al. 2011) or wireless transmission protocols (Borton et al. 2013; Miranda et al. 2010; Gao et al. 2012) would greatly reduce or eliminate potential wiring issues.

At the actual electrode interface end many new research avenues have been explored that would improve the stability of the insulating and site coatings. Newer formulations of PEDOT using carbon nanotubes (Zhou et al. 2013; Kolarcik et al. 2015) or tetrafluoroborate counter anions (Mandal et al. 2014) have shown excellent stability and biocompatibility for long term implants. In addition, to address any possible delamination issues (Thaning et al. 2010), a thin layer of gold can be deposited prior to the electrodeposition of PEDOT. This gold layer can improve the adherence of polymer films such as PEDOT (Cui & Martin 2003; Mandal et al. 2014). As seen in chapter IV, the parylene-c coating may be suffering from delamination which has been seen by other groups using equally thin layers of parylene-c (Chun et al. 2014; Seymour et al. 2009). Possible solutions for better adherence and stability include pre-deposition of aluminum oxide (Xie, Rieth, Negi, et al. 2014; Xie, Rieth, Williams, et al. 2014), annealing of the parylene-c post-deposition (Metzen & Stieglitz 2013), the use of reactive parylene films (Seymour et al. 2009), or a combination of treatments.

Improving the recording capabilities of these electrode is the most pressing priority, but carbon fibers can also be used to detect local concentrations of neurotransmitters. One of the most prevalent uses of carbon fibers in neuroscience is to detect changes in dopamine concentrations. Decreased dopamine levels are directly tied to Parkinson's disease (Lotharius & Brundin 2002) and has been linked to depression (Dailly et al. 2004). While carbon fibers can be used to detect dopamine without any special coatings, they can also be functionalized with enzymatic coatings to detect other neurotransmitters such as acetyl choline (Burmeister et al. 2003; Parikh et al. 2004) and glutamate (Burmeister et al. 2002; Hamdi et al. 2006). Creating an array with the

capability to concurrently detect electrophysiology and a combination of neurotransmitters would lead to a far deeper understanding of neuronal circuit communication and dynamics. A more comprehensive picture at the electrical and chemical level could lead to better diagnoses and treatment strategies for neurological disorders.

5.3 Concluding Remarks

As with any new technology, there will always be tradeoffs between desired functionality and design constraints. The hope is that the information gathered in this dissertation will help to inform a new generation of devices that can meet the needs of many different groups of people. Key to this work's current and future success has been and will always be the ongoing discussion between designers and end users. While this may seem obvious on the surface, too often in our field and others, technology is developed without the end user in mind. It is my firm belief that the success of this recording technology will hinge upon the collaborative efforts of neural engineers, neuroscientists, and neurosurgeons. It is only when these groups converge that great strides are made in medicine and science. It is my hope that this work will continue down this path, leading to a better understanding of the brain and ultimately to more advanced neuroprosthetics and treatments for neurological disorders.

5.4 References

Borton, D.A. et al., 2013. An implantable wireless neural interface for recording cortical circuit dynamics in moving primates. *Journal of Neural Engineering*, 10(2), p.26010.

Burmeister, J.J. et al., 2002. Improved ceramic-based multisite microelectrode for rapid measurements of L-glutamate in the CNS. *Journal of Neuroscience Methods*, 119(2), pp.163–171.

Burmeister, J.J., Palmer, M. & Gerhardt, G.A., 2003. Ceramic-based multisite microelectrode array for rapid choline measures in brain tissue. *Analytica Chimica Acta*, 481(1), pp.65–74.

Chun, W. et al., 2014. Evaluation of sub-micrometer parylene C films as an insulation layer using electrochemical impedance spectroscopy. *Progress in Organic Coatings*, 77(2), pp.537–547.

Cui, X.Y. & Martin, D.C., 2003. Fuzzy gold electrodes for lowering impedance and improving adhesion with electrodeposited conducting polymer films. *Sensors and Actuators A: Physical*, 103(3), pp.384–394.

Dailly, E. et al., 2004. Dopamine, depression and antidepressants. *Fundamental & Clinical Pharmacology*, 18(6), pp.601–607.

Gao, H. et al., 2012. HermesE: A 96-Channel Full Data Rate Direct Neural Interface in 0.13 µm CMOS. *IEEE Journal of Solid-state Circuits*, 47(4), pp.1043–1055.

Hamdi, N. et al., 2006. An electroenzymatic l-glutamate microbiosensor selective against dopamine. *Journal of Electroanalytical Chemistry*, 591(1), pp.33–40.

Kolarcik, C.L. et al., 2015. Evaluation of poly(3,4-ethylenedioxythiophene)/carbon nanotube neural electrode coatings for stimulation in the dorsal root ganglion. *Journal of Neural Engineering*, 12(1), p.16008.

Lotharius, J. & Brundin, P., 2002. Pathogenesis of parkinson's disease: dopamine, vesicles and [alpha]-synuclein. *Nature Reviews Neuroscience*, 3(12), pp.932–942.

Mandal, H.S. et al., 2014. Improving the performance of poly(3,4-ethylenedioxythiophene) for brain-machine interface applications. *Acta Biomaterialia*, 10(6), pp.2446–2454.

Metzen, R.P. von & Stieglitz, T., 2013. The effects of annealing on mechanical, chemical, and physical properties and structural stability of Parylene C. *Biomedical Microdevices*, 15, pp.727–735.

Miranda, H. et al., 2010. HermesD: A High-Rate Long-Range Wireless Transmission System for Simultaneous Multichannel Neural Recording Applications. *IEEE Transactions on Biomedical Circuits and Systems*, 4(3), pp.181–191.

Moffitt, M.A. & McIntyre, C.C., 2005. Model-based analysis of cortical recording with silicon microelectrodes. *Clinical Neurophysiology*, 116(9), pp.2240–2250.

Parikh, V. et al., 2004. Rapid assessment of in vivo cholinergic transmission by amperometric detection of changes in extracellular choline levels. *European Journal of Neuroscience*, 20(6), pp.1545–1554.

Seymour, J.P. et al., 2009. The insulation performance of reactive parylene films in implantable electronic devices. *Biomaterials*, 30(31), pp.6158–6167.

Thaning, E.M. et al., 2010. Stability of poly(3,4-ethylene dioxythiophene) materials intended for implants. *Journal of Biomedical Materials Research Part B: Applied Biomaterials*, 93B(2), pp.407–415.

Viventi, J. et al., 2011. Flexible, foldable, actively multiplexed, high-density electrode array for mapping brain activity in vivo. *Nature Neuroscience*, 14(12), pp.1599–1605.

Xie, X., Rieth, L., Williams, L., et al., 2014. Long-term reliability of Al2O3 and Parylene C bilayer encapsulated Utah electrode array based neural interfaces for chronic implantation. *Journal of Neural Engineering*, 11(2), p.26016.

Xie, X., Rieth, L., Negi, S., et al., 2014. Self-aligned tip deinsulation of atomic layer deposited Al2O3 and parylene C coated Utah electrode array based neural interfaces. *Journal of Micromechanics and Microengineering*, 24(3), p.35003.

Zhou, H. et al., 2013. Poly(3,4-ethylenedioxythiophene)/multiwall carbon nanotube composite coatings for improving the stability of microelectrodes in neural prostheses applications. *Acta Biomaterialia*, 9(5), pp.6439–6449.

APPENDIX A

Supplemental Material for Chapter II

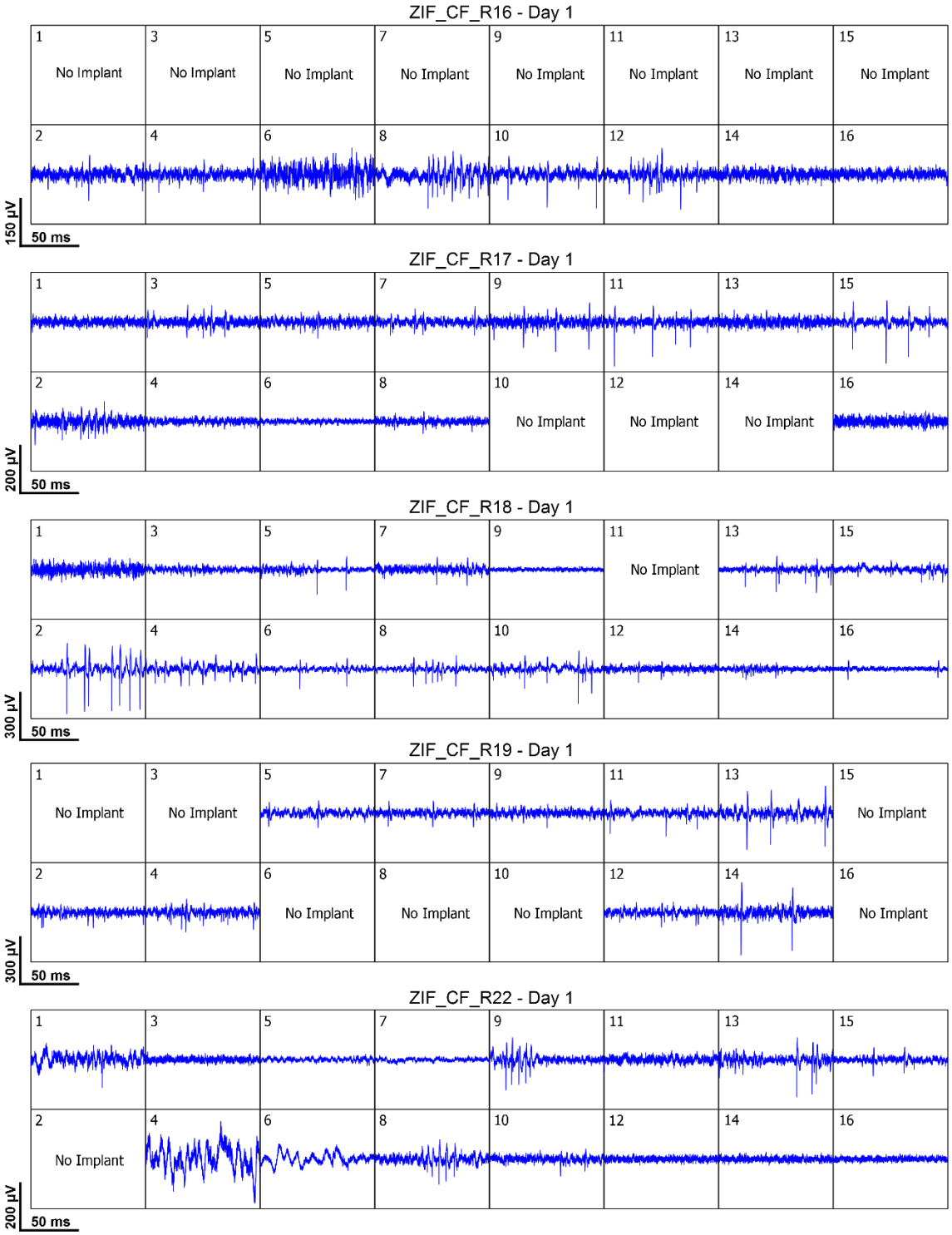

Figure A.1. Carbon fiber electrode recordings at day 1. Representative filtered (250 Hz corner, 4th order Butterworth, high-pass) high speed recordings from each implanted carbon fiber at day 1 post-operatively.

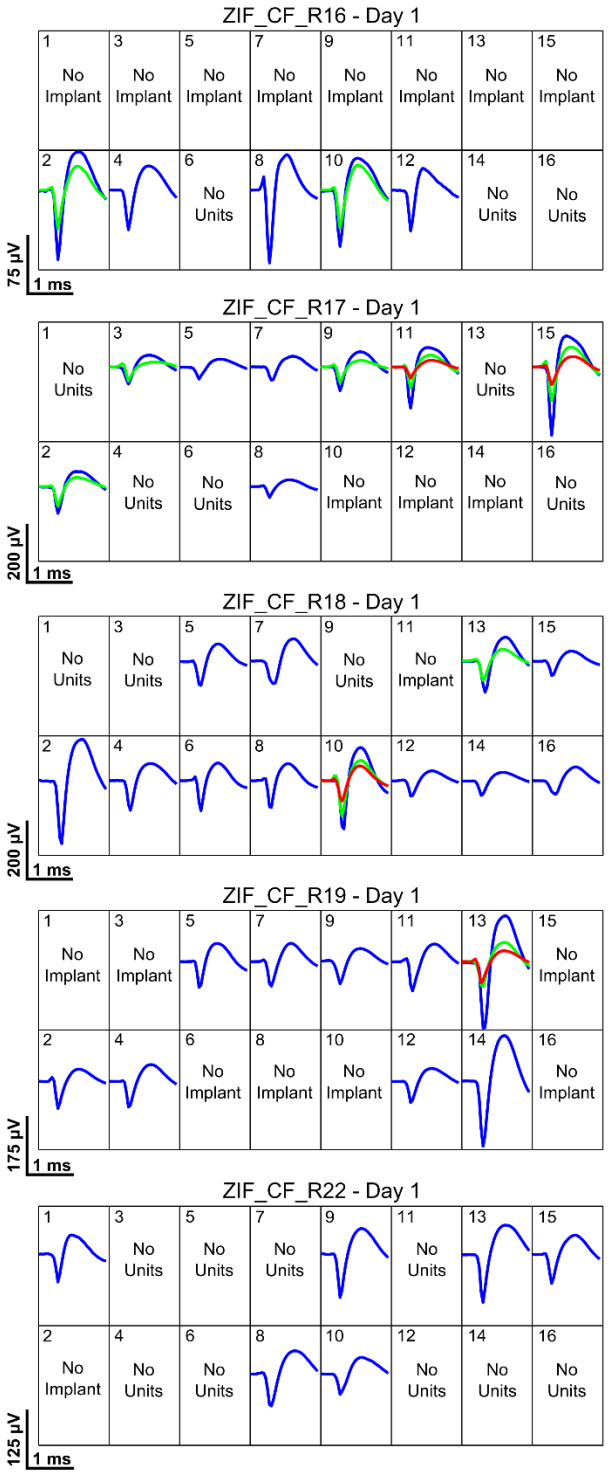

Figure A.2. Carbon fiber electrode unit activity at day 1. Average waveforms of sorted units detected on each implanted carbon fiber at day 1 post-operatively.

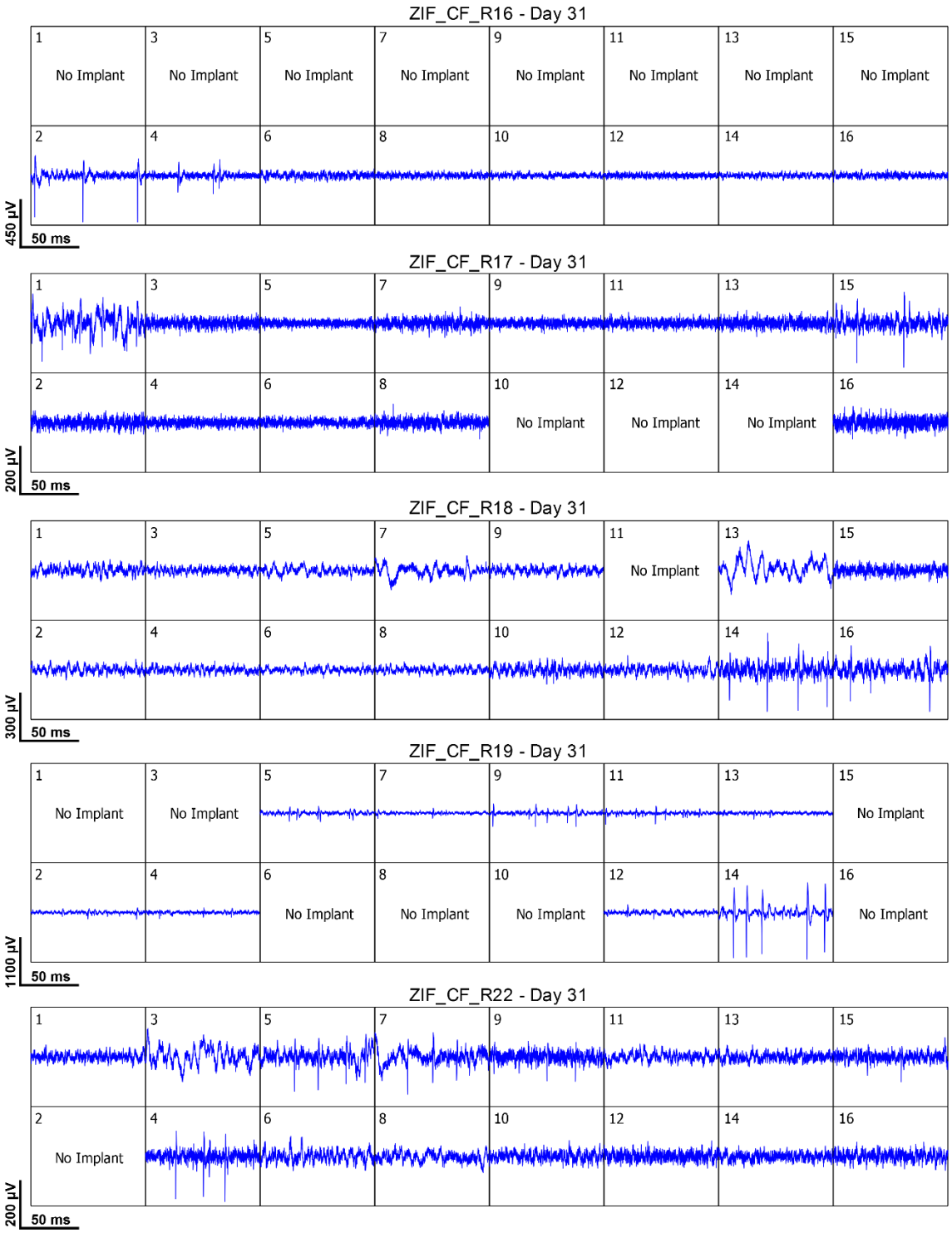

Figure A.3. Carbon fiber electrode recordings at day 31. Representative filtered (250 Hz corner, 4th order Butterworth, high-pass) high speed recordings from each implanted carbon fiber at day 31 post-operatively.

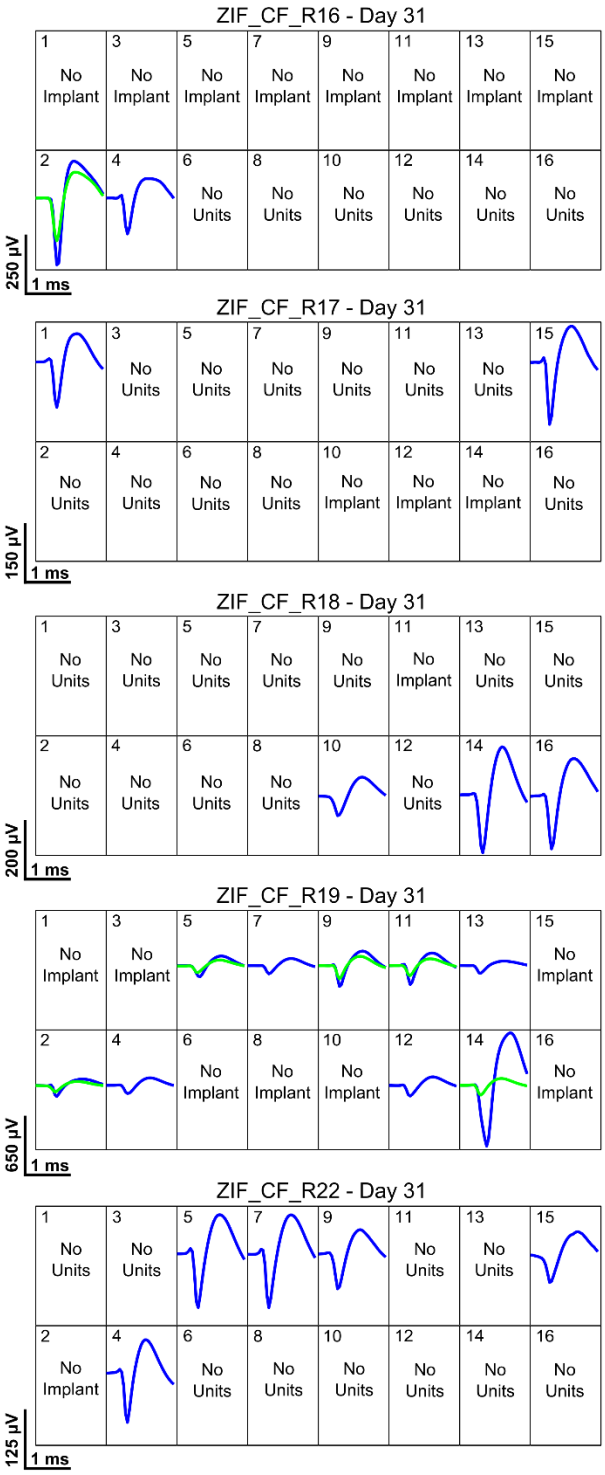

Figure A.4. Carbon fiber electrode unit activity at day 31. Average waveforms of sorted units detected on each implanted carbon fiber at day 31 post-operatively.

APPENDIX B

Supplemental Material for Chapter IV

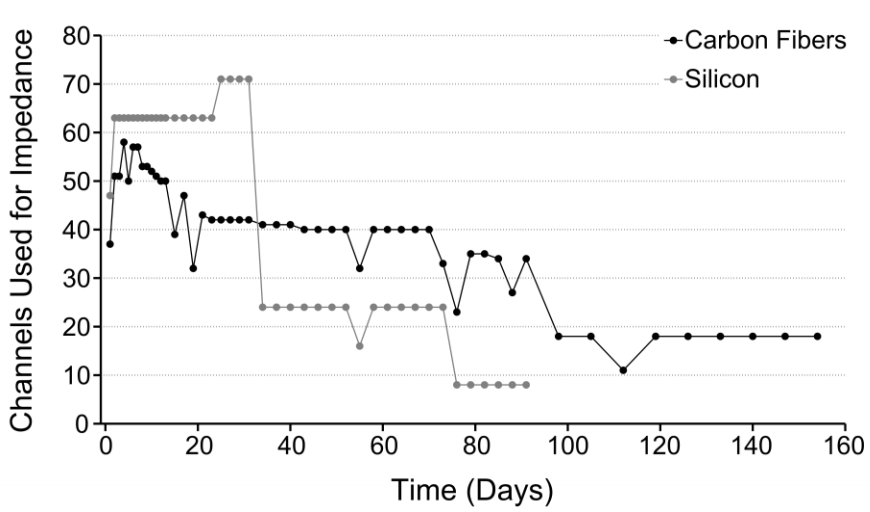

Figure B.1. Number of channels used for impedance results. For the silicon electrodes, the initial jump in channel count from day 1 to 2 was due to a poor connection (i.e. open circuit) during impedance measurements on day 1. The increase from day 23 to 25 was due to eight channels for ZIF_CF_R22 being reincorporated after a headstage had been repaired. The sharp decline after day 31 is from three animals no longer being in the study while two remain. The brief dip at day 55 was due to a missed time point. The decline at day 73 was due to another animal being removed from the study with one remaining until day 91. For the carbon fibers, the initial jumps from day 1 to 2 and then 3 to 4 were also due to a poor connection during impedance measurements on days 1 and 3. All subsequent dips and recoveries, except at day 55 which was a missed time point, were due to impedance values that indicated a poor connection. The drop off at day 91 is from the removal of three animals with two remaining until day 154.

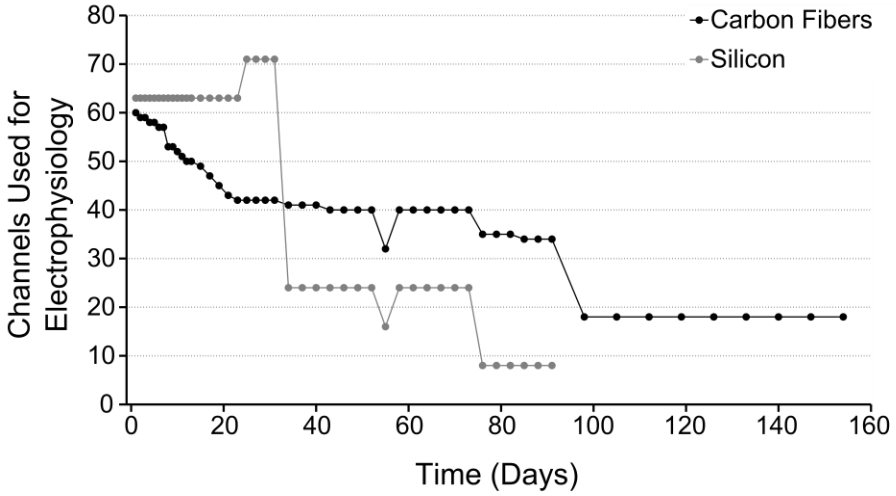

Figure B.2. Number of channels used for electrophysiology and noise results. For the silicon electrodes, the increase from day 23 to 25 was due to eight channels for ZIF_CF_R22 being reincorporated after a headstage had been repaired. The sharp decline after day 31 is from three animals no longer being in the study while two remained. The brief dip at day 55 was due to a missed time point. The decline at day 73 was due to another animal being removed from the study with one remaining until day 91. For the carbon fibers, the continual decline in channel count was due to channels being removed as their 10 Hz impedance magnitudes matched those of known broken channels. The two exceptions to this were day 55, which was a missed time point, and after day 91 when three of the animals were removed from the study and only two remained until day 154.

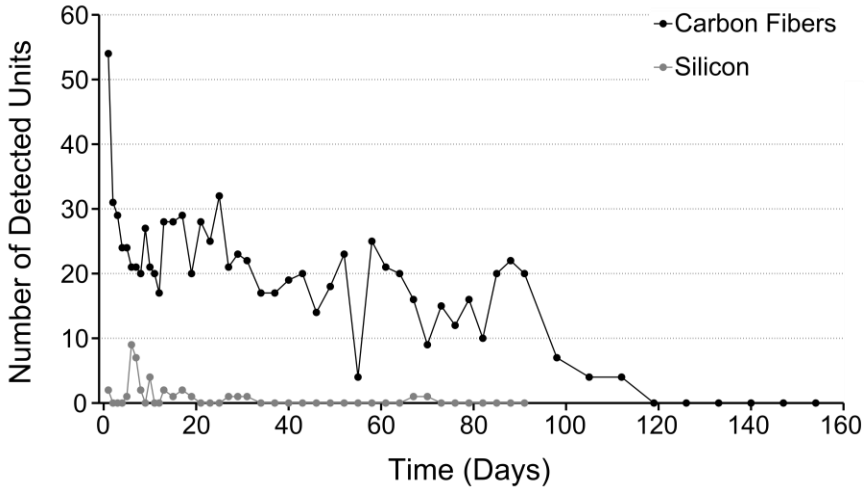

Figure B.3. Number of units detected for each probe type. For each probe type, the number of units detected on the valid electrophysiology channels from B.2, is plotted over time.